UNIVERSIDAD AUTÓNOMA DE MADRID

Departamento de Física de la Materia Condensada

NOVEL THERMOELECTRIC AND ELASTIC RESPONSES IN DIRAC MATTER

Tesis doctoral presentada por

Vicente Arjona Romano

Programa de doctorado de Física de la Materia Condensada, Nanociencia y Biofísica

Directora:

María Ángeles Hernández Vozmediano

Tutor:

Amadeo López Vázquez de Parga

Madrid, Octubre de 2019

... el cor m'encises
amb ton blau del cel tan bell
amb tes platjes remoroses,
que escomou l'ambat lleuger.
Amb les flors de tes praderes.
Amb lo cant de los aucells.
De lo cel é el paradis
per a mi semblança n'ets!

Tomàs Forteza

Contents

List of Figures

Agradecimientos

Al iniciar la tesis, nadie imagina el camino que va a recorrer hasta llegar a la meta. Este periodo ha estado repleto de momentos increíbles y grandes retos, y si he llegado al final ha sido gracias a la ayuda y el apoyo de magníficas personas que me han acompañado y formado, tanto profesional como personalmente, durante estos años.

En primer lugar, me gustaría agradecer a María, mi directora de tesis, haberme brindado la oportunidad de trabajar junto a ella y confiar en mí, hace ya cuatro años, para dirigirme y ayudarme en mi formación como científico. De ella no sólo he aprendido muchísima física, sino también unos hábitos, perspectiva y forma de hacer las cosas que llevaré siempre conmigo. Me enseñó a creer en mis capacidades y a madurar como investigador, y si ahora me encuentro escribiendo estas líneas ha sido gracias a su continuo e incansable esfuerzo para que este proyecto saliera adelante. Cualquier logro que pueda conseguir en un futuro será gracias a ella.

Me gustaría también agradecer a Amadeo López, mi tutor en la universidad, por acceder a tutelar esta tesis y su absoluta disponibilidad durante el transcurso de esta.

El trabajo de esta tesis ha sido realizado en colaboración con varios investigadores a los que también quiero agradecer por su dedicación: Eduardo Castro, Maxim Chernodub y Juan Borge.

El excelente ambiente de trabajo y motivación del ICMM ha contribuido enormemente a la consecución de esta tesis, gracias a la ayuda de excelentes científicos de los que también he aprendido. Estaré siempre agradecido a Alberto, uno de los mejores físicos que he conocido. Su pasión e incesante trabajo son para mí el ejemplo de lo que un investigador debe ser. Siempre le agradeceré y admiraré por su infinita sabiduría y su inestimable ayuda ante cualquier dificultad que he tenido. Cada visita a su despacho me ha enseñado algo nuevo de física (y no sólo física), alentándome con fuerzas renovadas a seguir aprendiendo. Quiero también agradecer especialmente a Yago, con quien he tenido el placer de trabajar durante el último año. Su claridad, capacidad e intuición a la hora de abordar y explicar los problemas me han ayudado a mejorar como científico. A Pilar, Belén y Pablo quiero agradecerles su valiosa ayuda y consejo siempre que las he necesitado. Me gustaría también mencionar a Paco, Luca, Jose, Ángel, Nacho, Leni y Rafa, grandes físicos y compañeros que me han ayudado durante mi formación.

I am deeply grateful to Eduardo for his very kind hospitality during my stay in Lisboa and Porto. I appreciate the time and patience that he spent to discuss physics with me, and his guidance and clear expositions on topics that were completely new to me. Learning from him during my stay was indeed invaluable. From that time I

would also thank the group at Técnico, especially Bruno, with whom I could share enjoyable talks about everything. I will always remember all the people that made me feel Lisboa as my home. Among them, I would like to give special thanks to Thiago and Jose. I really regard the few months that we spent together as unforgettable.

En el plano más personal, estoy inmensamente agradecido a mis amigos de materiales, con quienes he tenido la fortuna de compartir todo el proceso del doctorado: Raquel, Alfonso, Óscar, Francesca, María, Dani, Ana, María Jesús, Álvaro, Fernando y César. Su incondicional apoyo y ánimo han sido esenciales para llevar a cabo esta tesis. Gracias a ellos el día a día en el instituto (y fuera de él) ha sido mucho más fácil y divertido, compartiendo toda clase de momentos, risas, inquietudes y anécdotas que hoy todavía siguen y siempre recordaré. Su amistad es sin duda una de las cosas más valiosas e importantes que me llevo.

No podria deixar d'agrair als meus amics de l'illa que m'han acompanyat i donat suport al llarg de tants anys: Miguel, Christian, Bea, Pilar, Natalia, Luis, Alex, Gaspar i Germán. Incomptables són les experiències, converses i metes que hem compartit i superat junts des de petits (sobretot Gaspar i Germán, que porten ja massa temps patint-me). Em sent molt afortunat i agraït de continuar mantenint amistats com les vostres. M'agradaria agrair especialment a Miguel, per la seva infinita ajuda durant el procés de fer la tesi, i a Carmen, a qui sempre agrairé el seu continu suport durant aquest viatge i mostrar-me que creia en mi a l'hora de superar qualsevol repte.

Finalment, m'agradaria dedicar unes paraules a les persones que porten impulsant-me des del principi fins a arribar a la persona que sóc ara. Realment li dec tot als meus pares i germà. Vull agrair la seva incansable dedicació i infinit afecte, així com el seu suport i comprensió en totes les decisions que he pres. La seva constant força i motivació han estat el motor que m'ha empès a donar el millor de mi durant aquests anys. També vull agrair a la resta de la meva família i especialment als meus padrins, que han patit igual o més que jo el dur camí de convertir-me en científic. Aquesta tesi va dedicada a vosaltres.

Publications

The work presented in this thesis has given rise to the following publications and preprints:

- "*Collapse of Landau levels in Weyl semimetals*"
  Vicente Arjona, Eduardo V. Castro and María A.H. Vozmediano
  Physical Review B **96**, 081110 (R) (2017)
  Selected as "Rapid communication"

- "*Rotational strain in Weyl semimetals: A continuum approach*"
  Vicente Arjona and María A.H. Vozmediano
  Physical Review B **97**, 201404 (R) (2018)
  Selected as "Rapid communication"

- "*Fingerprints of the conformal anomaly in the thermoelectric transport in Dirac and Weyl semimetals*"
  Vicente Arjona, Maxim N. Chernodub and María A.H. Vozmediano
  Physical Review B **99**, 235123 (2019)

- "*Thermoelectric relations in the conformal limit in Dirac and Weyl semimetals*"
  Vicente Arjona, Juan Borge and María A.H. Vozmediano
  arXiv preprint, arXiv:1903.00019 (2019)

Abstract

This thesis studies some aspects of the physics of topological semimetals, a set of novel three-dimensional matter systems whose low-energy electronic excitations are described by Dirac quasiparticles. The unconventional features of these materials, ranging from basic physics to technological applications, have generated a substantial research activity during the last years. The interest in crystalline structures hosting Dirac quasiparticles lies partially on the relativistic nature of their electronic degrees of freedom, making them an ideal laboratory to test and study fundamental physics phenomena. This thesis addresses two topics of major interest in the physics of these systems: the interplay between lattice deformations and electronic properties, and the influence of anomalies on the thermoelectric response.

In the first part of this thesis, the thermoelectric response of Dirac and Weyl semimetals is studied in the presence of strong magnetic fields. The anomalous thermoelectric behaviour is addressed at the charge neutrality point, where a finite contribution to the thermoelectric coefficient is obtained in the conformal limit.

The thermoelectric coefficients fulfill robust phenomenological relations based on the Landau-Fermi liquid paradigm of coherent quasiparticles. These relations may be challenged when the system has strong interactions or when it presents a poor metallic behaviour. The validity of the Mott relation, a phenomenological law that relates the thermopower and the electrical conductivity coefficients, is discussed in the regime of zero doping and zero temperature. In particular, the off-diagonal components of the electric and thermoelectric tensors are analyzed in the presence of a magnetic field.

The influence of external deformations on the lattice configuration of topological semimetals is essential to understand their electronic properties. In these systems, elastic deformations couple to the low-energy electronic excitations in the form of elastic gauge fields. The possibility of controlling the dynamics of carriers by appropriate strain geometries has given rise to a prolific industry associated with straintronics. In the second part of this thesis, the coupling of lattice deformations to Dirac quasiparticles in three-dimensional materials is studied by using a symmetry approach. An interesting aspect is that, in contrast with the two-dimensional case, the antisymmetric part of the deformation tensor couple to the electronic excitations in three-dimensional Dirac materials.

Finally, the interplay between electromagnetic fields and elastic deformations is also discussed, in which the collapse of Landau levels is showed in the presence of strain. The similarities of this mechanism with the case of real magnetic and electric fields are emphasized, discussing possible strain configurations giving rise to this effect.

Resumen

Esta tesis estudia aspectos de la física de los semimetales topológicos, un conjunto de materiales tridimensionales cuyas excitaciones electrónicas de baja energía son descritas por las cuasipartículas de Dirac. Las características poco convencionales de estos sistemas, que abarcan desde la física fundamental hasta las aplicaciones tecnológicas, han generado una importante actividad investigadora durante los últimos años. El interés en sistemas de cuasipartículas de Dirac radica en parte en la naturaleza relativista de sus grados de libertad electrónicos, convirtiendo estos materiales en sistemas ideales para examinar y estudiar fenómenos de física fundamental. Esta tesis aborda dos temas de gran interés en la física de estos sistemas: la interacción entre las deformaciones de la red y las propiedades electrónicas, y la influencia de las anomalías en la respuesta termoeléctrica.

En este trabajo, se ha estudiado la respuesta termoeléctrica de los semimetales de Dirac y Weyl en presencia de un campo magnético intenso. El comportamiento termoeléctrico anómalo ha sido analizado en el punto de neutralidad de carga, donde se ha obtenido una contribución finita al coeficiente termoeléctrico en el límite conforme.

Los coeficientes termoeléctricos satisfacen relaciones fenomenológicas basadas en el paradigma de cuasipartículas del líquido de Fermi. Estas relaciones pueden ser cuestionadas cuando el sistema tiene interacciones fuertes o cuando presenta un mal comportamiento metálico. Se ha discutido la validez de la relación de Mott, una ley fenomenológica que relaciona la potencia térmica y el coeficiente de conductividad eléctrica en el límite de dopaje y temperatura cero. En particular, se han analizado las componentes no diagonales de los tensores eléctrico y termoeléctrico en presencia de un campo magnético.

La influencia de las deformaciones de la red de los semimetales topológicos resulta esencial para entender sus propiedades electrónicas. En estos sistemas, las deformaciones elásticas se acoplan a las excitaciones electrónicas de baja energía en forma de campos gauge elásticos. La posibilidad de controlar la dinámica de los portadores con las configuraciones de deformación apropiadas ha dado lugar a toda una industria dedicada a "straintronics". Se ha estudiado el acoplo de las deformaciones elásticas a las cuasipartículas de Dirac en materiales tridimensionales usando una acción efectiva basada en la simetría del sistema. Un aspecto interesante es que, al contrario de lo que ocurre en materiales bidimensionales, la parte antisimétrica del tensor de deformación se acopla a las excitaciones electrónicas en los materiales tridimensionales de Dirac.

Finalmente, se ha discutido la inter-relación entre los campos electromagnéticos y las deformaciones elásticas, mostrando el colapso de los niveles (pseudo) de

Landau en presencia de deformaciones. Se ha enfatizado la similitud de este mecanismo con el caso de campos magnéticos y eléctricos reales, discutiendo las posibles configuraciones de deformación que dan lugar a este efecto.

Chapter 1

Introduction

"A physical law must possess mathematical beauty"
- Paul A. Dirac

A complete quantum theory consistent with the postulates of special relativity was given in 1928 by Dirac [1]. He introduced an equation that describes the dynamics of the electron as a relativistic quantum particle and led to a natural insight into the concept of spin. Written in a covariant language, the Dirac equation reads:

$$\left(i\hbar c\gamma^{\mu}\partial_{\mu} - mc^2\right)\psi(x) = 0, \tag{1.1}$$

where ψ is a 4-component wave-function describing the electron and $\mu = 0, 1, 2, 3$. The matrices γ^{μ}, known as Dirac matrices, satisfy the particular anticommutation relation $\{\gamma^{\mu}, \gamma^{\nu}\} = 2\eta^{\mu\nu}$, with $\eta^{\mu\nu} = \text{diag}(1, -1, -1, -1)$.

Condensed matter physics focuses on understanding and studying the physical properties of large collections of atoms arranged in a periodic array. Since the typical energy scales in these systems are much smaller than the mass of the electron, a relativistic description of the electronic degrees of freedom was considered unnecessary. Nevertheless, the two branches of physics meet through the exchange of conceptual ideas and techniques. A typical example is the concept of renormalization group; first developed to control the divergences arising in quantum electrodynamics, it has been applied to solve problems in condensed matter physics, such as the Landau-Fermi liquid or the Kondo problem [2, 3]. During the last decade, the synthesis of a novel class of materials has opened a new bridge between condensed matter and high energy physics: the *Dirac matter*, whose electronic degrees of freedom are effectively described by the massless Dirac equation.

Although materials modeled with the Dirac equation were already known in condensed matter [4, 5], it was after the experimental realization of graphene in 2005 [6, 7] when the physical consequences of such equation were fully explored by the community [8]. The synthesis of graphene was followed by other important material realizations of the massless Dirac equation; the edge states of the topological insulators [9–12]. More recently, Dirac and Weyl semimetals are three-dimensional (3D) topological materials hosting massless Dirac spinors in the vicinity of linear band-crossings points [13–18].

This thesis centers on the interplay between high-energy processes and condensed matter phenomena in Weyl and Dirac semimetals. In particular, it studies the response of Dirac quasiparticles to magnetic fields (real or fictitious) and spatial deformations. Throughout this thesis, we will see that both topics are precisely interconnected when studying the thermoelectric response of Dirac materials and the coupling between the lattice deformations and electronic degrees of freedom.

We begin this introductory chapter by discussing the relevant characteristics of Weyl semimetals, whose linearly dispersing valence and conduction bands meet at isolated points at the Fermi level. In the first section, we discuss the conditions under which degeneracies arise in electronic band structures and its connection with the relativistic Dirac equation. In the second section we review the basic concepts to understand the topological character of such degeneracy points. In the third section, we describe the emergence of new terms that can be added to the Dirac equation when Lorentz invariance is broken and their physical consequences in material systems. The discussion of this chapter is partially based on the description of topological semimetals provided in the collection of review articles [19–25].

1.1 Weyl fermions

The Dirac equation characterizes the motion of relativistic spin-1/2 fermions with mass m, and is the first theory that successfully reconciles the principles of quantum mechanics (equations of motion must depend only on the first time derivative) and special relativity (time and spatial coordinates should be treated symmetrically). By taking the limit $m \to 0$ in Equation (1.1), Weyl noticed that the equation could be split into two decoupled equations [26]:

$$\begin{aligned} i\hbar\partial_0\psi_\pm(x) &= H_\pm\psi_\pm(x), \\ H_\pm &= \pm\sum_{j=1}^{3} c\sigma^j p_j, \end{aligned} \tag{1.2}$$

where σ^j are the Pauli matrices, $p_j = -i\hbar\partial_j$ is the momentum of the particle and $\psi_\pm$ is a two component bi-spinor. The resulting dispersion relation takes the form $E = \pm\hbar ck$, with k being the modulus of the corresponding wave-vector. In order to obtain Equation (1.2), the Weyl representation $\gamma^0 = \sigma^x \otimes \mathbb{I}_2$, $\gamma^i = i\sigma^y \otimes \sigma^i$ is used. We will adopt this convention throughout this thesis.

In any odd spatial dimension d, we can define a chirality operator constructed with the matrix $\gamma^5 = i^k\gamma^0\gamma^1\dots\gamma^d$ [27] that commutes with the Weyl Hamiltonian. This commutation relation is guaranteed for odd spatial dimensions, provided that γ^5 anticommutes with the velocity matrices γ^i. The Weyl spinors are eigenstates of definite chirality and have a well defined helicity (projection of the spin on the momentum).

Weyl fermions do not exist as fundamental particles. Neutrinos were conjectured as a promising candidate, but the discovery of neutrino oscillations implied that they have a finite mass [28, 29], eliminating them as an option. Manifestations of Weyl physics can be observed in the quark-gluon plasma [30, 31], and now in condensed matter systems. In the forthcoming sections, we will see how pairs of Weyl fermions separated in energy or momentum space arise in the vicinity of degeneracy points in electronic band structures.

1.1.1 Electronic band theory and quasiparticles in crystalline structures

At the microscopic level, ions of macroscopic crystalline structures are arranged in a periodic lattice. The interactions among atoms are strong enough to maintain the solid structure of the material. Hence, electrons in a crystalline structure are described as particles subjected to a periodic potential with the symmetry of the underlying lattice. This observation led the physicist Bloch to study the Schrödinger equation in an effective periodic potential. He showed that the eigenstates of the one-electron Hamiltonian have the form $\psi_{n\mathbf{k}}(\mathbf{r}) = e^{i\mathbf{kr}}u_{n\mathbf{k}}(\mathbf{r})$, where $\mathbf{k}$ is the crystal momentum of the electron and the function $u_{n\mathbf{k}}(\mathbf{r}) = \langle r|u_n(\mathbf{k})\rangle$ has the periodicity of the Bravais lattice; $u_{n\mathbf{k}}(\mathbf{r}+\mathbf{R}) = u_{n\mathbf{k}}(\mathbf{r})$, with $\mathbf{R}$ being the lattice vector [32, 33]. The index n labels the different solutions of the Scrödinger equation in the periodic momentum space. These discretely spaced eigenvalues form an infinite family of functions that depend continuously on the crystal momentum $\mathbf{k}$. Unlike the free electron case where any energy value is permitted, the electrons of a crystalline lattice are only allowed to occupy states within a certain energy window or *band*.

The band structure provides essential information to understand the characteristics and properties of crystalline structures. In particular, the transport properties of any material are ultimately determined by the amount of available electrons and its band structure, classifying them into metals and insulators. In the presence of a

finite Fermi surface, energy bands near the Fermi level in metals have a quadratic dispersion. Electronic excitations in such bands are described in the continuum limit by the Scrödinger equation, and its dispersion relation is $E_{\mathbf{k}} = \hbar^2 k^2/2m_{\text{eff}}$, where the effective mass m_{eff} accounts for deviations from the mass of the electron [34]. The definition of m_{eff} is associated with the concept of *quasiparticle*; in the presence of interaction processes –disorder, scattering effects or Couloumb interactions– the electronic excitations are "dressed particles" with effective mass m_{eff} and finite lifetime. The concept of quasiparticle was introduced by the Russian physicist Landau, who, in his work *The Theory of a Fermi Liquid* [35], explained how a system of strongly interacting particles (with a well-defined Fermi surface) can still be described as a free-motion system. Later, the theory was understood with the mathematical formalism of renormalization group [2, 36].

Defining conceptual, simple models to understand the nature of more complicated systems is the main goal of theoretical physics. Over the years, a plethora of effective particles have been introduced in order to explain the collective behaviour of different systems. Notable examples are phonons, which are used to describe the quantized vibrational modes of the lattice. Quasiparticle excitations have also provided excellent results in explaining more exotic phenomena. Various examples are composite fermions [37–39], Bogoliubov quasiparticles [40, 41] or magnetic skyrmions [42, 43]. The concept of quasiparticle will appear again when studying the effective dispersion relation around degeneracy points.

1.1.2 Degeneracy points and linear dispersion relations. Emergence of low-energy Dirac electrons in condensed matter

Field theory models arise in condensed matter as low-energy effective descriptions that are obtained by expanding the dispersion relation around the Fermi surface. Although most metallic compounds are effectively described by the Schrödinger equation, a relativistic dispersion relation may emerge under some conditions in crystalline structures. In the early days of quantum mechanics [44, 4], it was noted that in the vicinity of two-fold degeneracies or band touching points, the dispersion relation is linear and coincides with the dispersion of a massless Weyl spinor. An interesting question is then to ascertain what conditions are required to get band-crossing points near the Fermi energy in a material.

Considering a pair of non-degenerate energy bands, the most general 2×2 Hamiltonian can be cast in the form[1]

$$H = f_0(\mathbf{k}) + \sigma^x f_1(\mathbf{k}) + \sigma^y f_2(\mathbf{k}) + \sigma^z f_3(\mathbf{k}), \tag{1.3}$$

[1] In writing Equation (1.3), we have exploited the fact that the three Pauli matrices and the identity matrix form a basis for all two-by-two matrices.

whose eigenvalues are given by

$$E_{\mathbf{k}} = f_0(\mathbf{k}) \pm \sqrt{f_1^2(\mathbf{k}) + f_2^2(\mathbf{k}) + f_3^2(\mathbf{k})}. \tag{1.4}$$

In the absence of any symmetry, Equation (1.4) shows that the emergence of a degeneracy point $\mathbf{k}_*$ requires tuning the three parameters $f_i(\mathbf{k})$ to nullify the terms inside the square root. In three dimensional solids, where the Hamiltonian depends on the three components of the wave-vector, this condition is naturally satisfied, allowing the presence of stable band-crossing points at isolated points in the Brillouin zone. It is clear that additional conditions are required in two spacial dimensions to guarantee band crossings.

By expanding the generic Hamiltonian described in Equation (1.3) in a power series near the degeneracy point $\mathbf{k} = \mathbf{k}_*$ in the linear regime, the resulting expression is:

$$H = \hbar v_{ij} \sigma^i (\mathbf{k} - \mathbf{k}_*)^j, \tag{1.5}$$

with $v_{ij} = \partial_j f_i|_{\mathbf{k}=\mathbf{k}_*}$. Equation (1.5) coincides with the Weyl equation defined in Equation (1.2) after a shift $\mathbf{k} \to \mathbf{k} - \mathbf{k}_*$ and neglecting constant terms, with the replacement $c \to v_{ij}$. As discussed at the opening of the section, electronic excitations of two-fold degeneracies at the Fermi level are described by massless quasiparticles where the sign of the determinant

$$\chi = \text{sign det}(v_{ij}) = \text{sign det} \left. \frac{\partial f_i}{\partial k^j} \right|_{\mathbf{k}=\mathbf{k}_*} \tag{1.6}$$

determines the chirality χ of the gapless mode. These band-crossings are referred as *Weyl nodes* [18] (see Figure 1.1). The symmetry conditions under which the conduction and valence band coincide at the Fermi level were examined in the early work by Abrikosov and Beneslavskiĭ [5]. A non-degenerate electronic band structure is found in materials where either inversion symmetry ($\mathcal{P}$) or time-reversal symmetry ($\mathcal{T}$) are broken[2] [20]. Hence, non-centrosymmetric or magnetic systems are promising candidates to host unremovable Weyl nodes. The interest in materials hosting these degeneracies has grown significantly during the last years due to the improvement in the experimental synthesis of crystals. The theoretical excitement is partly motivated by the fact that high energy physical properties of Weyl fermions, such as the chiral anomaly [45, 46], remain present in this non-relativistic context.

[2]The energy levels of fermionic systems that present $\mathcal{P}$ or $\mathcal{T}$ symmetry have a band structure at least doubly degenerate. Symmetry implications on the band spectrum will be studied in detail in section 1.3.3.

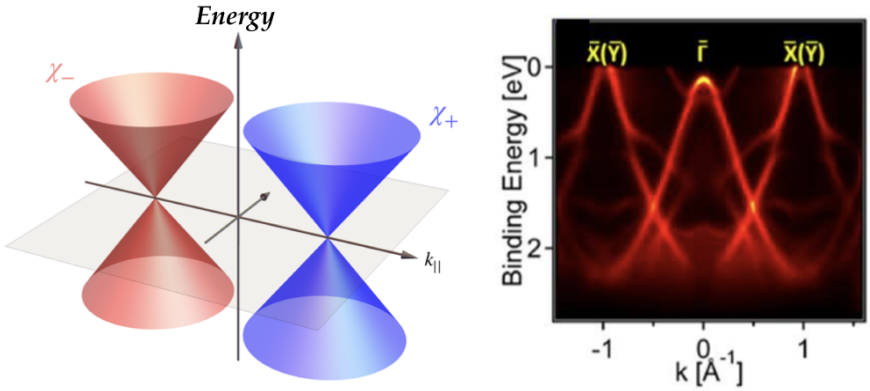

FIGURE 1.1: *(Left)*: Schematic representation of the dispersion relation corresponding to two Weyl nodes of opposite chirality. *(Right)*: Angle-resolved photoemission spectroscopy (ARPES) experiments of the crystal NbP. Adapted from Ref. [47].

1.2 Topological features of Weyl fermions

In order to have materials described by the Weyl equation, the band crossings must occur near the Fermi energy, which is fixed by the chemical composition of the crystal. Materials having these kind of degeneracies are known as *Weyl semimetals* (WSMs). As we will see, their band-crossing points are topologically protected. Contrary to two-dimensional crystals, degeneracy points are stable to small perturbations of the parameters regardless of the symmetry, as all Pauli matrices have been exhausted. Adding a mass term in the Hamiltonian proportional to one of the matrices only shifts the position of the solution, i.e., moves the Weyl node in crystal momentum space. In this section, we will show that the stability of the nodes is ultimately related to the non-trivial topology of the band structure. The details of the calculation are presented in appendix A.

1.2.1 Topology in condensed matter physics

Prior to the discovery of the quantum Hall effect, quantum phases of matter were classified according to the Ginzburg-Landau theory [48]. Within this framework, states of matter are characterized in terms of local order parameters, independently of the microscopic details of the system. Specifically, the order parameters acquire a finite value when the system undergoes a phase transition to a lower symmetry state. This paradigm allowed to understand the underlying mechanism behind (almost)

all physical transitions discovered during the last century, such as superconductivity [48], ferromagnetic order [49, 50] or Bose-Einstein condensation [51–53]. With the emergence of novel phases of matter during the last decades, it became clear that the symmetry-breaking paradigm is insufficient to capture some effects, as occurred in quantum Hall systems [54]. A full description of these phases demanded a new criteria whose foundations laid on the mathematical notion of topology [11, 12, 55].

Topological aspects of many-particle systems began to be explored by the condensed matter community with the advent of the quantum Hall effect and the awareness of the role played by the Berry curvature [56, 54]. Afterwards, the prediction and experimental realization of topological insulators [57, 11, 58] has given rise to a prolific activity, both theoretically and experimentally, in this field. Equivalent topological phases are characterized by the same topological index, whose character depends on the general properties of the spectrum under their discrete symmetries and dimensionality [10, 11, 59–61].

1.2.2 Topological aspects of band-crossing points. Berry phase of crystal Hamiltonians

Although initially circumscribed to gapped systems, a manifest interest in the study of the topological properties in gapless states has begun to arise during the last years. The topological nature of a crystalline lattice is rooted in the Bloch wave-functions $|u_n(\mathbf{k})\rangle$, where n labels the band index. The Berry phase γ_n [62] is computed from the closed line integral of the Berry connection (see appendix A.1 for a detailed derivation):

$$\mathcal{A}_n(\mathbf{k}) = -i\langle u_n(\mathbf{k})|\nabla_{\mathbf{k}} u_n(\mathbf{k})\rangle, \tag{1.7}$$

or the surface integral of the Berry curvature over the Brillouin zone:

$$\mathcal{F}_n(\mathbf{k}) = -i\nabla_{\mathbf{k}} \times \langle u_n(\mathbf{k})|\nabla_{\mathbf{k}} u_n(\mathbf{k})\rangle. \tag{1.8}$$

The stability of Weyl points is linked to an integer topological index, which is the reason why Weyl semimetals are considered topological materials. Their non-trivial topological structure is linked to the Berry curvature associated with a band-crossing point of definite chirality, which takes the form (see appendix A.2):

$$\mathcal{F}_{n,\chi}(\mathbf{k}) = n\chi\frac{\mathbf{k}}{2\mathbf{k}^3}. \tag{1.9}$$

In the vicinity of a Weyl node, the Berry curvature has the form of a magnetic monopole (see Figure 1.2). The sign of the charge is determined by the chirality χ of the point. Weyl nodes are sources and sinks of Berry curvature [63, 64], which prevents them to be eliminated: Weyl points move around in reciprocal

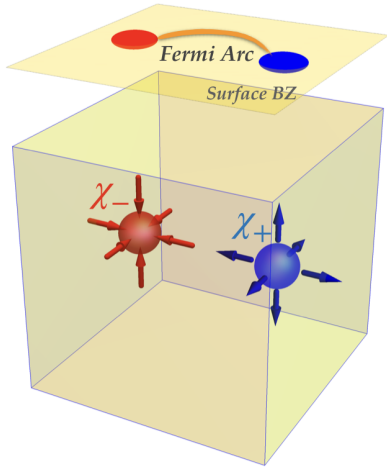

FIGURE 1.2: Schematic illustration of two single Weyl nodes with opposite chirality. Weyl nodes act as sources and sinks of Berry curvature. At the surface, the projections of the two Weyl nodes are connected by a Fermi arc.

space upon changing the parameters of the Hamiltonian, and eventually oppositely charged monopoles may annihilate when placed on top of each other. As shown by Nielsen and Ninomiya, the total monopole charge in the Brillouin zone has to be zero [65], which implies that the band-crossing points always come in pairs of opposite chirality.

1.3 Physical consequences of topology

Systems with gapless degrees of freedom have robust topological properties with defining topological invariants. Bulk degeneracies act as sources and sinks of Berry curvature, with a quantized Berry flux. In this section, we will explore the consequences of having solid-state systems with a non-trivial electronic band structure topology.

1.3.1 Topological surface states: Fermi arcs

In band insulators, non-trivial topology induces conducting states exponentially localized at the surface [66, 57]. Distinctive bound-states are also originated at the surfaces of gapless bulk materials as a consequence of their non-zero Berry curvature. Surprisingly, these states do not form a conventional closed Fermi surface, but form

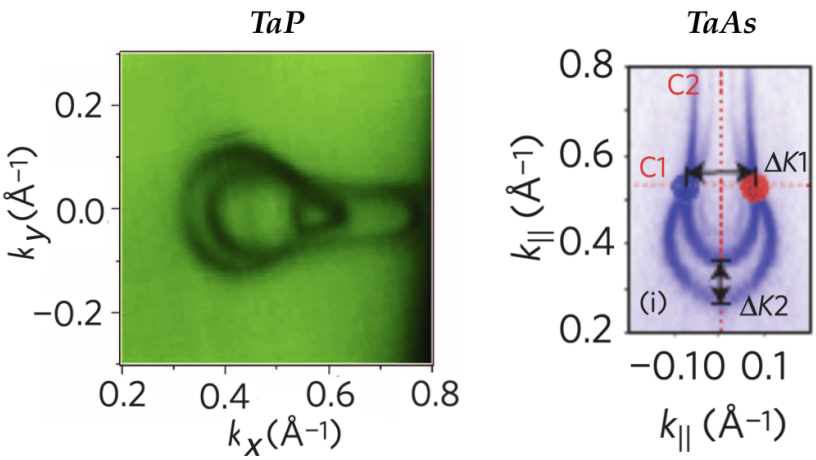

FIGURE 1.3: High-resolution ARPES Fermi surface maps in TaP *(left)* and TaAs *(right)* crystals, showing the presence of Fermi arc surface states. Adapted from Refs. [68, 69].

open "arcs" at the Fermi level (see Figure 1.2), which end at the projection of the degeneracy points onto the surface Brillouin zone [18, 19, 23, 67].

The existence of Fermi arcs carrying a non-trivial Chern number is used as an experimental signature of Weyl nodes in the bulk. Direct measurements of these surface states are made through angle-resolved photoemission spectroscopy (ARPES) studies (see Figure 1.3). Additionally, Fermi arcs are predicted to exhibit unusual quantum oscillations in magnetotransport measurements and quantum interference effects in scanning tunneling microscopy (STM) experiments, providing a variety of experimental probes of the surface states [70–72].

1.3.2 Chiral anomaly in Weyl semimetals

As mentioned at the beginning of section 1.1, the Dirac equation is split into two independent equations for the chiral components $\psi_\pm$ in the massless case. Since the two components do not mix, it follows that the charges associated to each chirality are separately conserved, and using Noether's theorem [73, 27] one can express individually classical conservation laws for the currents of left (−) and right (+) moving Weyl fermions. In particular, the axial vector current

$$J_5^\mu = J_+^\mu - J_-^\mu = \psi^\dagger \gamma^0 \gamma^\mu \gamma_5 \psi, \tag{1.10}$$

that corresponds to the difference between fermions with opposite chiralities, satisfies the continuity equation

$$\frac{\partial}{\partial x^{\mu}} J_5^{\mu} = 0. \tag{1.11}$$

Equation (1.11) arises as a result of the *axial* gauge symmetry,

$$\psi_+ \rightarrow \tilde{\psi}_+ = e^{+i\theta}\psi_+, \tag{1.12}$$

$$\psi_- \rightarrow \tilde{\psi}_- = e^{-i\theta}\psi_-. \tag{1.13}$$

The axial conservation law is no longer valid when quantizing the theory in the presence of external electric **E** and magnetic **B** fields. The gauge symmetry breaks at the quantum level, and the expectation value of the chiral currents becomes [74, 22]:

$$\partial_{\mu} J_{\chi}^{\mu} = \frac{\chi}{8\pi^2}\frac{e^2}{\hbar^2}(\mathbf{E}\cdot\mathbf{B}), \tag{1.14}$$

where χ is the chirality of the Weyl fermion. A classical symmetry that does not persist when the dynamics is quantized is referred as anomalous. Quantization processes normally involve divergent terms that are caused when the classical currents are substituted by local operators, leading to quantum anomalies when the regularization mechanism does not respect the classical symmetry [75]. The non-conservation of the chiral charge, referred as *chiral* anomaly, was essential to explain the decay process of the neutral pion into two photons [46, 45]. From the point of view of condensed matter field, Weyl systems show the chiral anomaly, which is associated with an enhancement of the magneto-conductivity in transport experiments [76–80].

A physical intuition of this effect can be given by considering a simple Weyl semimetal with two nodes of opposite chiralities. In the presence of an external, uniform magnetic field, the conical dispersion relation is split into a set of Landau levels. Each level is a one-dimensional dispersing mode along the direction parallel to the orientation of the magnetic field. What is particular of the Dirac systems is the presence of a zeroth level, which has a chiral dispersion relation independent of the magnitude of the magnetic field; $E_{0,\chi} = -\chi \mathrm{sign}(B) v_{\mathrm{F}} \hbar k$, where k is the momentum along the direction of the magnetic field (a detailed derivation of the relativistic Landau level spectrum will be reviewed in chapter 2). In the case considered, there are two counter-propagating chiral modes with opposite velocities (the band structure is sketched in Figure 1.4). If an electric field E is switched on along the same direction as the magnetic field, this field will accelerate the electronic charge $\hbar\dot{k} = -eE$ according to kinetic theory [81, 82]. In this way, the electric field is generating an inter-valley charge pumping at a rate described by Equation (1.14), giving rise to an electronic imbalance $\mu_5 = \mu_+ - \mu_-$ between nodes of opposite

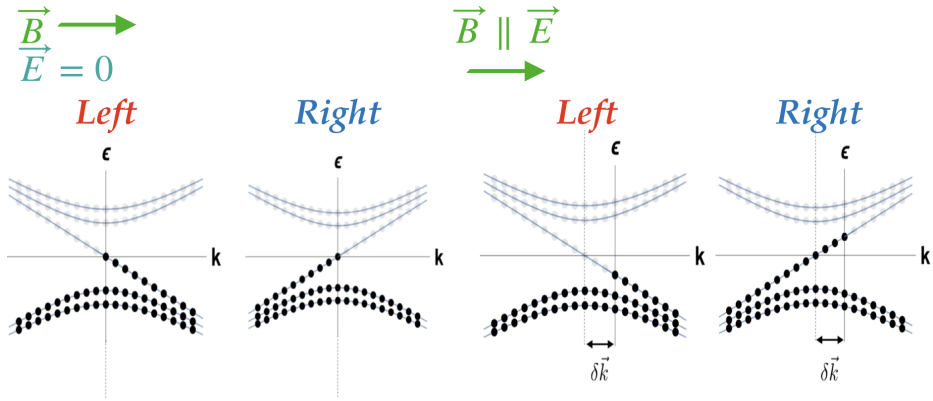

FIGURE 1.4: Representation of the energy spectrum of the left- and right-handed Weyl quasiparticles in the presence of a magnetic field. Filled (empty) states are represented by black (grey) dots. If an external electric field is applied parallel to the magnetic field, the electrons are displaced from their equilibrium positions in momentum space, pumping charge from one Weyl point to the other. Adapted from Ref. [21].

chirality. The total charge is conserved, while the difference between chiral charges is given by the following expression:

$$\partial_\mu J_5^\mu = \frac{1}{4\pi^2}\frac{e^2}{\hbar^2}(\mathbf{E}\cdot\mathbf{B}). \tag{1.15}$$

Signatures of the chiral anomaly are detected in transport experiments. This mechanism leads to a notable enhancement of the longitudinal conductivity as a function of the magnetic field, experimentally confirmed in Dirac and Weyl semimetals [78–80, 83, 84]. The chemical potential imbalance at two nodes of opposite chirality also gives rise to a dissipationless current along the direction of the magnetic field, the *chiral magnetic effect* [85–87], which was predicted in the quark-gluon plasma and observed in magneto-transport experiments in $ZrTe_5$ [88].

Recent experiments have shown evidences of other quantum anomalies as mixed axial-gravitational anomalies and scale anomaly [89–93]. These effects involve thermoelectric measurements in magnetic fields, which will be studied in detail in chapters 2 and 3.

1.3.3 Discrete symmetries and topological phases. Dirac semimetals

Crystal structures often have inversion and time-reversal symmetries. Discrete lattice symmetries have profound consequences on the band structure and topological properties of the material. In the case of lattices with an inversion center, the band structure satisfies the relation $E_{n,\sigma}(\mathbf{k}) = E_{n,\sigma}(-\mathbf{k})$, where σ denotes the spin of the energy band. On the other hand, non-magnetic materials (materials that possess time-reversal symmetry), the condition $E_{n,\uparrow}(\mathbf{k}) = E_{n,\downarrow}(-\mathbf{k})$ holds. When both of them are present, the combination $\mathcal{PT}$ is also a symmetry that leaves unchanged the momentum. Since $\mathcal{PT}$ is an antiunitary operation, the energy bands of $\mathcal{PT}$-symmetric materials have a Kramers degeneracy at every point in the reciprocal space [94]. This is not compatible with the condition for finding Weyl nodes at isolated points of the momentum space, which require non-degenerate bands in order to occur. The reason for such avoided crossing can be found on the topological character of the system: the Berry curvature satisfies the relation

$$\mathcal{F}_n(\mathbf{k}) = -\mathcal{F}_n(-\mathbf{k}) \tag{1.16}$$

if the system has time-reversal symmetry, and

$$\mathcal{F}_n(\mathbf{k}) = \mathcal{F}_n(-\mathbf{k}) \tag{1.17}$$

if it has spatial inversion symmetry [95]. Equations (1.16) and (1.17) imply that, if both symmetries are present, the Berry curvature vanishes identically at each point of the Brillouin zone: either time-reversal symmetry or inversion symmetry should be broken in order to get non-trivial topological bands.

Nevertheless, linear crossings are still possible in $\mathcal{PT}$-symmetric materials. Due to the presence of extra symmetry constraints, the degeneracy point becomes a four-fold degeneracy of the bands. Considering a crystal lattice whose Hamiltonian satisfies both time-reversal and inversion symmetries, a band crossing can only occur if two Weyl nodes with opposite chiralities are stabilized at the same crystal momentum, scenario described by the massless Dirac Hamiltonian[3]:

$$H = \begin{pmatrix} \hbar v_{\mathrm{F}} \sigma^j k_j & 0 \\ 0 & -\hbar v_{\mathrm{F}} \sigma^j k_j \end{pmatrix}, \tag{1.18}$$

[3]The most general $\mathcal{PT}$-invariant four-band Hamiltonian is given in terms of five 4×4 traceless gamma matrices $\hat{\gamma}^1, \ldots, \hat{\gamma}^5$ that satisfy the anticommutation relation $\{\hat{\gamma}^i, \hat{\gamma}^j\} = 2\delta^{ij}$; $H = \sum_i^5 \hat{\gamma}^i g_i(\mathbf{k})$. In 3+1-dimensional materials, this Hamiltonian is not robust against perturbations, and additional symmetries are required in order to get a four-fold degeneracy, as the number of parameters is not enough to make the functions $g_i(\mathbf{k})$ vanish [96].

which contains four linearly dispersing energy bands not topologically protected. A pair of Weyl nodes carrying opposite charges may annihilate each other when they are brought together, opening a gap in the electronic band structure. This gap can be avoided if the band crossing is protected by space-group symmetries of the lattice, in which case the *Dirac node* remains unaltered as a symmetry-protected degeneracy. The electronic excitations in the vicinity of this four-fold point are described by Equation (1.18), which yields a solid-state realization of the 3+1-dimensional massless Dirac equation. Materials supporting these kind of degeneracies at the Fermi level are called *Dirac semimetals*.

Dirac semimetals are expected to emerge at the phase transition between an ordinary and topological insulator when both time-reversal and inversion symmetries are present. The transition takes place when the Dirac fermion mass is equal to zero, constraint that is achieved either by fine tuning or with additional symmetries to force the gapless states at time reversal invariant momenta [97–100]. Along with this proposal, other possibilities has been uncovered. Specifically, Dirac nodes can be realized in materials with rotational symmetry, where two pairs of Weyl nodes merge at two $\mathbf{k}$ points lying along the rotation axis. Thus, each of the two points related by time-reversal symmetry hold two Weyl nodes of opposite chirality, defining two stable Dirac points. This type of Dirac semimetals have been realized experimentally in Na_3Bi and Cd_2As_3 compounds [13, 14, 101–104].

From Dirac to Weyl semimetals

After viewing Dirac semimetals as the stable merger of two Weyl points with opposite chirality, we can assert that two Weyl fermions with opposite charge emerge from breaking either time-reversal or inversion invariance in a four-fold degeneracy point. Using a covariant formalism, this is achieved by introducing the chiral vector $\gamma^5 b_\mu$ to the massless Dirac Lagrangian in the form [17, 64, 105, 106]:

$$\mathcal{L} = \hbar c \bar{\psi}(x) \left(i\gamma^\mu \partial_\mu + \gamma^\mu \gamma^5 b_\mu \right) \psi(x), \tag{1.19}$$

where $\bar{\psi} = \psi^\dagger \gamma^0$ and γ^5 is matrix defining the chirality operator described earlier (see Figure 1.5). Here b_μ couples to the chiral current as $j_5^\mu b_\mu$ as a gauge field. The time-component $\gamma^5 b_0$ is odd under parity, while the spatial-components $\gamma^5 b_j$ break time-reversal symmetry. The low-energy Hamiltonian for a node of chirality χ is:

$$H_\chi = \chi v_F \hbar \sigma^j (k_j + \chi b_j) + \chi v_F \hbar b_0 \mathbb{I}. \tag{1.20}$$

As a result, in materials where time-reversal symmetry has been broken (for instance, by doping the material with magnetic impurities), the axial gauge χb_j shifts the location of the energy cones with different chirality to different momenta, leading to

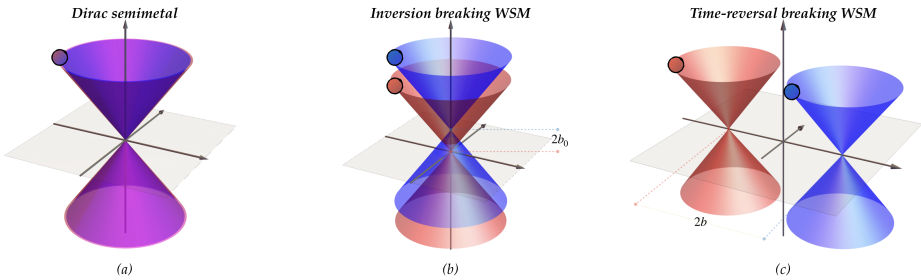

FIGURE 1.5: Pictorial representation of the different topological states. A four-fold degeneracy point *(a)* gives rise to a Weyl semimetallic phase by breaking either inversion *(b)* or time-reversal *(c)* symmetry.

a Weyl semimetal where the nodes are separated a distance $\Delta_{\mathbf{k}} = 2b$ in momentum space along the direction of $\mathbf{b}$; whereas in non-centrosymmetric semimetals the χb_0 term separates the Weyl cones a distance $\Delta_E = 2v_F\hbar b_0$ in energy space. The continuum model defined in Equation (1.20) will be broadly used throughout this thesis to characterize the behaviour of electronic excitations near the Weyl points.

Finally, we can see that the discrete symmetries of the microscopic model determine the minimum number of Weyl nodes present in any Weyl semimetals. Inversion symmetry requires that a Weyl node placed at momentum $\mathbf{k}$ must have a chiral partner with opposite topological charge at the point $-\mathbf{k}$ at the same energy [17, 18]. When time reversal symmetry is broken, this realizes the simplest scenario that allows for the minimum number of Weyl nodes. Conversely, when time-reversal symmetry is present, the time-reversal operation changes both the momentum and spin. The helicity (and thereby, the chirality) of the two time-reversed partners is the same and carry the same topological charge. This requires the presence of two additional Weyl partners in order to compensate their non-vanishing topology charge within the Brillouin zone [107]. Therefore, the total number of Weyl nodes is a multiple of four. Inversion-symmetry breaking materials are more experimentally accessible, as magnetic materials are less abundant. Time-preserving Weyl semimetals are expected to appear at the transition point from topological to trivial insulator, the four-fold degeneracy being lifted if inversion symmetry is lost.

1.4 Condensed matter realizations of Weyl semimetals

So far in this chapter we have discussed the different topological properties of band-crossing points and the necessary conditions to find such degeneracies in the bulk

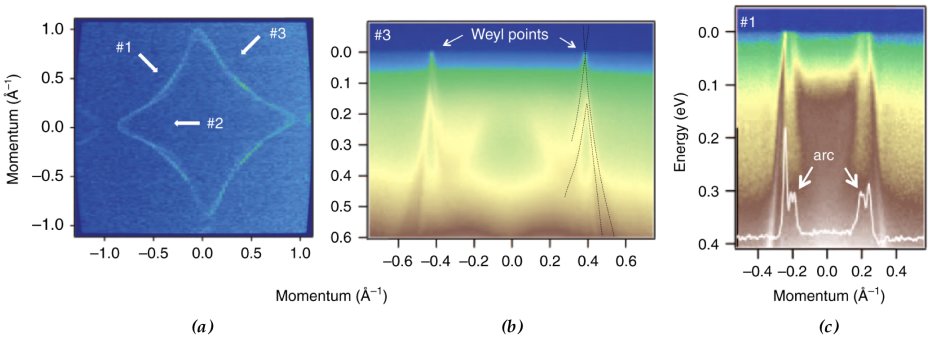

FIGURE 1.6: *(a,b)*: Fermi surface map of $YbMnBi_2$. Degenerate Dirac points are split due to the lack of time-reversal symmetry. *(c)*: Energy spectrum showing the presence of Fermi arcs. Adapted from Ref. [114].

spectrum of three-dimensional materials. Yet in order to observe Dirac physics in actual materials, the band touching points must be located at or very close to the Fermi energy, without any other state intervening at such level, which may screen the exotic effects stemming from the degeneracy points [21].

The first Weyl semimetals were described theoretically and postulated to occur in the pyrochlore iridates $A_2Ir_2O_7$ (where A is yttrium or a lanthanide) [17, 18]. Nevertheless, Weyl semimetals were first realized in the transition-metal monophophides TaAs, TaP, NbAs and NbP, with the subsequent observation of Fermi arcs with ARPES experiments [15, 16, 108–111, 69, 112, 113]. The complex structure of these materials give rise to a minimum of twelve pairs of Weyl nodes located at points with no particular symmetry in the Brillouin zone.

The pursuit of a time-reversal breaking Weyl materials with the minimum number of cones neatly separated in momentum space is a major research topic these days. Different works have reported the observation of such topological phase in non-collinear antiferromagnet Mn_3B (where B is Sn, Ir, Ge), a correlated metal that exhibits a large anomalous Hall and Nernst effect at room temperatures [115–119]; magnetic Heusler compounds [120–128]; and metallic $YbMnBi_2$ crystals, which develop a non-trivial magnetic response below 50K, giving rise to two pairs of Weyl nodes near the Fermi surface [114]. The Weyl points and Fermi arcs measured with ARPES technique are represented in Figure 1.6. The electronic structure shows that the Weyl points emerge at the boundary between electron and hole pockets, contrary to the standard point-like Fermi surface. This new type of Weyl semimetal is known as *Type-II* Weyl semimetals [129], which will be discussed in the next section.

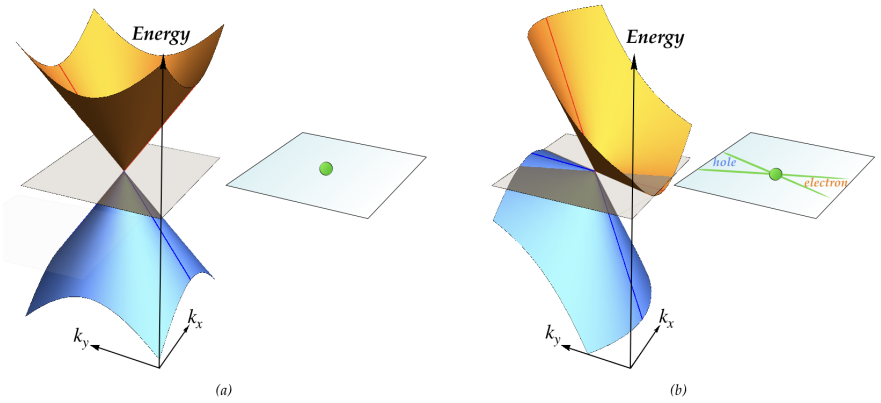

FIGURE 1.7: Schematic representation of Type-I *(a)* and Type-II *(b)* Weyl semimetals.

1.4.1 Electronic excitations in Weyl fermions. Beyond high-energy physics

The effective description of a model may not respect fundamental symmetries of nature that, in principle, must be preserved by any physical law. This freedom to formulate new "unrestricted" theories is justified as long as the model provides a faithful description of the system [130]. In particular, microscopic models in condensed matter are not restricted by the Lorentz symmetry, and provide a potential field for the discovery of exotic behaviours that do not have elementary analogues [131, 132].

One Lorentz invariance is not a requirement, we can generalize the expansion in Equation (1.5) with the term:

$$H = \hbar v_{ij}\sigma^i(\mathbf{k}-\mathbf{k}_*)^j + \hbar w_j \mathbb{I}(\mathbf{k}-\mathbf{k}_*)^j, \tag{1.21}$$

where the vector $w_j = \partial_j f_0|_{\mathbf{k}=\mathbf{k}_*}$, known as *tilt* velocity, breaks time-reversal and rotational invariance, and introduces an overall tilt in the cone-like dispersion relation. Weyl cones typically exhibit a tilted dispersion characterized by Equation (1.21). A sufficiently large $\mathbf{w}$ can induce an overlap in energy of the conduction and valence bands that cross at the Weyl point, giving rise to electron and holes pockets. When $|\mathbf{w}| > |\mathbf{v}_F|$, the Weyl cone is tipped over, leading to open Fermi surfaces and a metallic density of states. This novel phase is referred as Type-II Weyl semimetals [129], in contrast to Type-I Weyl semimetals with point-like Fermi surfaces (see Figure 1.7). Examples of a Type-II Weyl semimetals are WTe_2 and $MoTe_2$ crystals [133, 134].

1.4.2 Thermoelectric responses and topological materials

Thermoelectric materials have been an important field of activity during the last century, mostly due to their technological interest in heat-to-electricity conversion [135–137]. One important obstacle is their low efficiency, and current efforts are focused on get over these limitations. The strength of the thermoelectric effect is characterized by the Seebeck effect, a phenomenon where an applied thermal bias generates a parallel voltage between the hot and cold sides of the sample. The Seebeck coefficient S is defined as the ratio between the voltage difference and the temperature bias, while the absolute value of S is the thermopower [138]. The effectiveness of a thermoelectric material is quantified by its thermoelectric figure of merit [139] :

$$\mathcal{Z}T = \sigma S^2 T/\kappa \tag{1.22}$$

where σ is the electrical conductivity, T is the temperature of the system and κ is the thermal conductivity. The condensation of electrons and holes on the cold side in a conductive solid is the primary issue to achieve a large thermopower, as their opposite charges counterbalance each other reducing the net contribution to the induced voltage. For that reason, the most efficient thermoelectric materials up to date are doped semiconductors [135].

In the presence of an external magnetic field orthogonal to the temperature gradient, electronic carriers flowing from the hot to the cold side are deflected due to the Lorentz force, generating a transverse electric field perpendicular to both the magnetic field and thermal bias. This thermoelectric phenomenon known as *Nernst* effect was first discovered by Ettingshausen and Nernst when exploring the properties of the compensated semimetal Bismuth. Unlike the zero field case, the magnetic field bends the trajectories of electrons and holes in opposite directions, inducing a net contribution from both type of carriers (see Figure 1.8). Compensated semimetals, characterized by a small Fermi surface and large mean-free path, exhibit a large Nernst signal, as demonstrated in Bismuth and graphite [140, 141].

Historically, Seebeck-based thermoelectric devices have attracted more attention than their Nernst-based partners, motivated principally by the necessity to include an external magnetic field in order to get the emergent potential. Additionally, localization effects are enhanced by the magnetic field, making these materials less attractive. Recent interest in the thermoelectric properties of materials with a non-trivial topology has arisen based on their unconventional band structure, which can circumvent the inherent limitations of conventional materials [142–144]. In addition, the thermoelectric response coefficients shed light on the electronic structure of the materials, providing a new mechanism to study the nature of Dirac quasiparticles and a unique signature for the presence of Dirac bands [123, 144]. Topological

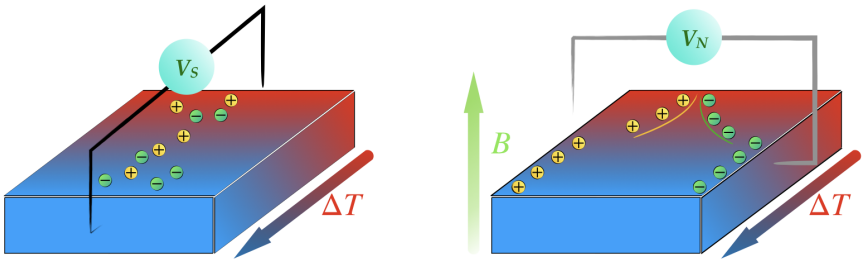

FIGURE 1.8: Illustration of Seebeck *(left)* and Nernst *(right)* effects. The mutual cancellation between oppositely charged particles may be circumvented in the presence of a perpendicular magnetic field, which deflects electrons and holes in opposite directions.

Weyl and Dirac semimetals display large anomalous Nernst thermopower values[4] which are ascribable to the non-vanishing Berry curvature associated with the Weyl points near the Fermi energy [148, 149]. The reported numbers are beyond any experimental value obtained in conventional ferromagnets [123, 124, 150–152].

Based on this, topological semimetals are promising candidates to obtain high-performance thermoelectric materials. The chiral zeroth Landau level with an energy-independent density of sates provides a mechanism to create huge electronic entropy, while the topological protection of the nodes avoids localization effects. The theoretical prediction that Weyl and Dirac semimetals would exhibit a large, non-saturating thermopower in quantizing magnetic fields [153, 154] was confirmed experimentally in Refs. [155, 156]. In chapters 2 and 3 we will explore the consequences of quantum anomalies on the thermoelectric properties and phenomenological relations of Dirac and Weyl semimetals.

1.4.3 Strain-induced pseudo-electromagnetic fields

The study of the influence of lattice deformations on the electronic properties of crystals is a central topic in condensed matter physics. A distinguished example is that of superconductivity, where the lattice vibrations of the system couple with the electrons to mediate in their attractive interaction [157]. In the case of Weyl systems, a special kind of electron-phonon coupling arises in the form of a pseudo-gauge field

[4]Temperature gradients applied to time-reversal breaking materials, a voltage bias perpendicular to the heat flow and the magnetization vector is generated in the sample at zero applied magnetic field. This is the *anomalous* Nernst effect [145, 146], in analogy with the anomalous Hall effect. It has been proven that the anomalous Nernst and Hall effects are intimately related to the net Berry curvature in topological matter [95, 147].

which, in combination with the chiral anomaly, gives rise to unexpected physical responses [158–162].

Emergent elastic pseudo-magnetic fields were first observed on graphene [158, 159, 163], where the mechanical strain acts as a vector potential that couples with opposite sign to the two valleys **K** and **K'**. Strain-induced electromagnetic fields sensitive to the chirality of the node were also extracted in the low-energy regime of Weyl quasiparticles in [161]. In this way, Dirac matter establishes, once more, an unexpected connection between two unrelated fields: elastic deformations of the lattice's parameters and axial gauge theories, giving rise to a unified description of different physical phenomena.

The origin of gauge fields can be traced back to the separation, either in momentum or energy, of the Weyl nodes. Considering a simple model of two Weyl nodes of opposite chirality and separated a distance $2b$ in momentum and $2v_{\mathrm{F}}\hbar b_0$ in energy, their low-energy Hamiltonian is given by Equation (1.20), $H_\chi = \chi v_{\mathrm{F}}\hbar\sigma^j(k_j + \chi b_j) + \chi v_{\mathrm{F}}\hbar b_0$. The vector **b** enters in the Hamiltonian in the same way as an axial vector potential $\mathbf{A}_\chi$. The effect of strain is to induce local variations in the vector **b**, which allows to define an emergent, elastic-magnetic field:

$$\mathbf{B}_5 = \frac{\hbar}{e}\boldsymbol{\nabla}\times\mathbf{b}. \tag{1.23}$$

The component b_0, which separates the cones in opposite directions in energy, acts as a scalar potential in the Hamiltonian, leading to the definition of the pseudo-electric field:

$$\mathbf{E}_5 = \frac{\hbar}{e}\left(-v_{\mathrm{F}}\boldsymbol{\nabla}b_0 - \partial_t\mathbf{b}\right). \tag{1.24}$$

The four-vector b_μ is an intrinsic parameter of the topological semimetal that enters in some response functions as the anomalous Hall effect [147]

In a tight binding approximation, elastic deformations modify the atomic position on the lattice, varying the overlap integral (the distance and the relative orientation) between atomic orbitals that, due to their topological stability, only induces a displacement of the location of the Weyl nodes [161, 162, 164] that results in the emergence of pseudo-electromagnetic fields [161]. As an example, the effect of applying torsion to a crystal wire has been explored in Ref. [165]. This geometry leads to the formation of a uniform pseudo-magnetic field $\mathbf{B}_5$ in the bulk, which breaks the energy spectrum of the Weyl semimetal into Landau levels. The same effect is expected when bending thin films (or nanowires) of Weyl semimetal, resulting in quantum oscillations driven by elastic deformations [166]. The recognition of strain-driven gauge fields described in Ref. [161] was followed by a number of works discussing their physical consequences [167–172]. What these results highlight is the intrinsic interplay between real and strain-induced magnetic fields, as both **B** (real) and $\mathbf{B}_5$

(elastic) ignite the same physical phenomena; the quantization of the band structure into Landau levels. The case of axial gauge-fields has important consequences on the chiral anomaly and chiral magnetic effect.

In the presence of an external electromagnetic field and axial pseudo-electromagnetic field generated from strain, the chiral anomaly reads [22, 173]:

$$\partial_\mu J_5^\mu = \frac{1}{2\pi^2} \left(\mathbf{E} \cdot \mathbf{B} + \mathbf{E}_5 \cdot \mathbf{B}_5 \right). \tag{1.25}$$

The consequences of having emergent electromagnetic fields in transport experiments are associated to the enhancement in the longitudinal conductivity as a function of the pseudo-magnetic field, as observed in the original chiral anomaly [165].

Related to the chiral magnetic effect, the lowest Landau levels of opposite chiralities are co-propagating modes in the presence of axial-magnetic fields. This results in a finite, strain-induced chiral magnetic effect proportional to $\mathbf{B}_5$ [173–175]. Alternatively, spatial variations of b_0 are suggested to create a chiral chemical potential imbalance between the two nodes and ignite the anomaly in the presence of real magnetic fields [162].

Strain also affects other parameters of the Hamiltonian, such as the Fermi or tilt velocities. The implications of these kind of effects will be analyzed in chapters 4 and 5.

Chapter 2

Thermoelectric transport in Dirac and Weyl semimetals

2.1 Introduction

Studying the response of a system to an external (maybe time-dependent) perturbation is a classical tool widely used to characterize condensed matter systems. For perturbations that are small in comparison to some characteristic length of the system, the response can be expanded in a power series of the perturbation, and the linear order is proportional to the field itself. Linear response theory is devoted to compute and understand the physical properties of the proportionality coefficient between the perturbation and the physical response [49, 176, 177]. One example is the electronic response of a metal to an applied electric field, where, in the linear regime, the emergent current is proportional to the external field.

In addition, when a temperature difference is induced in a metal (or any material with free charged particles), the flow of charged carriers from the hot to the cold side gives rise to an electric current. Linear response in thermoelectric transport theory allows to write electric and thermal currents generated by potential and thermal gradients as [138, 32]:

$$\begin{aligned} J^i &= L_{EE}^{ij} E_j + L_{ET}^{ij} \nabla_j T \\ J_Q^i &= L_{TE}^{ij} E_k + L_{TT}^{ij} \nabla_j T \end{aligned} \tag{2.1}$$

The proportionality coefficient $\boldsymbol{L}_{ET}$, connecting the gradient of temperature with the electric current, is the thermoelectric coefficient. For further details about kinetic theory, we refer the Refs. [34, 138, 178].

A very active area of research in the context of the novel 3D topological semimetals is centered on the emergence of anomaly induced transport phenomena [86, 179, 76]. A quantum anomaly arises when a continuum symmetry of the classical action [73, 27] cannot survive the quantization process and the corresponding conservation law is not longer valid. The physical consequences of having quantum anomalies were first explored in the construction of quantum field theory to describe elementary particles [74] and played an important role in grand unification and string theory. Nowadays, the interest on anomalies and anomaly-related transport has shifted to emergent condensed matter systems which support low-energy descriptions akin to their quantum field theory partners [86, 179]. After an intense and successful analysis of the consequences of the chiral anomaly on magnetoelectric transport [76, 78, 79], the interest has shifted to gravitational effects, especially those of the mixed axial-gravitational anomaly [89, 90]. These phenomena involve thermoelectric measurements in magnetic fields.

Thermoelectric transport has been a research topic of major activity and excitement both in physics and technology, as well as a tool to study and characterize the electronic properties of the materials. As mentioned in chapter 1, from the early research it was known that semiconductors and semimetals are the best candidates to generate large figures of merit in thermopower, with bismuth, an almost compensated semimetal, holding the record for metallic compounds [180]. Dirac and Weyl semimetals belong naturally to the family of good thermoelectric materials and their thermoelectric properties are now at the center of interest in experimental and theoretical research [123, 142, 143, 148, 181, 182]. Giant values of the anomalous Nernst effect associated with the non-trivial Berry phase of the materials are been systematically reported in the newly discovered magnetic Weyl semimetals [150, 151, 124]. Additionally, large thermopower values have been experimentally measured in these materials which are not restricted by the limitations held by ordinary metals [155, 156], opening potential new horizons in the field.

In a recent publication [93], it has been shown the emergence of a new anomalous electric current originated by a less-known quantum anomaly, the conformal anomaly, related to metric deformations [91]. It gives rise to a special contribution to the Nernst signal which remains finite at zero temperature and chemical potential.

The way in which gravity appears in condensed matter physics can be traced back to the problem of defining thermodynamic equilibrium in curved backgrounds [183], and is surprisingly connected to the thermoelectric phenomena. As will be argued below, the relation between these two seemingly unrelated fields was made possible by the Luttinger theory of thermal linear transport [184].

In this chapter, we will analyze with a Kubo calculation the thermoelectric coefficient of the massless Dirac systems in a magnetic field at zero chemical potential and zero temperature. The regime of zero temperature and chemical potential, where

the unusual prediction in Ref. [93] lies, prevents the use of a Boltzmann approach and the comparison with existing results. The chapter is organized as follows. First, we present an introductory overview of thermoelectric transport and linear response theory, highlighting the role of temperature gradients and magnetization currents. Next, we describe the effective continuum model for the Dirac and Weyl semimetals and discuss the specific expressions for the current and energy-momentum tensor. The chapter ends with the computation of the thermoelectric tensor and a summary of the main results. The analysis is extended to include finite temperature and chemical potential effects[1].

2.2 Linear response theory. Thermoelectric tensor

In linear response theory [176], when the action of a system is perturbed by a local source $F(t)$ which couples to an observable as $H_{\text{pert}}(t) = F(t)B$, the change in the expectation value of any operator A is assumed to be linear in the perturbing source: $\delta\langle A(t)\rangle = \int \mathrm{d}t' \chi(t,t')F(t')$. Mathematically, the response function χ is expressed as the correlation function between the response and the external perturbation [49]:

$$\chi(t) = -\frac{i}{\hbar}\int_{-\infty}^{\infty} \mathrm{d}t' \Theta(t-t') \left\langle [A(t), H_{\text{pert}}(t')] \right\rangle_0 , \tag{2.2}$$

where A is the observable operator arising from the external perturbation H_{pert}, and the brackets $\langle \cdots \rangle_0$ indicate the equilibrium expectation value with respect the unperturbed Hamiltonian H_0. The main hypothesis supporting the above expression is the adiabatic evolution of the system: the initial states are distributed according to the usual Boltzmann distribution, which implies that the n-th eigenstate $|\psi_n\rangle$ of the unperturbed Hamiltonian is occupied with a probability $P_n = \exp[-\beta E_n]/\mathcal{Z}$, where $\mathcal{Z} = \sum_n e^{-\beta E_n}$ is the canonical partition function. After the external perturbation is switched on, the system starts to evolve according to the total Hamiltonian $H_{\text{tot}}(t) = H_0 + H_{\text{pert}}$. A key assumption is that the occupation probabilities P_n remain constant (the states are described by the same occupation probabilities), and the transitions between orthogonal states are forbidden. The time-evolution of the system is governed by the Schrödinger equation:

$$i\hbar \frac{\partial}{\partial t}|\psi_n(t)\rangle = H_{\text{tot}}(t)|\psi_n(t)\rangle, \tag{2.3}$$

[1]This chapter is based on "Vicente Arjona, Maxim N. Chernodub and María A.H. Vozmediano, *Fingerprints of the conformal anomaly in the thermoelectric transport in Dirac and Weyl semimetals*, Physical Review B **99**, 235123 (2019)".

with P_n being an indenpendent function of time.

Correlation functions are extensively used for tackling problems where the perturbation can be described as a local perturbation in the Hamiltonian (mechanical formulation). The standard example is the computation of the electrical conductivity, where the electromagnetic potential couples directly as a source term to the electronic current in the Hamiltonian. In this case, the conductivity tensor is proportional to the current-current correlation function. The problem of using a statistical variable (such as the temperature) as a (local) source coupled to an energy current was solved by Luttinger [184]. Based on previous analyses by Tolman and Ehrenfest trying to define thermal equilibrium in a curved space [183], the underlying idea behind this formulation is that the thermal gradient moving the system out of equilibrium is compensated by a (perhaps fictitious) gravitational potential. This is reminiscent of Einstein's relationship between the diffusion (statistical) and the conductivity (mechanical) coefficients. In this case, the gravitational potential, coupled to the energy density, is the local source of the energy currents.

In the following section, we will illustrate how the gravitational potential is related to thermal gradients when the system is at thermodynamic equilibrium.

2.2.1 Luttinger's relationship for thermal gradients

Following the Refs. [184, 185], we review the key steps to obtain the relationship between the gravitational potential and the temperature gradient. Consider the response function to an external electrostatic and gravitational potentials ϕ and ψ, respectively. These external fields couple to the particle and energy densities in the form:

$$H = \int \mathrm{d}\mathbf{r} \left[h_0(\mathbf{r}) + \phi(\mathbf{r}) n(\mathbf{r}) + \psi(\mathbf{r}) h_0(\mathbf{r}) \right], \tag{2.4}$$

where h_0 describes the unperturbed system. Considering that the scale of the variation is large in comparison with the length of the system, one can split the system into small, independent sub-blocks that are close to local thermodynamic equilibrium. Each of those subsystems can be described by local conserved densities (energy and particle densities) and thermodynamic parameters (local temperature $T(\mathbf{r})$, chemical potential $\mu(\mathbf{r})$ and entropy density $s(\mathbf{r})$), which are functions of the conserved quantities. The extensive thermodynamic values are the result of integrating the local densities over the sample. The total energy, entropy and particle number are [185]:

$$E = \int \mathrm{d}\mathbf{r} \left[\epsilon(\mathbf{r}) + \phi(\mathbf{r}) n(\mathbf{r}) + \psi(\mathbf{r}) \epsilon(\mathbf{r}) \right], \tag{2.5}$$

$$S = \int \mathrm{d}\mathbf{r}\; s[\epsilon(\mathbf{r}), n(\mathbf{r})], \tag{2.6}$$

$$N = \int \mathrm{d}\mathbf{r}\; n(\mathbf{r}). \tag{2.7}$$

Thermodynamic equilibrium is reached when the entropy (or the sum of the entropies of each sub-block) is maximized [186]. This condition is written mathematically as [94]:

$$\delta\{S - \beta(E - \xi N)\} = 0, \tag{2.8}$$

where $\xi = \phi + \mu$ is the electrochemical potential and $\beta = T^{-1}$ is the temperature of the system (both being space independent functions of the unperturbed system). The functional variation given in Equation (2.8) defines the density matrix ρ for the equilibrium state. Varying Equation (2.8) with respect the energy and particle density, one gets the relations:

$$T^{-1}(\mathbf{r}) = \beta\{1 + \psi(\mathbf{r})\}, \tag{2.9}$$

$$\mu(\mathbf{r})/T(\mathbf{r}) = \beta\{\xi - \phi(\mathbf{r})\}, \tag{2.10}$$

where the partial derivatives have been replaced by the (local) definitions of the intensive parameters:

$$T^{-1} = \left.\frac{\partial s}{\partial \epsilon}\right|_n, \quad \mu = -T \left.\frac{\partial s}{\partial n}\right|_\epsilon. \tag{2.11}$$

The thermodynamic equilibrium conditions are defined by

$$\boldsymbol{\nabla}\left(\frac{1}{T}\right) - \frac{\boldsymbol{\nabla}\psi}{T} = 0, \tag{2.12}$$

$$\boldsymbol{\nabla}\left(\frac{\mu}{T}\right) + \frac{\boldsymbol{\nabla}\phi}{T} = 0, \tag{2.13}$$

which provide a relationship between the linear response coefficients of statistical and mechanical variables; since electric currents are not allowed to flow in a system at thermal equilibrium, external fields must be introduced as suggested by Equations (2.12) and (2.13). Equation (2.12) states that a gradient of temperature moving the system out of equilibrium is compensated by a gravitational potential (see Figure 2.1). The expressions given in Equations (2.12) and (2.13) were derived in the "slow case" regime [184], where the external fields are slowly applied so the system is able to achieve an equilibrium state.

The correlation functions of the statistical variables are determined in the "rapid case", where the system remains homogeneous since it is unable to adjust to the rapid oscillatory behaviour of the external fields. Despite the system cannot reach

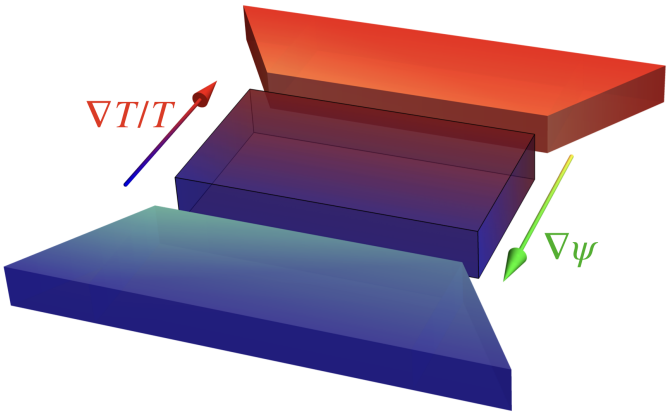

FIGURE 2.1: A gradient of temperature is compensated by a gravitational potential when the system is at thermal equilibrium.

a equilibrium state, the variations of the external perturbations are slow enough to consider the charge and energy densities as conserved quantities. Accordingly, the chemical potential and the temperature are space independent variables, the external potentials ϕ and ψ being the only perturbative fields. The emergent charge and energy currents are computed with the general Kubo formula:

$$J^i = N_{11}^{ij}\partial_j\phi + N_{12}^{ij}\partial_j\psi \tag{2.14}$$

$$J_E^i = N_{21}^{ij}\partial_j\phi + N_{22}^{ij}\partial_j\psi \tag{2.15}$$

where the transport coefficients $N_{\alpha\beta}^{ij}$ are the standard correlation functions described in Equation (2.2).

Proceeding with the general case, we consider arbitrary fields and local variables. As mentioned above, the perturbative fields should enter in the combination defined by Equations (2.12) and (2.13). The transport equations for statistical variables read:

$$J^i = N_{11}^{ij}\left[\partial_j\phi + T\partial_j\left(\frac{\mu}{T}\right)\right] + N_{12}^{ij}\left[\partial_j\psi + \frac{\partial_j T}{T}\right] \tag{2.16}$$

$$J_E^i = N_{21}^{ij}\left[\partial_j\phi + T\partial_j\left(\frac{\mu}{T}\right)\right] + N_{22}^{ij}\left[\partial_j\psi + \frac{\partial_j T}{T}\right] \tag{2.17}$$

Once the linear response coefficients for the statistical variables are formulated, the auxiliary mechanical fields can be set to zero.

2.2.2 Correlation function for thermal perturbations

If one considers a weak gravitational field, the gravitational potential is written in terms of the metric tensor:

$$g_{00} = 1 + 2\psi \tag{2.18}$$

The latter naturally couples to the energy-momentum tensor $T^{\mu\nu}$, which is defined as the response to variations of the metric. The corresponding perturbative Hamiltonian is:

$$H_{\text{pert}}(t) = T^{00}(t) g_{00}(t) \tag{2.19}$$

The electric current generated as a response to this perturbation is given by the expression:

$$\left\langle J^i \right\rangle (\mathbf{r}, t) = \int_{-\infty}^{\infty} \mathrm{d}\mathbf{r}' \mathrm{d}t' \left\{ \frac{-i}{\hbar} \Theta(t - t') \left\langle J^i(\mathbf{r}, t) . T^{00}(\mathbf{r}', t') \right\rangle \right\} g_{00}(\mathbf{r}', t') \tag{2.20}$$

The function given in Equation (2.20) is still not yet equivalent to the current generated by thermal perturbations (proportional to $\boldsymbol{\nabla}\psi$). To get the *spatial derivative* of the metric tensor, we use the conservation law of the energy-momentum tensor to express the energy component as a function of the momentum densities:

$$T^{00}(\mathbf{r}, t) = -\int_{-\infty}^{t} \mathrm{d}t' v_{\mathrm{F}} \partial_i T^{0i}(\mathbf{r}, t') \tag{2.21}$$

where we have introduced the Fermi velocity to adapt the calculation to the case of Dirac materials. The adiabatic hypothesis allows us to assume that the system is unperturbed at $t = -\infty$. Introducing Equation (2.21) in Equation (2.20) and integrating by parts, the expectation value of the vector current is:

$$\left\langle J^i \right\rangle (\mathbf{r}, t) = \int_{-\infty}^{\infty} \mathrm{d}\mathbf{r}' \mathrm{d}t' \int_{-\infty}^{t'} \mathrm{d}t'' \left\{ \frac{-i v_{\mathrm{F}}}{\hbar} \Theta(t - t') \left\langle J^i(\mathbf{r}, t) . T^{0j}(\mathbf{r}', t'') \right\rangle \right\} \partial_j g_{00}(\mathbf{r}', t') \tag{2.22}$$

The last expression represents the emergent current induced as a response to a thermal gradient computed via the Kubo formula. Using the translational invariance of the system, the electric current reads:

$$\left\langle J^i \right\rangle (\mathbf{q}, \omega) = \chi^{ij}(\mathbf{q}, \omega)(i q_j) g_{00}(\mathbf{q}, \omega) \tag{2.23}$$

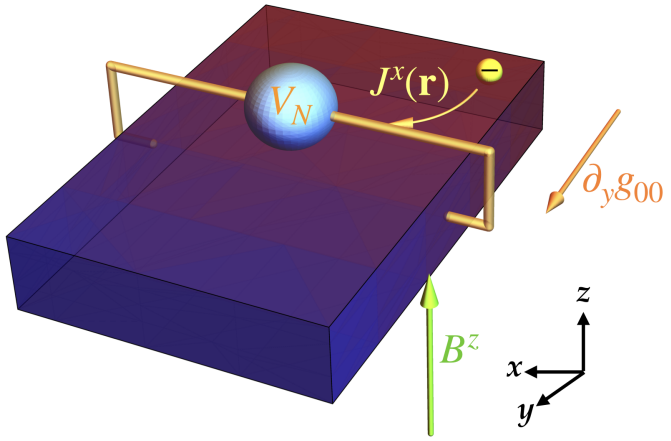

FIGURE 2.2: The setup of the thermoelectric effect. A transverse current $J^x(\mathbf{r})$ is generated perpendicular to both the magnetic field B^z and the gradient of temperature.

where χ^{ij} is the usual Fourier transform to momentum space of the response function:

$$\chi^{ij}(\mathbf{q},\omega) = (2\pi)^3 \int_{-\infty}^{\infty} \mathrm{d}t\, e^{i\omega(t-t')} \int_{-\infty}^{t'} \mathrm{d}t'' \left\{ \frac{-iv_{\mathrm{F}}}{\mathcal{V}\hbar} \Theta(t-t') \langle \left[J^i(\mathbf{q},t), T^{0j}(-\mathbf{q},t'') \right] \rangle \right\} \quad (2.24)$$

2.3 Thermoelectric response function of Dirac and Weyl semimetals

As mentioned in chapter 1, the low-energy excitations around a non-trivial band crossing of a Dirac semimetal are described by the massless Dirac equation in three space dimensions. Using the Weyl basis, the Hamiltonian splits into two Weyl nodes of definite chirality. In Dirac semimetals, the two chiralities are superimposed in momentum space and a mass term can arise mixing the two chiralities unless the band-crossing point is protected by crystal symmetries. In Weyl semimetals, the two chiralities are separated either in momentum or energy, which breaks either $\mathcal{T}$ or $\mathcal{P}$, respectively, and the Berry curvature makes the Weyl points very robust against perturbations.

The conformal invariance of the classical system implies that no dimension-full parameter can enter into the description of the system. Our model will generically be that of a massless Dirac semimetal, as used in Ref. [93]. We perform the calculations

for each Weyl fermion and ensure that no cancellation occurs due to the contribution of opposite chiralities. Once this is confirmed, the result will equally apply to Weyl semimetals which, eventually, can receive additional contributions from the separation of the Weyl points.

To analyze the anomaly-induced Nernst current, we consider a Dirac semimetal in an external magnetic field perpendicular to a gradient of temperature. A transverse current will be generated orthogonal to both the applied magnetic field and temperature gradient. Without loss of generality, we take the z-axis along the magnetic field, and the direction of the thermal perturbation as the y-axis, as illustrated in Figure 2.2.

2.3.1 Effective low-theory for Dirac and Weyl particles in a magnetic field

The low-energy model that characterizes the quasiparticle excitations around one Weyl cone in a magnetic field is:

$$H_s = s v_{\mathrm{F}} \sigma^i (p_i + e A_i) \tag{2.25}$$

where $s = \pm 1$ describes the chirality of the node, p_i is the momentum operator and $e = |q|$ is the charge of the electron. Fermions are coupled to the vector potential A_i via the minimal coupling prescription. Choosing the Landau gauge $A_x = -By$ (the final result is independent of this election), Equation (2.25) reads:

$$s v_{\mathrm{F}} \begin{pmatrix} p_z & p_x - eBy - ip_y \\ p_x - eBy + ip_y & -p_z \end{pmatrix} \begin{pmatrix} \varphi_1(\mathbf{r}) \\ \varphi_2(\mathbf{r}) \end{pmatrix} = E \begin{pmatrix} \varphi_1(\mathbf{r}) \\ \varphi_2(\mathbf{r}) \end{pmatrix} \tag{2.26}$$

This equation resembles the Hamiltonian of a quantum harmonic oscillator. Defining the usual ladder operators

$$a = \frac{1}{\sqrt{2}}(p_x - eBy + ip_y) \quad \text{and} \quad a^\dagger = \frac{1}{\sqrt{2}}(p_x - eBy - ip_y), \tag{2.27}$$

the spectrum of the Hamiltonian is quantized into Landau levels:

$$\begin{aligned} E_{k_z m s} &= \mathrm{sign}(m) v_{\mathrm{F}} \left[2e\hbar B|m| + \hbar^2 k_z^2 \right]^{1/2} \\ E_{k_z 0 s} &= -s v_{\mathrm{F}} \hbar k_z . \end{aligned} \tag{2.28}$$

The band index m runs over all integer numbers, except the zero level. The chiral mode has a linear dispersion relation with opposite sign for each node, while the rest, with a quadratic dispersion relation, are doubly degenerated. The eigenfunctions of

the system are:

$$\varphi_{\mathbf{k}ms}(\mathbf{r}) = \frac{e^{ik_x x}e^{ik_z z}}{\sqrt{L_x L_z}} \frac{e^{-(y-k_x l_B^2)^2/2l_B^2}}{\sqrt{\alpha_{k_z ms}^2+1}} \begin{pmatrix} \frac{\alpha_{k_z ms}}{\sqrt{2^{M-1}(M-1)!\pi^{1/2}l_B}} H_{M-1}\left[\frac{y-k_x l_B^2}{l_B}\right] \\ \frac{1}{\sqrt{2^M M!\pi^{1/2}l_B}} H_M\left[\frac{y-k_x l_B^2}{l_B}\right] \end{pmatrix}, \tag{2.29}$$

with

$$\alpha_{k_z ms} = \frac{-\sqrt{2eB\hbar|m|}}{E_{k_z ms}/sv_F - \hbar k_z}. \tag{2.30}$$

$l_B = [\hbar/eB]^{1/2}$ is the magnetic length, capital letters refer to the absolute value of band index, $H_m(x)$ are the Hermite polynomials of order n, and the factor $(\alpha_{k_z ms}^2+1)^{1/2}$ is the wave-function normalization (setting $k_z = 0$, one notices that the standard $\sqrt{2}$ factor of graphene is recovered, since $\alpha_{k_z ms} = \pm 1$). The number of states having the same energy is given by the different values of k_x that are allowed in that level. This quantity can be estimatedconsidering our particles confined inside a rectangular box with finite dimensions L_x, L_y, L_z. The centre of motion of the electron is restricted to the size of the box, $0 \leq y_c \leq L_y$, where $y_c = k_x l_B^2$. The latter relation imposes an upper bound for k_x:

$$0 \leq k_x \leq \frac{L_y eB}{\hbar} \tag{2.31}$$

Assuming periodic boundary conditions ($e^{ik_x L_x} = 1$), the degeneracy of each Landau level is given by the expression:

$$N = \frac{eBL_x L_y}{h}. \tag{2.32}$$

2.3.2 Current and energy-momentum operators

The current operator is defined as the functional derivative of the Hamiltonian with respect to the gauge vector $\mathbf{A}$[2]:

$$\delta H = e \int \mathrm{d}\mathbf{r}\, \mathbf{J}\delta\mathbf{A}. \tag{2.33}$$

The current operator (in second quantization) for the Hamiltonian in Equation (2.25) reads:

$$J^x(\mathbf{r},t) = esv_F \Psi^\dagger(\mathbf{r},t)\sigma^x\Psi(\mathbf{r},t). \tag{2.34}$$

[2]The electric current can also be derived using the Noether's theorem. Systems invariant under a $U(1)$ phase rotation have associated a time independent charge Q and a charge current vector J^μ satisfying the continuity equation $\partial_\mu J^\mu = 0$ [27].

According to Noether's theorem [73], a continuum symmetry of a classical action gives rise to conserved currents and charges. Systems that are invariant under spacetime translations have associated four conserved currents [27]:

$$T^{\mu}{}_{\nu} = \frac{\partial \mathcal{L}}{\partial(\partial_\mu \phi)} \partial_\nu \phi - \delta^{\mu}_{\nu} \mathcal{L}. \tag{2.35}$$

Equation (2.35) represents the canonical energy-momentum tensor, which has associated two conserved quantities; the energy (associated to time translations) and the momentum (associated to spatial translations). The energy-momentum tensor is defined in general relativity as $T^{\mu\nu} \sim \delta S / \delta g_{\mu\nu}$, quantity that is manifestly symmetric [50], while the definition given in Equation (2.35) is certainly not. In the rest of the calculation we will use the symmetrized version of the tensor[3]:

$$T^{\mu}{}_{\nu} = \frac{1}{2} \frac{\partial \mathcal{L}}{\partial(\partial_\mu \phi)} \partial_\nu \phi + \frac{1}{2} \frac{\partial \mathcal{L}}{\partial(\partial_\nu \phi)} \partial_\mu \phi - \delta^{\mu}_{\nu} \mathcal{L}, \tag{2.36}$$

which for the action associated to the Hamiltonian in Equation (2.36) is:

$$T^{0y}(\mathbf{r}, t) = \frac{-i\hbar}{2} \left[v_{\mathrm{F}} \Psi^{\dagger}(\mathbf{r}, t) \, \mathbb{I} \overleftrightarrow{\partial_y} \Psi(\mathbf{r}, t) - s \Psi^{\dagger}(\mathbf{r}, t) \, \sigma^{y} \overleftrightarrow{\partial_0} \Psi(\mathbf{r}, t) \right], \tag{2.37}$$

where the symmetric convention for the derivatives acting on the electron fields is understood:

$$\phi^{\dagger} \overleftrightarrow{\partial_i} \phi = \frac{1}{2} (\phi^{\dagger} \partial_i \phi - \partial_i \phi^{\dagger} \phi). \tag{2.38}$$

Notice that the last term in Equation (2.37) is proportional to the chirality of the node.

We will use the *Lehmann representation* to compute the response function of the system. Using the Landau wave-functions as the basis of our problem,

$$\Psi^{\dagger}(\mathbf{r}, t) = \sum_{\mathbf{k}m} \varphi^{\dagger}_{\mathbf{k}ms}(\mathbf{r}) a^{\dagger}_{\mathbf{k}ms}(t) \tag{2.39}$$

[3]This form of the energy-momentum tensor for the Dirac Lagrangian is non-trivial, since its definition arises as the result of demanding local Lorentz invariance to the effective action [187].

(the summation runs over the different Landau bands and the allowed values of k_x, k_z), the current and energy-momentum operators are:

$$J^x(\mathbf{r},t) = \sum_{\mathbf{k}m,\mathbf{l}n} j^x_{\mathbf{k}m,\mathbf{l}n}(\mathbf{r})\, a^\dagger_{\mathbf{k}ms}(t) a_{\mathbf{l}ns}(t), \tag{2.40}$$

$$T^{0y}(\mathbf{r},t) = \sum_{\boldsymbol{\kappa}\mu,\boldsymbol{\lambda}\nu} t^{0y}_{\boldsymbol{\kappa}\mu,\boldsymbol{\lambda}\nu}(\mathbf{r})\, a^\dagger_{\boldsymbol{\kappa}\mu s}(t) a_{\boldsymbol{\lambda}\nu s}(t), \tag{2.41}$$

with the matrix elements:

$$j^x_{\mathbf{k}m,\mathbf{l}n}(\mathbf{r}) = s v_{\mathrm{F}} e \varphi^\dagger_{\mathbf{k}ms}(\mathbf{r})\, \sigma^x\, \varphi_{\mathbf{l}ns}(\mathbf{r}), \tag{2.42}$$

$$t^{0y}_{\boldsymbol{\kappa}\mu,\boldsymbol{\lambda}\nu}(\mathbf{r}) = \frac{1}{4}\varphi^\dagger_{\boldsymbol{\kappa}\mu s}(\mathbf{r}) \left[v_{\mathrm{F}} \mathbb{I} \overleftrightarrow{p}_y + s\sigma^y (E_{\kappa_z \mu s} + E_{\lambda_z \nu s} - 2\mu) \right] \varphi_{\boldsymbol{\lambda}\nu s}(\mathbf{r}), \tag{2.43}$$

where $a^\dagger_{\mathbf{k}ms}$ ($a_{\mathbf{k}ms}$) creates (annihilates) an electron with momentum $\mathbf{k}$ at the band m of the Weyl cone s. For future purposes, we have added a finite chemical potential to the last term of the energy-momentum tensor. When a magnetic field is present, the definition of the energy-momentum tensor includes a covariant derivative $D_\mu = \partial_\mu - ieA_\mu$. The time-derivative D_0 is proportional to a scalar potential, which accounts for the chemical potential. We will compute the thermoelectric coefficient defined in Equation (2.24) for each chirality. The chiral sign s remains fixed during the calculation of the response function and no summation is included when expanding the operators into the Landau basis. After working out the various integration terms (details of the calculation are given in appendix B), the thermoelectric function takes the form:

$$\chi^{xy}(\mathbf{q},\omega) = \lim_{\eta\to 0^+} \sum_{\mathbf{k},mn} \frac{(2\pi)^3}{\mathcal{V}} \frac{i v_{\mathrm{F}} \hbar\, s\, j^x_{\mathbf{k}m,\mathbf{k}+\mathbf{q}n}(\mathbf{q}) t^{0y}_{\mathbf{k}+\mathbf{q}n,\mathbf{k}m}(\mathbf{q}) \left[n_{\mathbf{k}ms} - n_{\mathbf{k}+\mathbf{q}ns} \right]}{(E_{k_z ms} - E_{k_z+q_z ns} + i\hbar\eta)(E_{k_z ms} - E_{k_z+q_z ns} + \hbar\omega + i\hbar\eta)} \tag{2.44}$$

where $n_{\mathbf{k}ms} = [\exp(\beta(E_{k_z ms} - \mu)) + 1]^{-1}$ is the Fermi-Dirac distribution and the matrix elements are computed in the reciprocal space. At zero temperature, the distribution function becomes a step function $n_{\mathbf{k}ms} = \Theta(\mu - E_{k_z ms})$, which restricts the possible transitions between energy levels. In order to capture the conformal limit, the chemical potential is placed at the neutrality point ($\mu = 0$), where the main contribution comes from the chiral Landau level.

2.4 Results

2.4.1 Thermoelectric response at zero temperature

As mentioned in section 2.3.2, the linear response of the system has been obtained using the exact eigenstate representation, where the operators are written in the basis that diagonalizes the system. Assuming that the wave-length of the background fields is large in comparison with the characteristics length of the material, we can concentrate on the local limit approximation $\mathbf{q} \to 0$.

We will trade the summation over the allowed k-vectors to an integral [34] over the whole space. Since neither the eigenvalues nor the matrix elements depend on k_x, the corresponding integration accounts for the degeneracy factor $eBL_y/\hbar$ of each Landau level. For the remaining component, we rewrite the different variables as a function of a dimensionless parameter $\kappa_z = \hbar k_z/\sqrt{2eB\hbar}$. The thermoelectric function becomes (see appendix B):

$$\chi^{xy}(0,\omega) = \lim_{\eta\to 0^+} \frac{1}{4(2\pi)^2} \sum_{m,n}{}' \frac{v_F e^2 sB}{\hbar} \int \mathrm{d}\kappa_z \, \xi(m,n,s,\omega)\alpha^2_{\kappa_z ms} \times \left[s(E_{\kappa_z ms} + E_{\kappa_z ns} - 2\mu) - \alpha_{\kappa_z ns}\sqrt{M-1} - \sqrt{M}/\alpha_{\kappa_z ms} \right], \tag{2.45}$$

where the summation is restricted to $N = M - 1$ and the dimensionless function $\xi(m,n,s,\omega)$ is defined as:

$$\xi(m,n,s,\omega) = \frac{2\left[n_{\kappa_z ms} - n_{\kappa_z ns}\right]\left[\alpha^2_{\kappa_z ms}+1\right]^{-1}\left[\alpha^2_{\kappa_z ns}+1\right]^{-1}}{\left(E_{\kappa_z ms} - E_{\kappa_z ns} + i\eta\right)\left(E_{\kappa_z ms} - E_{\kappa_z ns} + \omega/\omega_c + i\eta\right)}. \tag{2.46}$$

$\omega_c = v_F\sqrt{2eB/\hbar}$ is the cyclotron frequency, which gives the separation between energy bands. The integrand appearing in Equation (2.45) is a dimensionless function that results in a numerical value when the integral is performed. The restriction over the possible transitions ensures that the energies appearing in the denominator are different. At zero temperature and chemical potential only interband transitions "across the Fermi sea" are allowed. Considering this limit, the zeroth order result for the thermoelectric coefficient is given by:

$$\chi^{xy} = \lim_{\omega\to 0} \chi^{xy}(0,\omega) = \frac{1}{2(2\pi)^2}\frac{v_F e^2 sB}{\hbar} \tag{2.47}$$

This is a remarkable result. Weyl nodes present a finite, constant thermoelectric coefficient at zero temperature, with $\nabla T/T$ being kept finite. This value depends only on universal constants and the Fermi velocity as the only material-dependent

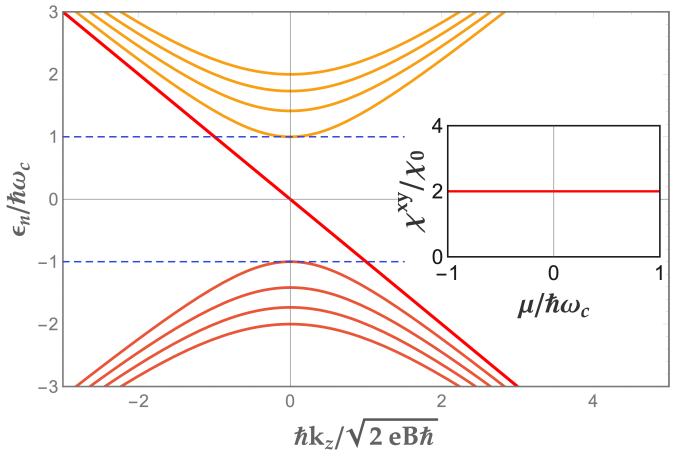

FIGURE 2.3: Landau level structure of a single chirality in the Dirac semimetal. The inset shows the thermoelectric coefficient as a function of the chemical potential at $T = 0$. The function has a constant value ($\chi^{xy}/\chi_0 = 2$, where $\chi_0 = v_F e^2 B/(4\pi)^2\hbar$) when μ lies in the interval between the first Landau levels.

parameter. This result is valid at the Dirac point, at zero chemical potential, where it captures the vacuum contribution from the quantum anomaly. The thermoelectric coefficient stemming from the opposite node has the same value (we have been particularly careful to follow the chirality dependence of the terms throughout the calculation to ensure that no cancellations occur), and both Weyl partners contribute to the response function with the same sign.

2.4.2 Thermoelectric response at finite temperature and chemical potential

The Fermi energy in real materials is close but not exactly at the Dirac point, although the experimental expertise can tune it by chemical doping to great accuracy. To bring the theoretical result closer to the experimental situation, we have extended the calculation to include thermal effects and a non-zero chemical potential.

The expression given in Equation (2.45) is valid for finite μ and T, which enter in the response term through the definition of the Fermi distribution. At zero temperature, the thermoelectric coefficient exhibits a plateau when the chemical potential lies between the first Landau levels $|\mu| < \hbar\omega_c$ (see Figure 2.3). This behaviour is expected, as the zeroth Landau level has a constant density of states. The zeroth

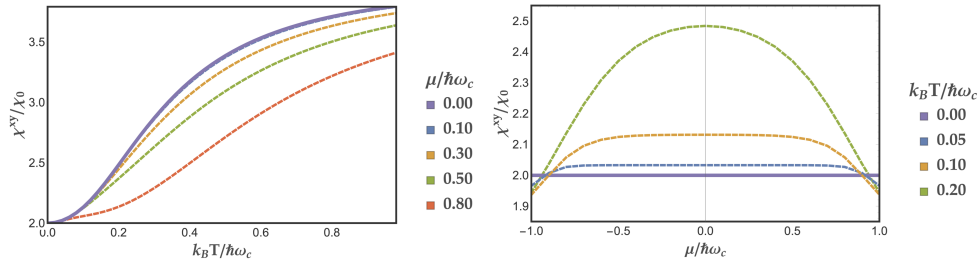

FIGURE 2.4: Zeroth order thermoelectric coefficient at finite temperature and chemical potential. *(Left)*: Behaviour of the thermoelectric coefficient as a function of the temperature for different values of μ. *(Right)*: Behaviour of the thermoelectric coefficient as a function of the chemical potential for different values of the temperature. Thermally excited carriers enhance the response function.

order coefficient gets correction arising from higher-energy transitions. The contribution to the numerical value coming from these transitions decreases rapidly with the Landau level index. Nevertheless, the addition of these contributions does not modify the general behaviour of the system, and the thermoelectric function still presents a plateau when the higher-energy corrections are included.

The generalization to finite temperature is represented in Figure 2.4. By increasing the temperature, thermally activated carriers contribute to higher values of the transport coefficient, which resembles the general thermoelectric behaviour of other materials [138, 154]. As Figure 2.4 shows, the size of the plateau is reduced according to the structure of the Fermi functions.

2.5 Conclusions and discussion

In this chapter, we have studied the thermoelectric coefficient of a Dirac and Weyl semimetal in a magnetic field. Motivated by the recent discovery of an anomaly-related current [91, 93], we have performed a Kubo calculation of the electric current generated by a thermal gradient, focusing on the conformal limit $\mu = 0$. As predicted by the anomaly result, we obtained a non-vanishing thermoelectric coefficient at zero temperature. The quantity $\chi^{xy}/v_F B$ has a quantized value determined by universal constants. This value remains fixed at zero temperature and when the chemical potential lies in the interval $|\mu| < \hbar\omega_c$.In this regime, other possible sources for the thermoelectric current are strongly suppressed, and the result can be seen as an evidence for the scale anomaly described in Ref. [91]. The calculation has

been extended to include finite chemical potential and temperature effects. The resulting thermoelectric coefficient presents, as a function of the chemical potential, a distinctive experimental signature in the form of a plateau when only the lowest Landau level is populated.

The analysis has been done considering the low-energy model of a Dirac semimetal, concentrating on a single chirality. The contribution from the other node has the same sign, both chiralities adding up to the total response function. When the Weyl nodes are separated in momentum space, additional contributions proportional to the separation will contribute to the electric response. Dirac semimetals, where the two chiralities are superimposed in momentum space, are better "testing samples" to investigate this anomaly-related current, since additional effects arising from the Berry curvature or the separation between nodes are minimized.

The results shown in this chapter are based on the zeroth order result for the thermoelectric coefficient. Higher-order transitions will contribute to the numerical value of the response function, but the general behaviour will remain unaltered.

Chapter 3

Thermoelectric relations in the conformal limit

3.1 Introduction

In addition to the industrial impact and novel applications in the technological field, understanding the physical properties of transport coefficients is a topic of major interest as they provide a tool to characterize and distinguish the electronic and thermal attributes of materials [180]. As was manifested in chapter 2, the unusual thermoelectric result presented in section 2.4 proves that Dirac and Weyl semimetals do not behave as ordinary semiconductors. Different transport coefficients are related by phenomenological relations. These connections are used as instruments to study the properties of the materials, as their violation signals departure from the standard behaviour.

As will be illustrated in section 3.2, examples of such relations are the *Wiedemann-Franz law* and the *Mott relation*. The former establishes that the ratio between the thermal and the electrical conductivity is proportional to the temperature of the system, which the proportionality factor having a universal value $\mathcal{L}$ called Lorenz number. The Mott relation, on the other hand, connects the thermopower with the derivative of the electrical conductivity with respect to the chemical potential (evaluated at the Fermi level).

The first attempt to understand the underlying physics behind the Wiedemann-Franz relation can be traced down to the studies by Paul Drude in the early days of electrical conduction theory in metals. His model was able to give a crude estimate of the proportionality factor, the numerical value being in a good agreement with the experimental result [34]. More precise models were developed later in order to

explain the flow of electric and thermal currents and the transport coefficients. In particular, the kinetic theory [138, 34, 32] has proved very successful in analyzing the transport properties of standard metals. The key element behind this theory is the Boltzmann function $f_{\mathbf{k}}$, which characterizes the movement and evolution of a particle distribution (either classically or *semi*-classically if quantum corrections are taken into account). Once this function has been evaluated, any physical observable is given by the expectation value of the corresponding operator. In particular, the analytical expression for the transport coefficients and the phenomenological relations can be obtained by expanding the distribution function in a power series in temperature. More rigorous approaches were adopted in order to derive the mentioned relations in Refs. [188, 189]. In these works, the exact expressions for the transport coefficients were computed using the Kubo and Green's function formalism, leading to the Wiedemann-Franz and Mott relations after a Sommerfeld expansion.

The validity of these relations was questioned with the emergence of quantizing magnetic fields. It was shown that the expressions for the thermal transport coefficients in terms of correlation functions are invalid under strong magnetic fields [190, 191]. The numerous attempts suggested to prove the validity of the relations in that regime culminated with the work of Smrčka and Středa [192]. Based on the Luttinger theory of thermal transport [184], they generalized the Kubo formulas and included magnetization currents to determine the limits of validity of the relations[1], laying the foundations of our current understanding of the phenomena [185].

The above thermoelectric relations are based on the Landau-Fermi liquid paradigm [193, 2, 36], where the electronic interactions can be neglected and the predominant events are due to scattering of electrons with phonons. In this theory, the electrons are described as a free-motion system, which is completely characterized by the kinetic theory. The Fermi liquid framework fails when trying to describe strongly interacting systems, or when the electron-electron interactions become the fastest time scale in the problem. The dynamics in such scenario can be characterized in terms of a hydrodynamic description of the quasiparticles [194, 195]. Such situation normally arises in ultra-clean samples [196] or in systems with a vanishing Fermi surface such as graphene [197], where long-range interactions are enhanced due to ineffective Coulomb screening. The transport coefficients are severely modified by hydrodynamic effects. Deviations from these relations can also be observed at high temperatures, originated by inelastic phonon scattering [182, 197, 198].

The emergence of topological and novel Dirac materials has raised a renewed attention in the field. These materials display anomalous Hall conductivities originated by non-vanishing Berry curvatures, similarly to the case of ferromagnetic materials (see Refs. [56, 199–202, 95] and references therein for a overview of the

[1] As shown in their paper, Středa and Smrčka verified that these relations remain valid as long as the scattering events are elastic and the limit $\hbar\omega \gg k_B T$ is satisfied.

topic). The validity of Mott relation and Wiedemann-Franz law is still an open question in these materials, and the thermoelectric properties of Dirac and Weyl semimetals is a very active field of current research [148, 123, 150, 153]; while topological effects have been successfully included in the semiclassic framework [203] and experimental observations in ferromagnetic films revealed the validity of the Mott relation [146, 204, 205], the theoretical and experimental situation in topological materials is less clear [146, 206–209].

The interesting result depicted in section 2.4 raises more questions to this situation. It shows that Dirac materials exhibit a finite thermoelectric response even at the zero temperature limit incompatible with the Mott relation. In this chapter we will analyze the thermoelectric relations and the role played by the finite thermoelectric coefficient obtained in chapter 2. First, we will review how the phenomenological Wiedemann-Franz law and Mott relation arise from the thermoelectric coefficients by using the kinetic description. This will include a revision of the different mechanism that would lead to a breakdown of the Fermi liquid description of coherent quasiparticles. Next, we will compute the quantities involved in the Mott relation, the electrical conductivity and the thermoelectric tensor, using a Kubo formula. We finally discuss the results obtained and their relation with the standard Mott relation[2].

3.2 Phenomenological transport relations

As mentioned in chapter 2, external electromagnetic and thermal perturbations induce charge and heat currents, and the transport coefficients are defined in linear response after a power expansion in terms of the interactions. Kinetic theory yields an analytic expression for these coefficients as a function of the Boltzmann distribution function $f_{\mathbf{k}}(\mathbf{r})$ and the collision integral. This mechanical approach studies the number of carriers entering and leaving a particular region in the space with a certain velocity $\mathbf{v}$. Kinetic theory was originally derived for a classical gas of hard spheres, and it is well suited to describe classical systems and wave-packets, where every particle has a well-defined position and momentum and the total state of the system can be defined by the number of particles in each one of these individual states [210, 138].

[2]This chapter is based on "Vicente Arjona, Juan Borge and María A.H. Vozmediano, *Thermoelectric relations in the conformal limit in Dirac and Weyl semimetals*, arXiv preprint, arXiv:1903.00019 (2019)".

Once the distribution function $f_{\mathbf{k}}$ is known, the electric and heat flows are determined by:

$$\mathbf{J} = \int \mathrm{d}\mathbf{k}\, q\mathbf{v}_{\mathbf{k}} f_{\mathbf{k}} \tag{3.1}$$

$$\mathbf{J}_Q = \int \mathrm{d}\mathbf{k}\, (E_{\mathbf{k}} - \mu)\mathbf{v}_{\mathbf{k}} f_{\mathbf{k}}. \tag{3.2}$$

The Boltzmann distribution includes all possible mechanisms (diffusion, external forces, scattering, etc.) that contribute to the displacement of the particles. Using the solution of the Boltzmann equation in the presence of electric fields and thermal gradients, it can be shown generically that the transport coefficients $L^{ij}_{\alpha\beta}$[3] are written as a function of a general integral term [138, 32, 34]:

$$\begin{aligned} L_{EE} &= \mathcal{K}_0 \\ L_{ET} &= -\frac{1}{T} L_{TE} = -\frac{1}{qT}\mathcal{K}_1 \\ L_{TT} &= -\frac{1}{q^2 T}\mathcal{K}_2, \end{aligned} \tag{3.3}$$

where the integral function is defined as:

$$\mathcal{K}_n^{ij} = -q^2 \int \mathrm{d}\mathbf{k}\, v_{\mathbf{k}}^i v_{\mathbf{k}}^j \tau(\mathbf{k})(E_{\mathbf{k}} - \mu)^n \frac{\partial f_{\mathbf{k}}^0}{\partial E_{\mathbf{k}}}. \tag{3.4}$$

In the above equation, $\tau(\mathbf{k})$ is the scattering relaxation time and $f_{\mathbf{k}}^0$ is the Fermi distribution function at equilibrium. The function defined in Equation (3.4) depends linearly on the derivative of the equilibrium Fermi distribution, which selects the energy region at the Fermi surface and its vicinity. After applying a Sommerfeld expansion, Equation (3.4) is reduced to:

$$\mathcal{K}_n = \left[(E_{\mathbf{k}} - \mu)^n L_{EE} + \frac{\pi^2}{6} k_B^2 T^2 \frac{\partial^2}{\partial E_{\mathbf{k}}^2} \left((E_{\mathbf{k}} - \mu)^n L_{EE} \right) + \cdots \right]_{E_{\mathbf{k}} = \mu}, \tag{3.5}$$

where the function $\mathcal{K}_n$ is evaluated at the Fermi level. This allows to establish thermoelectric relations between the various coefficients. Starting with the thermal component L_{TT}, the first non-vanishing contribution is given by the second order

[3] In order to simplify the notation, we have omitted the tensor indices in those situations where the dependence is clearly understood.

term:

$$L_{TT} = \frac{\pi^2}{3}\frac{k_B^2 T}{q^2} L_{EE}. \tag{3.6}$$

Equation (3.6) is the Wiedemann-Franz law, where the proportionality constant is the Lorenz number

$$\mathcal{L} = \frac{\pi^2}{3}\frac{k_B^2 T}{q^2}, \tag{3.7}$$

which is independent of temperature, material details or scattering processes. This relation is based on the fact that heat and charge currents are carried by the same type of carriers; when the dominant relaxation processes are lattice imperfections, the relaxation times of thermal and charge currents are very similar, which indicates that both currents are affected in the same way by the scattering mechanism. Proceeding in an analogous way with the thermoelectric tensor L_{ET}, the highest contribution in the power series is proportional to the derivative of the electric coefficient, giving rise to the Mott relation:

$$L_{ET} = -\frac{\pi^2}{3}\frac{k_B^2 T}{q}\left[\frac{\partial L_{EE}}{\partial E_{\mathbf{k}}}\right]_{E_{\mathbf{k}}=\mu}. \tag{3.8}$$

Unlike the previous Wiedemann-Franz relation, the expression depends on the charge sign of the carriers. The derivative is computed at the chemical potential and, consequently, it is affected by the fluctuations of the conductivity at the Fermi surface. Considering a normal metal, these changes are mainly produced by variations of the electronic mean free path and the scattering probability.

The transport coefficients defined in Equation (3.3) cannot be directly measured in real systems, and the Mott relation and the Wiedemann-Franz law are regularly related to the conductivities observed experimentally; the electrical conductivity σ, the thermal conductivity κ and the thermopower Q[4]. One can expand the conductivities in a power series in temperature [138], as was previously done for the transport coefficients. As a result, the phenomenological relations remain unaltered, but now they are written as a function of the new terms:

$$\frac{\kappa}{T\sigma} = \mathcal{L} \tag{3.9}$$

$$\frac{Q}{qT} = \mathcal{L}\left[\frac{\partial \ln \sigma}{\partial E_{\mathbf{k}}}\right]_{E_{\mathbf{k}}=\mu}. \tag{3.10}$$

[4]As discussed in chapter 1, the thermopower is also known as Seebeck coefficient, the strength of the induced voltage in response to the temperature gradient. Seebeck coefficient is a key ingredient in the classification of the thermoelectric materials according to their effectiveness, which is evaluated by its figure of merit. The inverse process defines the Peltier coefficient, the magnitude of the thermal current generated by the charge flow.

The Wiedemann-Franz and the Mott relations were derived without any particular assumption or approximation, and remain valid in a wide variety of scenarios. They are employed to determine electrical and thermal conductivities that might otherwise be challenging to measure [144, 211, 212]. Physical systems will obey Equations (3.9) and (3.10) as long as the electron scattering is elastic, a condition normally fulfilled in scattering processes originated by lattice imperfections (this condition can be broken at high temperatures due to inelastic phonon scattering). It is the role played by the interactions inside the material which determines the range of effectiveness of Wiedemann-Franz law and Mott relation.

The Landau-Fermi liquid model fails when describing strongly interacting systems or anomalous Fermi surfaces. When the Coulomb interactions are the dominant relaxation process, the free-electron model is not valid, and the system may become dominated by hydrodynamic effects [195, 213]. In this regime, the system is characterized by conserved variables and their respective continuity equations, in a state that is close to the thermodynamic equilibrium. The electronic motion is described as a collective behaviour and restricted to channels [214], which is used as a signature of the hydrodynamic nature of transport. The hydrodynamic framework has been successfully used to describe numerous interacting systems [215–218]. Under strong electron-electron interactions, the relaxation times follow different mechanisms, affecting the conductivities in opposite ways [219, 220]. Evidences on the breakdown of these relations (all being connected to non-Fermi liquid phenomena) have been observed in different works [221–223].

The emergence of Dirac matter in condensed matter has entailed a new milestone in thermoelectricity; the non-trivial topological features of these materials open new avenues to bypass the limitations of conventional thermoelectrics and generate large figures of merit [155, 156], specially when quantizing magnetic fields are present: Dirac materials do not present localizing effects due to their topological protection, and their low carrier density and very high mobility made them ideal platforms to test the electronic behaviour in the extreme quantum regime. A vivid debate has raised in the literature around the validity of the thermoelectric relations [197, 150, 206, 207, 209, 211, 182]. Having a linear dispersion relation, the discussion can be divided into two well-defined cases: when the chemical potential is at the charge neutrality point, where the Fermi surface is a point, and when the system is doped. In the undoped case, hydrodynamic effects are fostered due to the ineffective Coulomb screening [224] and the vanishing density of states at the Fermi level. Away from the degeneracy point, Dirac systems have a robust Fermi surface and are described by the ordinary Fermi liquid theory.

Different studies have reported evidences of hydrodynamic effects in the electronic motion of graphene [225–228] and the emergence of a Dirac fluid (formation of strongly-interacting quasirelativistic plasma) at the neutrality point [197]. In this

regime, both Wiedemann-Franz and Mott relations are strongly violated. The experimental situation of Dirac and Weyl semimetals is still in an early stage, but the path is very reminiscent of the graphene case. There are already different theoretical works exposing the failure of the transport relations and addressing the properties of the materials within the hydrodynamic approach [182, 229–231], the breakdown of the Wiedemann-Franz relation and the emergence of the hydrodynamic regime have been recently observed experimentally in the Weyl semimental WP_2 [207]. Non-trivial topological features add a new layer to this field, with the development of anomalous responses [123, 148, 232, 212]. Numerous efforts have been devoted to the characterization of thermal topological responses, especially concerning the Nernst currents originated from non-trivial Berry curvatures, which has been shown to exceed conventional thermopower of traditional materials [123, 152].

3.3 Electrical conductivity of Dirac matter

The finite thermoelectric coefficient at zero temperature and chemical potential described in Equation (2.47) generates a puzzling question concerning the thermoelectric relations. In this section we will analyze the Mott relation for the case of Dirac and Weyl semimetals. The zeroth order result for the off-diagonal thermoelectric coefficient was:

$$\chi^{xy} = \frac{1}{2(2\pi)^2}\frac{e^2 v_{\mathrm{F}} B}{\hbar}. \tag{3.11}$$

The coefficient described in Equation (3.11) was computed in the presence of perpendicular magnetic field and temperature gradient. The numerical value was obtained by considering the energy transitions between the lowest Landau levels. As highlighted in chapter 2, the coefficient χ^{xy} has a finite contribution in the conformal limit (zero temperature and zero chemical potential). This unusual behaviour automatically implies the violation of the Mott relation in Equations (3.8) and (3.10). In order to analyze the validity of the thermoelectric relation in the conformal limit of Dirac electrons, we calculate the Hall conductivity with a Kubo formula as the one done in section 2.3. Before proceeding with the calculation, we will review the basic concepts of the electrical conductivity and its derivation.

3.3.1 Electrical conductivity. Theoretical background

In linear response theory, the conductivity tensor σ^{ij} is the proportionality function that relates the induced electric density with the applied electric field. Mathematically, σ is defined after coupling the Hamiltonian to an electromagnetic field, introduced by the minimal substitution of the momentum operator $\mathbf{p}$ to $\mathbf{p} + e\mathbf{A}$. As mentioned in chapter 2, the particle current operator is defined by considering

infinitesimal variations of the Hamiltonian with respect the vector field **A**:

$$\delta H = \int \mathrm{d}\mathbf{r}\, \mathbf{J}\delta\mathbf{A}. \tag{3.12}$$

For non-relativistic Hamiltonians, which are proportional to the square of the momentum operator, the current vector is given by the sum of two terms; the diamagnetic contribution, proportional to **A**, and the paramangetic term, independent of the gauge vector. These terms arise after expanding the electromagnetic Hamiltonian in powers of **A** and calculate the functional derivative of the series with respect the vector field. Hence, the linearly dependent contribution leads to the paramagnetic term while the $O[A^2]$ order contribution gives rise to the diagmagnetic term [49].

For generic quantum systems with a parabolic dispersion relation (a non-relativistic free-electron gas, for instance), the diamagnetic contribution is the product of the equilibrium particle density $\langle\rho(\mathbf{r})\rangle$ and the gauge field **A**. The paramagnetic term is proportional to the current-current correlation function [233, 49]:

$$\Pi^{ij}(\mathbf{r}, t; \mathbf{r}', t') = -\frac{i}{\hbar}\int_{-\infty}^{\infty} \mathrm{d}\mathbf{r}'\mathrm{d}t' \left\langle [J^i(\mathbf{r}, t), J^j(\mathbf{r}', t')] \right\rangle. \tag{3.13}$$

Selecting a suitable gauge where $\mathbf{A}(\mathbf{r}, \omega) = \mathbf{E}(\mathbf{r}, \omega)/i\omega$, the current operator is written as a function of the external field, and the expectation value of the current operator reads:

$$\begin{aligned}\left\langle J^i(\mathbf{q}, \omega)\right\rangle &= \left\langle J^i_{\text{diam}}\right\rangle + \left\langle J^i_{\text{param}}\right\rangle \\ &= \left[\frac{-i}{\omega}\Pi^{ij}(\mathbf{q}, \omega) + \frac{e^2\langle\rho\rangle}{im\omega}\delta^{ij}\right] E_j(\mathbf{q}, \omega),\end{aligned} \tag{3.14}$$

where the time and space translational invariance of the system are used to write the expression in momentum space. The conductivity tensor is defined as the function inside the brackets:

$$\sigma^{ij}(\mathbf{q}, \omega) = \frac{-i}{\omega}\Pi^{ij}(\mathbf{q}, \omega) + \frac{e^2\langle\rho\rangle}{im\omega}\delta^{ij} \tag{3.15}$$

Equation (3.15) represents a powerful result that includes all possible (linear) electromagnetic phenomena. The diagonal terms describe the longitudinal conductivity, and the off-diagonal components contain the Hall conductivity. In the particular case of Dirac materials, whose low-energy excitations have a linear dispersion relation, the diamagnetic contribution to the conductivity tensor vanishes, as this term is derived from the second derivative of the Hamiltonian. The response to an external electric field reduces to the computation of the correlation function

$\Pi(\mathbf{q}, \omega)$. We review the Mott relation for the electronic excitations around a single Weyl node, without considering the possible effects arising from the separation between nodes (see Refs. [234, 147] for good reviews about the topic).

3.3.2 Hall conductivity for Dirac matter

As was already mentioned, the diamagnetic contribution is removed from the expression of the conductivity in the case of Dirac materials, and one is left with the term:

$$\sigma^{ij}(\mathbf{q}, \omega) = (2\pi)^3 \int_{-\infty}^{\infty} \mathrm{d}t \, e^{i\omega(t-t')} \frac{-1}{\mathcal{V}\hbar\omega} \left\langle [J^i(\mathbf{q}, t), J^j(-\mathbf{q}, t')] \right\rangle . \tag{3.16}$$

The unperturbed low-energy Hamiltonian describing the electronic excitations around a single Weyl cone takes the form:

$$H_s = s v_{\mathrm{F}} \sigma^i (p_i - q A_i) \tag{3.17}$$

where $s = \pm 1$ defines the chirality of the node and $q = -e$ is the electronic charge. As was done in chapter 2, we choose the Landau gauge $A_x = -By$ and the y-axis along the direction of the external perturbation. The set of eigenvectors and eigenvalues are given in Equations (2.28) and (2.29), respectively. Since we are working with non-interacting electrons, the response function can be written in terms of single-particle operators [176]; following the arguments explained in appendix B, we can write the conductivity function using the exact eigenstates representation. The resulting expression takes the characteristic form:

$$\sigma^{ij}(\mathbf{q}, \omega) = \frac{-i(2\pi)^3}{\mathcal{V}\omega} \sum_{\mathbf{k}, mn} j^i_{\mathbf{k}m, \mathbf{k}+\mathbf{q}n} j^j_{\mathbf{k}+\mathbf{q}n, \mathbf{k}m} \frac{(n_{\mathbf{k}m} - n_{\mathbf{k}+\mathbf{q}n})}{E_{\mathbf{k}m} - E_{\mathbf{k}+\mathbf{q}n} + \hbar\omega + i\hbar\eta}, \tag{3.18}$$

where the matrix element $j^\alpha_{\mathbf{k}m, \mathbf{k}+\mathbf{q}n}$ reads

$$j^\alpha_{\mathbf{k}m, \mathbf{k}+\mathbf{q}n} = \frac{1}{(2\pi)^3} \int_{-\infty}^{\infty} \mathrm{d}\mathbf{r} \, e^{-i\mathbf{q}\mathbf{r}} s v_{\mathrm{F}} \varphi^\dagger_{\mathbf{k}m}(\mathbf{r}) \sigma^\alpha \varphi_{\mathbf{k}+\mathbf{q}n}(\mathbf{r}), \tag{3.19}$$

and the wave-functions $\varphi_{\mathbf{k}m}(\mathbf{r})$ are given in Equation (2.29). The matrix elements of Equation (3.18) are computed between single particle states, and the denominator involves the difference between single particle energies.

3.3.3 Hall conductivity. Local and zero frequency limit

The conductivity tensor is a function of both ω and $\mathbf{q}$. Assuming that the wavelength of the external field is large in comparison to the characteristic length of the sample, we can focus on the local limit approximation and set $\mathbf{q} \to 0$. In the local approximation, non-vanishing results are obtained when the optical transitions between energy levels satisfy the condition $M = N \pm 1$. After computing the different matrix elements, the Hall conductivity for a Weyl semimetal at the local and zero frequency limit is given by the expression:

$$\sigma^{xy} = \lim_{\eta \to 0^+} \sum_{m,n}{}' \frac{\sqrt{2}}{4\pi l_B} \frac{e^2}{h} \int \mathrm{d}\kappa_z \, \frac{-2\alpha^2_{\kappa_z ms}}{(\alpha^2_{\kappa_z ms}+1)(\alpha^2_{\kappa_z ns}+1)} \frac{n_{\kappa_z ms} - n_{\kappa_z ns}}{(\epsilon_{\kappa_z ms} - \epsilon_{\kappa_z ns} + i\hbar\eta)^2}, \tag{3.20}$$

where h is the Planck's constant and the factor $[\alpha^2_{k_z ms}+1]^{1/2}$ comes from the wavefunction normalization of the Landau eigenvectors, defined as:

$$\alpha^2_{k_z ms} = \frac{-\sqrt{2eB\hbar M}}{E_{k_z ms}/sv_\mathrm{F} - \hbar k_z}. \tag{3.21}$$

In deriving Equation (3.20), we have introduced the dimensionless variables $k_z = \kappa_z \sqrt{2} l_B^{-1}$ and $E_{k_z ms} = \hbar\omega_c \epsilon_{\kappa_z ms}$. The Hall conductivity is written in terms of the constant

$$\sigma_0 = \frac{\sqrt{2}}{4\pi l_B} \frac{e^2}{h}, \tag{3.22}$$

which is characterized by universal constants and the magnetic length l_B. Throughout this chapter, we will use σ_0 as the natural units for the results relative to the Hall conductivity. The conductivity tensor includes an infinite sum over energy levels restricted to the condition $N = M - 1$ where, as will be shown, the higher energetic transitions do not contribute to the response function. Figure 3.1(a) displays the Hall conductivity σ^{xy} as a function of the chemical potential at $T = 0$. We concentrate at the quantum limit, where the zeroth Landau level is the only filled band. The completely filled lowest Landau level produces a finite, linearly dependent conductivity [234] when the chemical potential is placed at the interval $\mu \leq |\hbar\omega_c|$. Higher interband transitions across the chemical potential adds up exactly to zero [235], the lowest Landau level being the only contribution to the conductivity, as depicted in Figure 3.1(b) . This exact cancellation among optical transitions for energies larger than $\hbar\omega_c$ remains valid as long as the temperature of the system is zero. As illustrated in Figure 3.1(a), the effect of the temperature is to increase the slope of the function, since thermally activated carriers participate in the response function with a finite contribution, leading to a larger value of the conductivity. It is noteworthy that the conductivity function increases considerably when the chemical potential

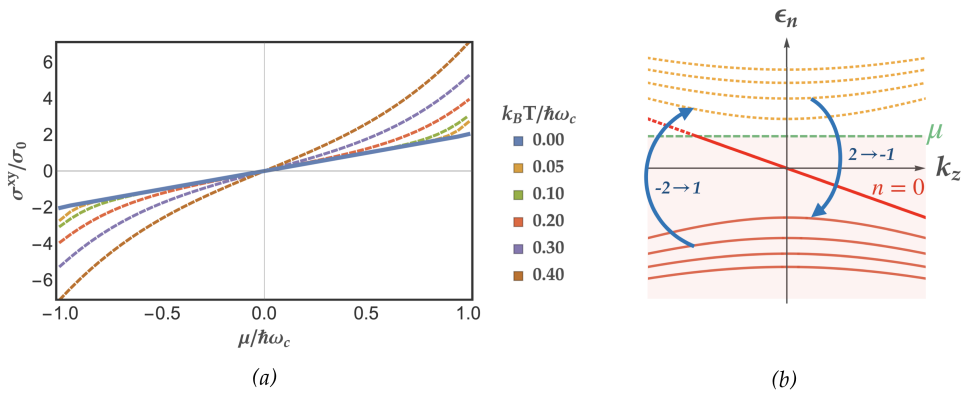

FIGURE 3.1: *(a)*: Hall conductivity σ^{xy} as a function of the chemical potential in the range $-\hbar\omega_c \leq \mu \leq \hbar\omega_c$ for various values of temperature. *(b)*: Schematic representation of the Landau levels and the energy transitions. The contribution of the interband transitions across the Fermi level cancel. Only transitions between the lowest Landau level and excited levels contribute to the conductivity.

approaches the next Landau levels, as the energy threshold becomes significantly smaller.

3.3.4 Energy derivative of the conductivity

The derivative of the conductivity $\partial_\mu \sigma^{xy}$ is easily computed from Equation (3.18): the electrical conductivity depends only on the temperature and the chemical potential through the Fermi distribution $n_{\mathbf{k}ms}$, giving as a result:

$$\frac{\partial}{\partial\mu}\sigma^{xy}\bigg|_{\mu=E_F} = \lim_{\eta\to 0^+} {\sum_{m,n}}' \frac{1}{v_F 8\pi^2}\frac{e^2}{\hbar^2}\int \mathrm{d}\kappa_z \frac{-2\alpha^2_{\kappa_z ms}}{(\alpha^2_{\kappa_z ms}+1)(\alpha^2_{\kappa_z ns}+1)} \times \frac{n_{\kappa_z ms}(1-n_{\kappa_z ms}) - n_{\kappa_z ns}(1-n_{\kappa_z ns})}{\tilde{T}(\epsilon_{\kappa_z ms} - \epsilon_{\kappa_z ns} + i\hbar\eta)^2}\bigg|_{\mu=E_F}, \tag{3.23}$$

where we have defined the dimensionless temperature $\tilde{T} = k_B T/\hbar\omega_c$ and the summation over energy levels is subjected to the restriction $M = N-1$. Similarly to what happened in the previous case, as the temperature increases more thermally activated carriers contribute to the response of the system (more inter-band transitions

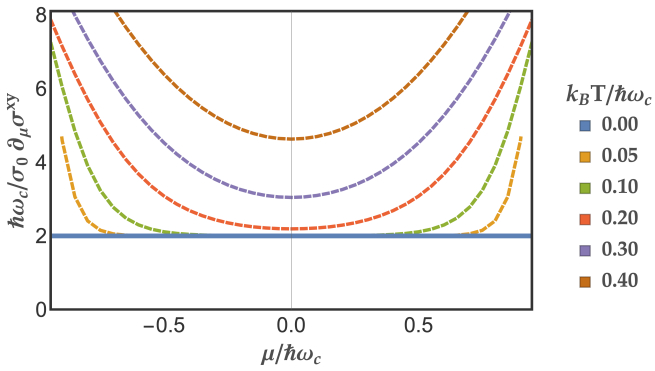

FIGURE 3.2: Temperature dependence of $\partial_\mu \sigma^{xy}$ as a function of the chemical potential. As the temperature increases, more thermally activated carriers contribute to the function.

through the Fermi level are involved). In the low-temperature limit, only the lowest Landau level contributes to the derivative.

The behaviour of $\partial_\mu \sigma^{xy}$ at the Fermi surface $\mu = 0$ as a function of $\tilde{T}$ is depicted in Figure 3.2. Two distinct regimes can be appreciated. At low temperatures, the derivative of the conductivity presents an almost constant value due to the low number of carriers participating in the process. A dramatic enhancement of the function is observed at higher temperatures, especially when the chemical potential approaches the next quantized energy levels.

3.4 Mott relation in Dirac semimetals at the conformal limit

The standard Mott relation between the thermoelectric coefficient L_{ET} and the derivative of the electrical conductivity reads[5]:

$$\chi^{xy} \left(\frac{\partial \sigma^{xy}}{\partial \mu} \right)^{-1}_{\mu = E_F} = \mathcal{R}\, T^2. \tag{3.24}$$

where $\mathcal{R}$ is the proportionality function that has the value $\mathcal{L}$ when the system behaves as a Fermi-liquid. The ratio between these two coefficients for the case of a Dirac semimetals is shown in Figure 3.3. The resulting expression has been derived

[5]The extra T factor appearing in Equation (3.24) originates from the definition of the thermoelectric coefficient L_{ET} in terms of the Kubo response function χ^{xy}; $L^{xy}_{ET} = \chi^{xy}/T$.

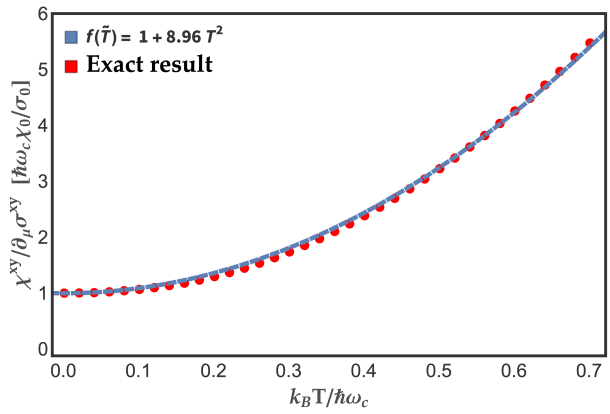

FIGURE 3.3: Temperature dependence of the Mott ration between the thermoelectric response function χ^{xy} and the derivative of the electric conductivity $\partial_\mu\sigma^{xy}$ at $\mu = 0$. Red dots represent the numerical calculation while the blue line is the fit to the function $f(\tilde{T}) = 1 + 8.96\tilde{T}^2$.

considering only the zeroth order values for the electric and thermoelectric coefficients. The dominant contribution to the numerical value of the response functions comes from the energy transitions between the lowest Landau levels. Higher-energy transitions due to temperature effects represent second order corrections to the result displayed in Figure 3.3.

As expected, the thermodynamic relation is violated at the critical point $\mu = 0$: whereas the electric conductivity is a well-behaved function at the conformal point, the anomalous thermoelectric response presents a finite value stemming from the quantum anomaly. Away from the singular point $T = 0$, the relation follows a quadratic dependence in agreement with Equation (3.24): the description of the electronic excitations as coherent quasiparticles returns to be valid. A fit of the numerical values (continuum blue line in Figure 3.3) gives the expression

$$f(\tilde{T}) = 1 + 8.96\tilde{T}^2. \tag{3.25}$$

Restoring the units and ignoring the anomalous contribution from $T = 0$, we get the coefficient

$$\mathcal{R} = 2.24(k_B T)^2/e, \tag{3.26}$$

which coincides with the standard Lorenz value $\mathcal{L}$ to a great accuracy. Therefore, the Mott relation is recovered for temperatures away from the conformal limit.

3.5 Conclusions and discussion

In this chapter we have addressed and analyzed the phenomenological Mott relation in topological Dirac semimetals. We have characterized the electric conductivity in the quantum Hall regime. The resulting term matches the analytical behaviour given in Ref. [234] in the limit of small μ. In the light of the result given in the previous chapter, we have found that the Mott relation breaks down at the conformal limit due to the non-vanishing thermoelectric value obtained at $\mu = T = 0$. This result confirms that the charge neutrality point of clean Dirac samples, similar to the case of two-dimensional graphene, is a singular point that cannot be reached as a continuous limit from a finite chemical potential system. The breakdown of the Mott relation clearly signals, in agreement with previous results [144, 148, 150, 153, 197, 236, 207], the departure of these systems from the Landau-Fermi liquid paradigm of coherent quasiparticles, description that becomes insufficient at this regime. This is a natural result given the vanishing Fermi surface and the poor screening of interactions around neutrality.

Away from the singular point, the system recovers the conventional Fermi liquid phenomenology. The anomalous contribution originated at the charge neutrality point only leads to a solid shift from the expected behavior of a quasiparticle. Additionally, the result exposed in this chapter is not limited to Dirac semimetals, but it is also applicable to Weyl semimetals where, besides this result, extra contributions will arise from the separation between the chiral nodes.

To conclude, there are interesting open problems regarding the phenomenological transport relations and how these are affected by anomalies, which acquire especial relevance in thermoelectric transport measurements performed on Dirac crystals. After different works reported the violation of the Wiedemann-Franz law (either theoretically or experimentally) on Dirac and Weyl semimetals [206, 143, 197, 237, 207, 209], it results particularly relevant to unveil the role of the conformal anomaly on the thermoelectric transport at the critical point of these materials.

Chapter 4

Rotational strain in Weyl semimetals

4.1 Introduction

Experimental realizations of condensed matter systems are neither ideal nor immune to defects, and they present what is generally referred as disorder: crystalline samples usually exhibit irregularities in the lattice, structural defects, magnetic impurities, dislocations, etc. Disorder has profound implications in the mechanical properties of the materials, and its understanding is also crucial to explain the electronic structure and transport features of the sample.

A closely related problem to disorder in condensed matter systems is the presence of strain. The spectral and transport properties of different systems may be affected by external influences such as mechanical deformations, as is illustrated in Figure 4.1. When regarded as small, these perturbations induce smooth oscillations around the equilibrium position of the atoms[1]: elastic deformations modify the distance and relative orientation between the atomic orbitals, leading to local changes in the hopping strength. In the case of Dirac materials, understanding the consequences of elastic perturbations becomes crucial from the electronic point of view, since the transport properties and the electronic structure may be modified under variations of the lattice configuration. Historically, the influence of lattice deformations on the electronic transport properties of Dirac materials has been studied using tight-binding models within the framework of elasticity theory, giving rise to axial vector fields coupled to the electronic degrees of freedom [158, 240, 241]. An

[1]The parameters characterizing the strength of the deformations contribute to the electron-phonon coupling.

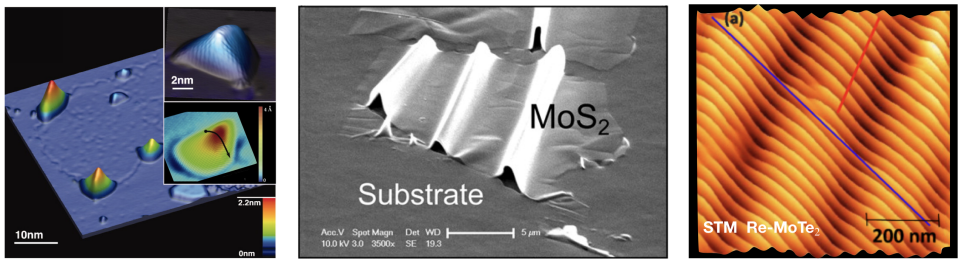

(a) *(b)* *(c)*

FIGURE 4.1: Elastic deformations in Dirac matter. *(a)*: STM experimental images of graphene samples grown on thin films of platinum. The image reveals the formation of highly strained nanobubbles. Adapted from Ref. [163]. *(b)*: Localized uniaxial strain in wrinkled MoS_2 nanolayers. Adapted from Ref. [238]. *(c)*: STM image on the surface of the doped Type-II Weyl semimetal Re-$MoTe_2$. Internal deformations are induced under modulations on the chemical potential, leading to the formation of topographic ripples. Adapted from Ref. [239].

alternative method to study the possible electron-phonon couplings arising in these materials is based purely on symmetry considerations. The possibility of constructing effective interactions using symmetry arguments has been extensively adopted in both quantum field theory and condensed matter systems, where the underlying crystal symmetries constrain the possible actions describing the dynamics of phonons and electrons (for instance, this approach was employed in Ref. [242] for generating all possible interacting terms in graphene layers).

The current chapter is devoted to study the effective low-energy electron-phonon interaction terms stemming from the symmetries of our system. In particular, we will analyze the new terms induced by antisymmetric components of the deformation tensor (related to changes in the orientation of the orbitals) in Dirac and Weyl semimetals.

The effective couplings and their physical interpretation will be discussed in section 4.2. An interesting aspect of the 3D case as compared with its 2D analogue is the role played by the antisymmetric part of the deformation tensor. This coupling will be analyzed in section 4.2.2. The chapter ends with the description of a particularly interesting physical realization of an elastic deformation, a discussion about its physical implications and a summary of the main conclusions of the chapter[2].

[2]This chapter is based on "Vicente Arjona and María A.H. Vozmediano, *Rotational strain in Weyl semimetals: A continuum approach*, Physical Review B **97**, 201404 (R) (2018)".

4.1.1 Elasticity theory. Fundamental equations

The mechanics of solids, regarded as continuum media, is the subject of elasticity theory [243]. When external forces are applied, the system undergoes deformations in shape and volume. Deformations are mathematically described by the displacement $\mathbf{u}$ of a point at position $\mathbf{x}$ relative to the original position $\mathbf{x}_0$:

$$u^i = x^i - x_0^i, \tag{4.1}$$

with latin indices denoting the different components of the vector. Considering two points infinitesimally close, the deformation tensor $\hat{u}_{ij}$ is defined by the leading term in a Taylor expansion of the radius vector:

$$\mathrm{d}x^i = \mathrm{d}x_0^i + \frac{\partial u^i}{\partial x^j}\mathrm{d}x_0^j, \tag{4.2}$$

where $d\mathbf{x}_0$ and $d\mathbf{x}$ are the vectors joining the two points before and after the deformation, respectively, and $\hat{u}_{ij} = \partial_j u_i$. The symmetric part of $\hat{u}_{ij}$ defines the strain tensor u_{ij}, which is related to the distance $dl^2 = d\mathbf{x}^2$ between the points:

$$\mathrm{d}l^2 = \mathrm{d}l_0^2 + 2u_{ik}\mathrm{d}x^i\mathrm{d}x^k, \tag{4.3}$$

where the tensor u_{ij} is given as follows:

$$u_{ik} = \sum_l \frac{1}{2}\left(\frac{\partial u_i}{\partial x^k} + \frac{\partial u_k}{\partial u^i} + \frac{\partial u_l}{\partial x^i}\frac{\partial u_l}{\partial u^k}\right). \tag{4.4}$$

In elasticity theory, deformations acting on a system are regarded as small perturbations, and generally one can treat the components of u_{ij} as small terms. Being the last term in Equation (4.4) of second order, it can be neglected [243].

The symmetric tensor u_{ij} plays the main role in elasticity theory as well as in a geometric formulation, where it is identified as a metric. This follows directly from Equation (4.3), which can be read as:

$$g_{ij} = \delta_{ij} + 2u_{ij}, \tag{4.5}$$

where δ_{ij} is the identity matrix [243, 244]. In three dimensions, the antisymmetric part of the gradient deformation tensor,

$$\omega_{ik} = \frac{1}{2}\left(\frac{\partial u_i}{\partial x^k} - \frac{\partial u_k}{\partial u^i}\right), \tag{4.6}$$

is related to torsional deformations where the points are infinitesimally rotated

through some angle relative to those below them. This deformation plays an important role in the mechanics of solids and is represented by the pseudo-vector field (invariant under inversion transformations) $\mathbf{\Omega}$, which is related to the displacement vector $\mathbf{u}$ by:

$$\mathbf{\Omega} = \nabla \times \mathbf{u}. \tag{4.7}$$

The nature of this vector is better understood in fluid mechanics, where $\mathbf{u}$ represents the fluid velocity and $\hat{u}_{ij}$ measures the rate of change of the flow velocity in the neighborhood of a point. The vorticity vector $\mathbf{\Omega}$ is a pseudo-vector that characterizes the tendency of a fluid to generate whirlpools. $\mathbf{\Omega}$ is defined as the rotational of the fluid velocity [245], $\mathbf{\Omega} = \nabla \times \mathbf{u}$, and is related to the antisymmetric tensor ω_{ij} by:

$$\Omega^i = -\epsilon^{ijk}\omega_{jk}. \tag{4.8}$$

In 2D the antisymmetric part of the deformation gradient tensor is dual to a pseudo-scalar field, and does not play a major role in the dynamics ($-2\omega_{ij} = \epsilon_{ij}\Omega$).

4.1.2 Elastic deformations in Dirac crystals

Effects of the lattice deformations on the electronic properties of graphitic structures were described in the literature before the synthesis of graphene[3]. Lattice deformations couple to the electronic density of Weyl materials in the form of elastic gauge fields, constructed with the deformation tensor. This particular coupling was first derived in the context of carbon nanotubes [158, 240], and it was soon generalized to graphene flakes [248–250, 241] (see also Ref. [160]). The extraordinary mechanical attributes and flexibility of the material, and the potential of tuning their electronic properties by appropriate strain geometries, opened the pathway for a prolific industry associated with straintronics [251, 246]. An important highlight in the development of the field was the recognition of a reorganization of the energy spectrum into quantized Landau levels due to the emergence of an effective magnetic field in strained graphene [163, 159, 252] (see Figure 4.1).

The emergence of elastic gauge fields in 3D Weyl semimetals (deduced in Ref. [161]) has been followed by multiple studies analyzing their physical consequences [165, 167, 166, 175]. An experimental realization of strain-induced pseudo-magnetic fields (on the order of 3 Tesla) was recently observed in strained crystals of Re-doped $MoTe_2$ (see Figure 4.1), where Landau levels at zero applied magnetic field were detected in areas associated to rippled regions [239].

[3]The basics of the elastic deformations will be described in section 4.1.2, which is far from being an exhaustive review about elastic deformations. We refer the reviews [160, 8, 246, 247, 25] and references therein for further details.

Recent works shows that the influence of external deformations on the electronic properties of Dirac matter gives rise to different phenomena not captured by the elastic gauge fields. For a complete review about the different effects arising from strain in 2D Dirac materials, we refer the Ref. [247].

4.2 Electron-phonon couplings

The effective low-energy interactions between lattice deformations and electronic excitations under non-uniform strain can be organized using a systematic expansion in derivatives of the strain tensor and the electron field. Considering elastic deformations, each derivative of $\hat{u}_{ij}$ is suppressed by a factor of order $O(a/\lambda)$, where λ is the wavelength of the deformation and a is the lattice constant.

Any electron-phonon coupling respecting the symmetries of the system is allowed. The minimal low-energy model describing a Weyl semimetal with only two nodes of opposite chirality separated in energy-momentum space by a vector (b_0, b_i) is given by the Hamiltonian:

$$H_s = s v_F \sigma^i (k_i + s b_i) + s b_0 \mathbb{I}, \tag{4.9}$$

where $s = \pm 1$ denotes the chirality of each node. As mentioned in chapter 1, the vector b_μ and the Fermi velocity are the only intrinsic parameters of the material. The term involving the spatial components $\mathbf{b}$ breaks time-reversal symmetry, while the time component b_0 shifts the nodes to different energies and breaks inversion symmetry. In the case of a Weyl semimetal, Weyl nodes are often located at points in the Brillouin zone without any particular symmetry. We restrict the construction to this case and perform a derivation based on the continuum model given in Equation (4.9), where the only symmetries are rotations in the plane perpendicular to the vector $\mathbf{b}$. This approach does not provide the numerical value of the coupling constants, which remains arbitrary. Generalized tight-binding approximations [161, 164, 165], *ab-initio* calculations or experimental data should be used in order to estimate their values.

As our main interest lies in the description of quasiparticle excitations around the Weyl nodes, where the electrons disperse linearly, we restrict ourselves to interaction terms that are, at most, linear in the electron-momentum $\mathbf{k}$. Within the domain of elasticity theory, where deformations are regarded as small, only terms linear in the deformation tensor are considered. In this way, the effective interactions will be a function of the deformation tensor $\hat{u}_{ij}$, the vorticity vector $\mathbf{\Omega}$, the electron fields ψ and their derivatives.

$\mathbf{H_i}$	**Electron-phonon coupling**	**Physical interpretation**	$\mathbf{K_2}$
H^s_1	$\mathrm{Tr}(u_{ij})$	Deformation potential	+
$H^s_{2,0}$	$\sigma^0 A_0,\ A_0 = u_{\|\|} b_0$	Pseudo-scalar gauge potential	-
$H^s_{2,i}$	$\sigma^i A_i,\ A_i = u_{ij} b^j$	Pseudo-vector gauge field	-
H^s_3	$u_{ij}\sigma^i k^j$	Space-dependent Fermi velocity	+
H^s_4	$u_{ij} w^i k^j$	Space-dependent tilt velocity	+
H^s_5	$k^i A_i$	Dirac cone tilt	-
H^s_6	$\epsilon^{ijk}\sigma_i \partial_j b_k,\ \epsilon^{ijk}\sigma_i \partial_j A_k$	Pseudo-Zeeman field	-

TABLE 4.1: Lowest-order effective low-energy Hamiltonians for the electron-phonon interactions associated with the standard strain tensor. The different terms presented here describe the interactions around one Weyl node. The relative sign of its corresponding partner (separated in momentum space) is given in column K_2.

4.2.1 The strain tensor. Effective electron-phonon interactions

For the case of three-dimensional materials, the couplings of the electronic density to the symmetric strain tensor defined in Equation (4.4) are very similar to these already known in the graphene system [242]. Some couplings, especially those related to elastic gauge fields, have been already discussed in the literature.

The complete list of terms is summarized in Table 4.1. The column K_2 indicates the relative sign of the coupling sitting on the corresponding chiral partner, separated in reciprocal space by the vector $\mathbf{b}$. In what follows we will describe the physical consequences of the different terms.

Deformation potential

The simplest deformation that one can consider is due to changes in the volume of the unit cell, originated by either contraction or dilation of the sample [158, 8]. Volume differences give rise to local fluctuations in the electron density, shifting the energy bands of the material (an effect similar to that of a chemical potential). It is mathematically represented by the trace of the deformation tensor. Deformation potentials were thought of as a general perturbation whose only effect was related to energy displacements of the Dirac cones. Nevertheless, they play a significant role when (pseudo) magnetic fields are present, as will be discussed in the next chapter.

Pseudo-gauge fields

Elastic deformations modify the local bond length between hoppings, leading to effective gauge potentials that couple with opposite sign to each chiral node[4]. The spatial separation between nodes (introduced in Equation (4.9)) is affected by the local displacements,

$$b_i \longrightarrow \tilde{b}_i = b_i + u_{ij} b^j, \tag{4.10}$$

giving rise to elastic vector potentials $A_i = u_{ij} b^j$. Suitable non-uniform configurations can induce time-reversal breaking vectors (hence, elastic gauge fields) which are position-dependent. As a result, we can define fictitious pseudo-magnetic fields which couple with different sign to each of the chiralities. The elastic vector potential was first derived in Ref. [161], which was followed by a number of works discussing their physical consequences and paving the way for Weyl semimetals straintronics [165, 166, 175, 253, 168–172, 25]. The coupling written in $H^s_{2,i}$ is only valid for time-reversal symmetry broken Weyl semimetals; other forms of strain-induced potentials have been found for materials where the Weyl nodes are protected by lattice symmetries [171].

The Weyl nodes are separated not only in space, but they can be shifted in energy. Elastic deformations also contribute to this energy distance, as demonstrated in $H^s_{2,0}$. The time component b_0 couples to the elements of the strain tensor $u_{||}$ that are parallel to the vector $\mathbf{b}$. The resulting coupling is a pseudo-scalar (inversion symmetry breaking term) that changes (in opposite directions) the position of the Weyl nodes, resulting in a strain-induced contribution to the chiral magnetic effect [162].

Strain-dependent Fermi velocity

The Fermi velocity is one of the intrinsic parameters of the model, and all measurable quantities depend on it. Space-dependent Fermi velocity originates from inhomogeneous elastic disorder, which is endonced by the coupling H^s_3. The strain-induced velocity has associated two contributions:

$$v_{ij} \longrightarrow \tilde{v}_{ij} = v(\mathrm{Tr}(u)\delta_{ij} + u_{ij}) \tag{4.11}$$

where the first (second) term is the isotropic (anisotropic) Fermi velocity. Anisotropic position-dependent Fermi velocities have been discussed in the context of cubic Weyl semimetals and may be interpreted as emergent gravitational field [167].

[4]These axial gauge fields are absent in high energy physics, where they would play an important role related to the chiral anomaly.

Strain-dependent tilt velocity

As mentioned in chapter 1, a generic feature in Weyl and Dirac semimetals is that the cone of the linear dispersion relation may be tilted [254–258, 133, 134]. These tilted Dirac cones are described by the term $H_{\text{tilt}} = w^i k_i \mathbb{I}$, where w^i denotes the tilt velocity, another intrinsic parameter of the material. In the same way as the Fermi velocity, the tilt parameter can be modified under lattice deformations, making it inhomogeneous through the sample for non-uniform strain (H_4^s term):

$$w^i \longrightarrow \tilde{w}^i = w^i + u_{ij} w^j. \tag{4.12}$$

Nevertheless, strain deformations contribute with an additional term to $\mathbf{w}$. The pseudo-vector $\mathbf{A}$ is able to tilt the dispersion relation of an originally untilted Weyl semimetal in opposite directions, interaction that is described by the term H_5^s. Being proportional to the separation between the nodes, this coupling only arises in Weyl semimetals. The combination of these two terms opens the possibility of a strain-induced Lifshitz transition [129, 259, 258, 260, 134, 261], i.e., going from Type-I to Type-II Weyl semimetal by applying strain (or vice versa). Since the Fermi velocity is also affected by elastic deformations, the condition for the transition becomes $||\mathbf{t}|| > 1$, where the vector $\mathbf{t}$ is given by the expression:

$$t_i = (w_l + u_{lj} w_j + A_l)(\tilde{v}^{-1})_{li} \tag{4.13}$$

and $\tilde{v}_{li} = v_{li} + u_{li}$ is the space-dependent Fermi velocity. This type of tunability has been discussed in Ref. [262], where the orthorhombic Weyl semimetal Ta_3S_2[5], regarded as one of the most robust Weyl semimetals, exhibits a transition from Type-II to Type-I Weyl semimetal as one increases the lattice constant b. By further increasing this parameter, the system develops a topological phase transition into a topological insulator state, as the two chiral nodes have annihilated with each other and the spectrum becomes fully gapped.

Pseudo-Zeeman term

A Zeeman term can be constructed with the derivative acting on the vector $\mathbf{b}$. Although $\mathbf{b}$ is constant inside the sample, it will always go to zero at the boundary of finite samples, giving rise to an effective pseudo-magnetic field confined to the boundary as discussed in Ref. [265] (see also Ref. [25]). For the sake of clarity, let us consider as an example a cylinder of height L and radius a with the simplest configuration $\mathbf{b} = b_z \Theta(a - |\mathbf{r}|)\hat{z}$. This separation will produce a pseudo-magnetic

[5] Ta_3S_2 is a semimetallic compound with the space group *Abm*2. The lattice constants are $a = 5.6051$ Å, $b = 7.4783$ Å, $c = 17.222$ Å [262–264].

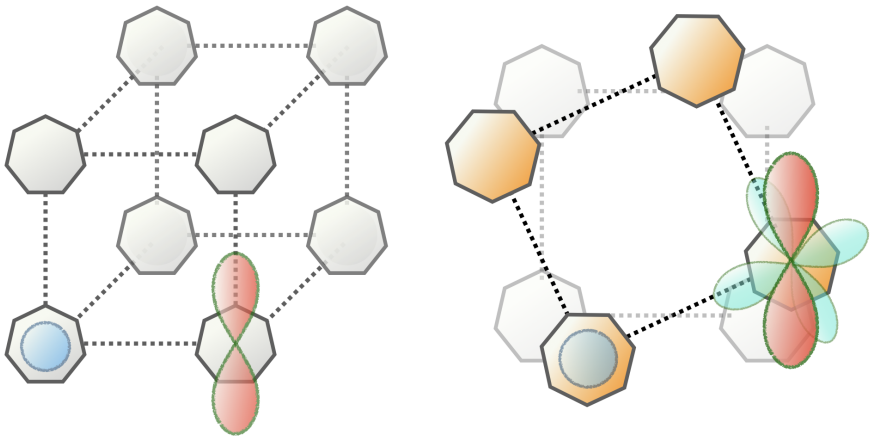

FIGURE 4.2: *(Left)*: Schematic illustration of a cubic lattice. Considering a pair of s and p orbitals, the structural configuration depicted in the image does not allow any interaction between the atomic orbitals. *(Right)*: The relative orientation between the atoms is modified by applying a rotational perturbation. The new alignment gives rise to new hoppings not allowed previously by the symmetry of the system [266].

field pointing in the azimuthal direction and proportional to $B_\Theta \propto b_z \delta(a - |\mathbf{r}|)$. Associated to this magnetic field there will be a corresponding Zeeman term $H = \sigma^\Theta B_\Theta$. The elastic magnetic field defined through $H^s_{2,i}$ will lead to a pseudo-Zeeman term $H = \sigma_i \epsilon^{ijk} \partial_j A_k$.

4.2.2 Antisymmetric deformation tensor. Effective electron-phonon interactions

The strain gradient tensor u_{ij} can be defined from the change in the bond length due to deviations of the atomic orbitals from the equilibrium values. Additional contributions to the overlap hopping matrix arise from the relative orientation seen from the adjacent sites (see Figure 4.2). As a result, new effective couplings, prohibited by symmetry arguments in the unstrained case, become permitted as a consequence of the relative rotation of the relevant orbitals when strain is applied [266, 164, 161]. The antisymmetric tensor ω_{ij} characterizes this kind of elastic deformations, the relative rotation between atoms being described by the vorticity vector $\mathbf{\Omega}$. Contrary to the general elastic gauge field, $\mathbf{\Omega}$ is independent of the separation between the

$\mathbf{H_i}$	**Electron-phonon coupling**	**Physical interpretation**	$\mathbf{K_2}$
H_1^a	$\Omega_i b^i$	Deformation potential	+
H_2^a	$\sigma^i \omega_{ij} b^j,\ \sigma^i \Omega_i$	Pseudo-vector gauge field	-
H_3^a	$\omega_{ij} w^i k^j,\ \Omega_i k^i$	Dirac cone tilt	-
H_4^a	$\epsilon^{ijk} \sigma_i k_j V_k$	"Antisymmetric" Fermi velocity	

TABLE 4.2: Lowest-order effective low-energy Hamiltonians for the electron-phonon interactions associated with the antisymmetry tensor ω_{ij}. New couplings not present in the symmetric case originate from the vorticity vector.

Weyl nodes and its couplings will be present in Dirac semimetals. As was done in section 4.2.1, the complete list of effective couplings related to the antisymmetric strain tensor to first order in derivatives is summarized in Table 4.2. The different interacting terms are organized in a derivative expansion, where each term is referred to one of the Weyl nodes and K_2 gives the relative sign of the chiral partner.

Scalar potential

An interesting observation concerns the coupling between the node separation **b** and the vorticity vector. Being both pseudo-vectors (they do not break inversion symmetry), their pairing will produce a rotational contribution to the deformation potential. Being independent of the strain tensor, it implies that a scalar potential can be generated from volume preserving deformations, as in the case of local rotations. This result implies a promising new pathway for achieving specific, space-dependent electron densities from elastic perturbations without altering the volume of the sample.

Pseudo-gauge fields

Rotational deformations give rise to two novel axial gauge fields. The first vector potential $H = \sigma^i \omega_{ij} b^j$ involves the Weyl node separation and is the antisymmetric analog to the term derived in $H^s_{2,i}$ of Table 4.1. Interestingly, the second coupling $H = \sigma^i \Omega_i$ does not depend on **b**, which implies that rotational deformations can induce a transition from Dirac to Weyl semimetals similar to that discussed in Ref. [267]. In fact, we can generate pseudo-magnetic fields from space-dependent vorticity vectors, following a similar approach as proposed in Ref. [165].

Strain-dependent tilt velocity

Both strain-induced vectors $\mathbf{\Omega}$ and $\omega_{ij}w^j$ will induce opposite tilts in the two nodes. As in the previous case, being independent of the Weyl node separation, the coupling $\Omega_i k^i$ will tilt the cones in any Dirac material. These two contributions will be added to Equation (4.13) to promote the Lifshitz transition between Type-I and Type-II Weyl semimetals [262].

Antisymmetric Fermi velocity

The term described in H_4 deserves an appropriate treatment as it brings interesting consequences to the electron-phonon derivation. This term can be regarded as an antisymmetric contribution to the Fermi velocity since it concerns a tensor whose components are antisymmetric, $\epsilon_{ijk}V^k \equiv \mathcal{V}_{ij}$. As it was shown in Ref. [242], the antisymmetric contribution to the Fermi velocity vanishes in the case of 2D Dirac materials (a detailed derivation is found in appendix C), where a spinor rotation completely cancels the antisymmetric term. The 3D case is more involved, as the relations between the Pauli matrices include an extra δ-term not present in 2D systems, where σ^z is a privileged matrix.

Consider the generic Hamiltonian described in H_4^a, where V_k is an arbitrary field. Due to the commutation relation of the Pauli matrices,

$$\sigma_a\sigma_b = i\epsilon_{abc}\sigma^c + \delta_{ab}, \tag{4.14}$$

and using the symmetric convention for the derivatives acting on the electron fields,

$$\psi^\dagger k_j \psi \to -\frac{i}{2}\psi^\dagger \overleftrightarrow{\partial_j}\psi \equiv -\frac{i}{2}\left(\psi^\dagger\partial_j\psi - \partial_j\psi^\dagger\psi\right), \tag{4.15}$$

a spinor rotation

$$\psi \to \psi' = e^{i/2\,\sigma^k V_k}\psi \tag{4.16}$$

cancels the antisymmetric term, leaving behind a term proportional to the divergence of the vector $\mathbf{V}$ (all the technical details about this calculation are included in appendix C). Depending on the nature of $\mathbf{V}$, this effective coupling will contribute to the low-energy Hamiltonian as a scalar potential ($\mathbf{V}$ is a vector) or to the energy separation b_0 ($\mathbf{V}$ is a pseudo-vector). In the case of a strained Weyl semimetal, we have at our disposal three vectors (separation between nodes $\mathbf{b}$, elastic gauge fields $\mathbf{A}$, vorticity vector $\mathbf{\Omega}$) that couple to the electronic degrees of freedom in the form suggested by H_4^a.

The first term to be considered is the vorticity vector, $H = \epsilon^{ijk}\sigma_i k_j \Omega_k$. Using the definition of $\mathbf{\Omega}$, this term follows from the Fermi velocity originated by the

antisymmetric tensor; $\omega_{ij}\sigma^i k^j$. The resulting Hamiltonian after the spinor rotation is $H = \boldsymbol{\nabla}\cdot\boldsymbol{\Omega}$. Being the divergence of a curl, this term is zero. The antisymmetric part of the Fermi velocity vanishes for Dirac and Weyl materials.

An interesting coupling that emerges from the previous example is a strain-independent term proportional to the node separation. The Hamiltonian $H = \epsilon^{ijk}\sigma_i k_j b_k$ can be rotated to $H = \boldsymbol{\nabla}\cdot\mathbf{b}$, term that will induce a pseudo-scalar potential similar to b_0 confined at the boundaries of the sample, where the separation between the nodes goes to zero. This interaction is a pseudo-scalar (breaks inversion symmetry) and will induce an energy separation between the nodes. When non-uniform strain is applied, $\mathbf{b}$ will be inhomogeneous through the sample, giving rise to two space-dependent axial gauge fields $H^s_{2,i}$ and $H^a_{2(2)}$. After performing the spinor rotation explained above, the resulting inversion-breaking term $H = \boldsymbol{\nabla}\cdot\mathbf{A}$ will contribute to the energy separation b_0. Being proportional to $\hat{u}_{ij}$, this term is of higher order in derivatives of the strain that the one described in $H^s_{2,0}$. Both terms will contribute to the chiral magnetic effect in a similar fashion to the mechanism discussed in Ref. [162], where the intrinsic parameter b_0 is modified under elastic deformations in order to change the locations of the Weyl cones.

4.3 Physical example. Realistic strain configuration

In this section we present a feasible realization of Dirac matter under strain. This configuration was originally proposed in Ref. [165] to generate a constant pseudo-magnetic field and study the emergence of pseudo-Landau levels. We will show that new extra terms will be generated from the given configuration, which may alter previous results.

In order to probe strain-induced phenomena in Dirac matter is recommendable to concentrate on films or wire-shaped materials: the mechanical flexibility of such geometries allows the sample to support a considerable strain without breaking, much better than bulk crystals. We will analyze the effect of elastic deformations on nanowires of Dirac semimetal Cd_3As_2, a material that has exhibited an impressive mechanical flexibility and suitable bending attributes. The Dirac semimetal Cd_3As_2 presents a complicated crystal structure that can be regarded as tetragonally distorted array with *Cd*-site vacancies [102]. The low-energy model captures the semimetallic nature of the crystal with a symmetry protected band crossing point along the $\Gamma - Z$ direction. The effective Hamiltonian is made of two decoupled sub-blocks, where each individual block characterizes a time-reversal breaking Weyl semimetal with the pair of Weyl nodes sitting at different $\mathbf{K}_\pm$ points in the reciprocal space. Time-reversal symmetry is restored when the two copies are considered, each "Weyl sub-block" being the chiral partner of the other [102, 165]. Therefore, the tight-binding

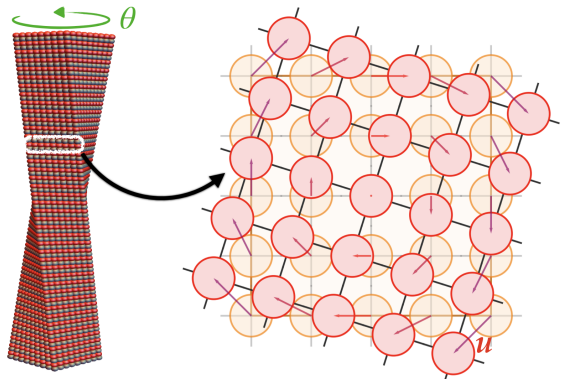

FIGURE 4.3: Schematic representation of the wire-shaped nanowire considered for this section. The sample is twisted a total angle θ, which introduces a misalignment between adjacent layers. Adapted from Ref. [165].

model provides a material with two Weyl nodes separated along the z-direction by a vector $\mathbf{b} = b\,\hat{\mathbf{z}}$. Assuming a wire-shaped crystal of length L with an axis along the z-direction, the displacement vector $\mathbf{u}$ that derives from twisting the sample an angle θ is given by:

$$u^i = \theta \frac{z}{L} \epsilon^{ijk} r_j \hat{z}_k \tag{4.17}$$

where $\mathbf{r}$ denotes the position relative to the origin located on the axis of the wire and $\hat{\mathbf{z}}$ is the unit vector along the z-direction, as illustrated in Figure 4.3. The strain tensor associated with the deformation written in Equation (4.17) is traceless, meaning that the deformation potential generated from the symmetric deformation will be zero. Equation (4.17) has an associated elastic gauge field[6]:

$$A_i = u_{ij} b^j \rightarrow \mathbf{A} = \frac{\theta b}{2L}(y, -x, 0), \tag{4.18}$$

and the corresponding uniform magnetic field:

$$B^i_{\text{el}} = \frac{\hbar}{e} \epsilon^{ijk} \partial_j A_k \rightarrow \mathbf{B}_{\text{el}} = -\frac{\hbar}{e} \frac{\theta}{L} b\,\hat{\mathbf{z}}. \tag{4.19}$$

As explained before, we will analyze the novel contributions arising from the antisymmetric part of the gradient deformation tensor, described in the previous section.

[6]When defining the fictitious fields induced by the elastic deformations in Equations (4.19) and (4.22), we have introduced the required constants in order to resemble the physical units of their electromagnetic analogues.

Following Equation (4.8), the vorticity vector associated to this deformation is

$$\mathbf{\Omega} = \frac{\theta}{L}(x, y, -2z), \tag{4.20}$$

which leads to a deformation potential proportional to the antisymmetric part of the deformation tensor:

$$\xi = \Omega_i b^i = -2\frac{\theta}{L} bz. \tag{4.21}$$

Even though the applied deformation is traceless i.e., it preserves the volume of the wire, it is still able to produce a scalar field through the vorticity vector. Without considering time-dependent deformations, the strain-induced scalar potential will create an elastic electric field parallel to the field $\mathbf{B}_{\text{el}}$:

$$E_i^{\text{el}} = -v_{\text{F}}\frac{\hbar}{e}\frac{\partial \xi}{\partial x^i} \rightarrow \mathbf{E}_{\text{el}} = 2v_{\text{F}}\frac{\hbar}{e}\frac{\theta}{L} b\,\hat{\mathbf{z}}. \tag{4.22}$$

Unlike the axial-electric field that one could get from the trace of the deformation tensor (described in H_1^s), the resulting term stemming from the antisymmetric part is a regular vector and couples with the same sign to the two chiralities. The product of these two synthetic vectors will not ignite the chiral anomaly since the vector $\mathbf{E}_{\text{el}}$ cancels the contribution generated by the two cones (such scenario does not promote a charge pumping between the Weyl points).

Following the anomaly equations when both ordinary and chiral electromagnetic fields are present [173, 179, 265, 22], a pumping of charge will flow between the two chiral partners when a real magnetic field $\mathbf{B}$ along the z-direction is present:

$$\partial_t \rho_5 + \boldsymbol{\nabla}\cdot\mathbf{j}_5 = \frac{e^2}{2\pi^2\hbar^2}(\mathbf{E}\cdot\mathbf{B} + \mathbf{E}_5\cdot\mathbf{B}_5), \tag{4.23}$$

where $\rho_5 = \rho_{\text{R}} - \rho_{\text{L}}$ is the chiral density and $\mathbf{E}_5$, $\mathbf{B}_5$ denotes chiral electromagnetic fields[7]. As suggested in Ref. [165], the proposed strain configuration will give rise to an electric current characterized by the chiral anomaly equation:

$$\partial_t \rho + \boldsymbol{\nabla}\cdot\mathbf{j} = \frac{e^2}{2\pi^2\hbar^2 c}(\mathbf{E}\cdot\mathbf{B}_5 + \mathbf{E}_5\cdot\mathbf{B}). \tag{4.24}$$

Equation (4.24) only occurs when both chiral and real electromagnetic fields are present. Being the electric current strictly conserved in real solids, Equation (4.24)

[7] As discussed before, whereas the pseudo-magnetic field generated with strain couples with opposite sign to the two chiralities, i.e. $\mathbf{B}_{\text{el}} = \mathbf{B}_5$, the electric field $\mathbf{E}_{\text{el}}$ described in Equation (4.22) behaves in the same way as a real electric field, $\mathbf{E}_{\text{el}} = \mathbf{E}$. For the proposed geometry, chiral electric fields $\mathbf{E}_5$ can be originated from time-dependent elastic deformations, $E_5^i = -\partial_t A_{\text{el}}^i$.

is understood as a charge-density current flowing from the bulk to the edges of the system that only arises in strained Dirac crystals [165].

The deformation characterized in Equation (4.17) will develop a tilted dispersion relation (opposite at each node) due to the contributions described in Tables 4.1 and 4.2:

$$\tilde{w}_i = g_1 u_{ij} b^j + g_2 \omega_{ij} b^j + g_3 \Omega_i, \tag{4.25}$$

where g_i are the different coupling constants. As discussed in Section 4.2.1, H_6^s is a new term describing the coupling between the spin components and the pseudo-magnetic field $\mathbf{B}_{\text{el}}$. This term is interpreted as a strain tunable pseudo-Zeeman term, which breaks the spin degeneracy and comes with opposite signs in the two Dirac points.

4.4 Conclusions and discussion

In this chapter, we have used a symmetry approach to construct effective electron-phonon couplings affecting the low-energy quasiparticle excitations of Dirac and Weyl semimetals. We have defined our derivation within the framework of elasticity theory, setting up a systematic expansion in derivatives of the deformation tensor. Higher order corrections are strongly suppressed in many experimental situations (each derivative of the deformation tensor is suppressed by a factor of order $O[a/\lambda]$), and they do not contribute with new significant physical phenomena.

Contrary to the 2D case, antisymmetric contributions to electron-phonon couplings stem in Weyl and Dirac semimetals, and lead to new effective terms that enrich the scenario of elastic deformations-induced effects. The orbital character of the tight-binding models in Weyl semimetals makes rotational strain particularly relevant, inducing new orbital couplings that were forbidden by symmetry in the unperturbed case. This provides a richer scenario than that present in graphene and similar 2D Dirac systems, where the relevant orbitals characterizing the model are p_z orbitals perpendicular to the plane, leaving the distance between neighboring atoms as the only parameter susceptible of being modified under elastic deformations. The vorticity vector $\mathbf{\Omega}$, which represents the relative rotation between the atomic positions, plays the main role in the antisymmetric contribution to the low-energy description of the effective actions, generating new couplings not present in 2D systems, where the dual to the antisymmetric part of the gradient deformation tensor is a scalar field. Of special interest is the volume-preserving deformation potential, a scalar term that does not involve the trace of the strain tensor, or the tilt parameter. Being independent of the momentum (or energy) separation between the nodes, $\mathbf{\Omega}$ will couple to both Weyl or Dirac semimetals.

For the sake of completeness, we have included the terms associated with the symmetric strain tensor, which are analogous to these extracted in Ref. [242]. This brings to light the close relation between antisymmetric deformations and 3D Dirac materials and highlights the vorticity-induced terms as a distinctive property of Dirac and Weyl semimetals.

Part of the interest in emerging axial vector fields associated with elastic deformations lies on the possibility of generating elastic or mixed electromagnetic-elastic responses like the ones discussed in early works [268]. We have seen an example of this phenomena in the considered example, where a nanowire of Dirac semimetal Cd_3As_2 is subjected to torsional strain. The applied strain induces an elastic magnetic and electric fields able to ignite the chiral anomaly and an electric current between the bulk and the boundaries of the sample [165].

The influence of antisymmetric deformations on the thermo-electric properties of 3D Dirac materials has been investigated in a recent publication [269]. The results indicate that the thermoelectric transport coefficients in Weyl semimetals can be tailored by appropriate tuning of the magnetic field strength, the torsional deformation and the thermal gradient, giving rise to large figure of merit and proving the potential of straintronics in Dirac materials.

Chapter 5

Collapse of Landau levels in Weyl semimetals

5.1 Introduction

In the previous chapter, we detailed the different effective electron-phonon couplings arising from lattice deformations induced by strain. These interactions were constructed based only the underlying symmetry of the system.

Arguably, the coupling of electronic degrees of freedom to lattice deformations in the form of vector fields similar to the electromagnetic potential is one of the most interesting features in the field of strained Dirac materials [158, 160, 161]. This observation paved the way to investigate different strain configurations that would induce a constant magnetic field able to quantize the spectrum into pseudo-Landau levels [159, 165, 166, 175]. The subsequent experimental observation with scanning tunneling spectroscopy [163, 239] is considered as a milestone in the physics of Dirac systems (see Figure 5.1). The concept of elastic gauge field and the potential to manipulate the electronic excitations by means of elastic deformations opened a new research field called straintronics [251, 25, 166, 169, 172].

The relativistic nature of the massless quasiparticles has important consequences on the properties of these materials. One of the best explored in the literature is, precisely, the behaviour of the electronic excitations in magnetic fields. On the one hand, the Landau level spectrum differs from that of the standard electron systems: the dispersion relation is proportional to $\sqrt{B}$ and $\sqrt{n}$, in contrast to the linear dependence of the classical case[1]. On the other hand, the characteristic zeroth

[1]This characteristic dependence was the compelling evidence of having Dirac electrons in graphene [6, 7].

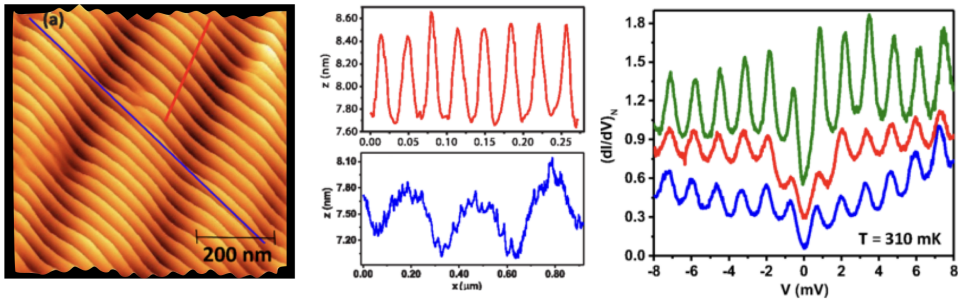

(a) *(b)* *(c)*

FIGURE 5.1: *(a)*: STM topograph of the Weyl semimetal Re – $MoTe_2$ surface. Strain-induced ripples can be observed in the image. *(b)*: Periodic height variation due to topographic modulations along the cuts (red and blue lines) shown in Figure 5.1(a). *(c)*: Tunneling spectra measured at different points in the strained region. The image reveals strain-induced Landau levels oscillations. Adapted from Ref. [239].

Landau level plays an important role in the discussion of the chiral anomaly in Weyl semimetals [270], and its negative contribution to the magnetoresistance has become the standard test of the anomaly [271, 272, 78–80].

In the presence of a perpendicular electric field **E**, the Landau level spectrum develops a non-trivial dependence with the electric field that renormalizes the cyclotron frequency [273, 274]. Whereas the level spacing is independent of **E** in the non-relativistic case, the Landau spectrum for the case of Dirac systems is affected by the **E**-dependent frequency. Noticeable, the whole quantized spectrum collapses when the electric field is beyond a critical value [274, 275]. The underlying mechanism behind this phenomenon is the combination of special relativity (the recognition that different inertial observers will measure different electric and magnetic fields) and electrodynamics. This fact was first explored in two spatial dimensions for the case of graphene in Refs. [274, 275], and it has been also recognized in a different context when analyzing the magnetoresponse of Type-II Weyl semimetals[2] [259, 258].

In light of this result, it is natural to ask if pseudo-magnetic fields could also be affected by this kind of phenomena. In this chapter we will explain how specific strain patterns will induce the collapse of the pseudo-Landau levels via the same

[2]Tilted Dirac materials in the presence of a magnetic field were previously studied in 2D organic compounds [254, 255, 257]. These materials also displayed the characteristic transition from Landau level quantization to continuous spectra, depending on the orientation between the tilt and the magnetic field.

mechanism to that previously discussed for the case of real electromagnetic fields. This phenomenon has already been considered for graphene systems in Ref. [276].

The chapter is organized as follows. First, for completeness, we will review some basic concepts about Lorentz symmetry and how the electromagnetic field tensor transforms under the elements of the Lorentz group. Then, Lorentz transformations will be adopted as a tool to solve the spectrum of Dirac and Weyl semimetals in the presence of perpendicular electric and magnetic fields. After a brief description of the classical case (it will be helpful in emphasizing the differences with its relativistic counterpart), we will show how a perpendicular electric field introduces a non-trivial dependence on the cyclotron frequency of Dirac materials able to destabilize the quantized spectrum. We will extend this situation to strained Dirac materials by considering the different terms induced by strain analyzed in chapter 4. Finally, we will discuss the physical implications of particular deformations on Dirac materials[3].

5.1.1 Lorentz transformations

An intrinsic principle in physics is the invariance of the physical laws in all inertial reference frames [277, 278]. This symmetry is the first postulate of the special theory of relativity introduced by Einstein [279], which imposes that any physical theory must be invariant under Lorentz transformations relating two inertial coordinate systems[4].

At the end of the 19th century, it was already known that Maxwell's theory of electromagnetism was inconsistent with the principle of Galilean relativity. Lorentz transformations were introduced in 1904 by Lorentz, who sought symmetry transformations that kept the Maxwell's equations covariant [281, 278]. It was due to Einstein and his theory of special relativity who generalized the covariance of the physical laws beyond electromagnetic theory.

Mathematically, the Lorentz group is defined as the group of linear coordinate transformations

$$x^\mu \longrightarrow x'^\mu = \Lambda^\mu{}_\nu x^\nu \tag{5.1}$$

that leave invariant the space-time interval $\mathrm{d}s^2 = g_{\mu\nu}\mathrm{d}x^\mu \mathrm{d}x^\nu$. This condition is formally expressed as:

$$g_{\rho\sigma} = g_{\mu\nu}\Lambda^\mu{}_\rho \Lambda^\nu{}_\sigma. \tag{5.2}$$

[3]This chapter is based on "Vicente Arjona, Eduardo V. Castro and María A.H. Vozmediano, *Collapse of Landau levels in Weyl semimetals*, Physical Review B **96**, 081110 (R) (2017)".

[4]General relativity broadens this statement to *all* reference frames [280]. Within this framework, the global condition of Lorentz invariance becomes a local symmetry in the presence of matter, the latter being directly related to the curvature of space time.

In three spacial dimensions, the Lorentz group is isomorphic to $O(1,3)$ with infinitesimal generators $J^{\mu\nu}$ and the associated commutation relation:

$$[J^{\mu\nu}, J^{\rho\sigma}] = i\left(g^{\nu\rho}J^{\mu\sigma} - g^{\mu\rho}J^{\nu\sigma} - g^{\nu\sigma}J^{\mu\rho} + g^{\mu\sigma}J^{\nu\rho}\right). \tag{5.3}$$

From Equation (5.2) if follows that

$$(\Lambda^0{}_0)^2 \geq 1 \qquad \det\Lambda = \pm 1. \tag{5.4}$$

The subset of Lorentz transformations having positive determinant and component $\Lambda^0{}_0 \geq 1$ forms a subgroup, called the *Proper Lorentz group*. Their elements are connected with the identity by successive infinitesimal transformations. They can be decomposed into 3D spatial rotations and *boosts* relating the coordinate systems of two inertial observers. Discrete operations (parity and time-reversal) should be added to the set of transformations of the Lorentz group.

Any Lorentz transformation Λ can be written as a product of rotations R (parametrized by three angles $\boldsymbol{\theta} = (\theta_1, \theta_2, \theta_3) \in [0, 2\pi]$ around the three elementary axes) and boosts transformations L, which are characterized by the three components of the *rapidity* parameter $\boldsymbol{\eta} = (\eta_1, \eta_2, \eta_3) \in (-\infty, +\infty)$. These elements can be obtained by exponentiating the generators $J^{\mu\nu}$:

$$\Lambda^{\alpha}{}_{\beta} = (\exp[-i\omega_{\mu\nu}J^{\mu\nu}/2])^{\alpha}{}_{\beta}, \tag{5.5}$$

where $\omega_{\mu\nu}$ are the parameters of the transformation[5]. A set of matrices (or linear operators) satisfying the commutation relations in Equation (5.3) yields, through exponentiation, a representation of the Lorentz group. In the 4-vector representation, it is straightforward to see that the 4×4 matrix

$$(\mathcal{J}^{\mu\nu})^{\alpha}{}_{\beta} = i(g^{\mu\alpha}\delta^{\nu}{}_{\beta} - g^{\nu\alpha}\delta^{\mu}{}_{\beta}) \tag{5.6}$$

satisfies the algebra described in Equation (5.3). Upon explicitly expanding Equation (5.5) in a power series, one can write an explicit representation of the Proper Lorentz group:

$$R_x = \begin{pmatrix} 1 & 0 & 0 & 0 \\ 0 & 1 & 0 & 0 \\ 0 & 0 & c_\theta & -s_\theta \\ 0 & 0 & s_\theta & c_\theta \end{pmatrix}, \; R_y = \begin{pmatrix} 1 & 0 & 0 & 0 \\ 0 & c_\theta & 0 & s_\theta \\ 0 & 0 & 1 & 0 \\ 0 & -s_\theta & 0 & c_\theta \end{pmatrix}, \; R_z = \begin{pmatrix} 1 & 0 & 0 & 0 \\ 0 & c_\theta & -s_\theta & 0 \\ 0 & s_\theta & c_\theta & 0 \\ 0 & 0 & 0 & 1 \end{pmatrix},$$

[5]The tensor $\omega_{\mu\nu}$ is related to the usual rotation $\boldsymbol{\theta}$ and rapidity $\boldsymbol{\eta}$ parameters by $\omega_{ij} = -\omega_{ji} = \epsilon_{ijk}\theta^k$ and $\omega_{0i} = -\omega_{i0} = \eta_i$.

and

$$L_x = \begin{pmatrix} \gamma & -\gamma\beta & 0 & 0 \\ -\gamma\beta & \gamma & 0 & 0 \\ 0 & 0 & 1 & 0 \\ 0 & 0 & 0 & 1 \end{pmatrix}, \; L_y = \begin{pmatrix} \gamma & 0 & -\gamma\beta & 0 \\ 0 & 1 & 0 & 0 \\ -\gamma\beta & 0 & \gamma & 0 \\ 0 & 0 & 0 & 1 \end{pmatrix}, \; L_z = \begin{pmatrix} \gamma & 0 & 0 & -\gamma\beta \\ 0 & 1 & 0 & 0 \\ 0 & 0 & 1 & 0 \\ -\gamma\beta & 0 & 0 & \gamma \end{pmatrix}, \tag{5.7}$$

with $c_\theta = \cos\theta$, $s_\theta = \sin\theta$ and $\gamma = 1/\sqrt{1-\beta^2}$. In deriving the boost transformations L_i, we have replaced the rapidity term η by the Lorentz factor γ and the velocity parameter $\beta = v/c$, which are related to η by:

$$e^\eta = \gamma + \gamma\beta. \tag{5.8}$$

The covariant formulation of any theory makes it explicitly Lorentz invariant; the equations of motion derived from a Lagrangian that is a Lorentz scalar will be systematically invariant under Lorentz transformations [27]. This result stems from the principle of least action: if Lorentz transformations leave the Lagrangian unchanged, the transformed extremum of the action will remain an extremum.

5.1.2 Electromagnetic field tensor and special relativity

Before the formulation of special relativity, Lorentz invariance was already discussed in the context of classical electromagnetism: Maxwell's theory of electromagnetism was incompatible with Galilean invariance. The laws describing classical electromagnetism can be written in a manifestly covariant language by means of a gauge and Lorentz invariant Lagrangian (in the absence of charge sources):

$$\mathcal{L}_{\text{EM}} = -\frac{1}{4\mu_0} F^{\mu\nu} F_{\mu\nu}, \tag{5.9}$$

where the electromagnetic field tensor is defined as $F_{\mu\nu} = \partial_\mu A_\nu - \partial_\nu A_\mu$ in terms of the electromagnetic gauge field A_μ. The explicit form of $F^{\mu\nu}$ as a function of the electric **E** and magnetic field **B** is:

$$F^{\mu\nu} = \begin{pmatrix} 0 & -E_x/c & -E_y/c & E_z/c \\ E_x/c & 0 & -B_z & B_y \\ E_y/c & B_z & 0 & -B_x \\ E_z/c & -B_y & B_x & 0 \end{pmatrix}. \tag{5.10}$$

One can easily recover the traditional Maxwell's equations by applying the Euler-Lagrange equations to Equation (5.9) with respect A_μ.

Even though the Lagrangian formulated in Equation (5.9) is a Lorentz scalar (the physical laws will be the same for all inertial frames), the physical observables of the theory will depend on the reference frame where they are measured. The electric and magnetic fields will have different magnitudes for two inertial observers. Using the expressions obtained in Equation (5.7), the electric and magnetic fields measured in different inertial frames moving at relative velocity $\mathbf{v}$ are related by the equations:

$$\begin{aligned}
\mathbf{E}'_{\parallel} &= \mathbf{E}_{\parallel} \\
\mathbf{E}'_{\perp} &= \gamma \left(\mathbf{E}_{\perp} + \mathbf{v} \times \mathbf{B}\right), \qquad (5.11) \\
\mathbf{B}'_{\parallel} &= \mathbf{B}_{\parallel} \\
\mathbf{B}'_{\perp} &= \gamma \left(\mathbf{B}_{\perp} - 1/c^2\, \mathbf{v} \times \mathbf{E}\right). \qquad (5.12)
\end{aligned}$$

As anticipated before, the electric and magnetic fields, like the majority of physical quantities, are relative to the reference frame: an electric field measured by one observer appears to be a magnetic field to another, and vice versa. Electromagnetic vectors $\mathbf{E}$ and $\mathbf{B}$ do not exist as independent entities, but their decomposition into electric and magnetic components depends on the relative movement of the observer.

5.2 Collapse of the Landau levels

In what follows, we will present the derivation of the Landau levels collapse in perpendicular electric and magnetic fields to fix the notation and to pave the way for the discussion of strain in the next section. The case of perpendicular, uniform $\mathbf{E}$ and $\mathbf{B}$ has been already discussed in tilted Weyl semimetals when analyzing their optical conductivities and magnetic properties in Refs. [258, 259]. We will begin the discussion by reviewing the behaviour of non-relativistic matter in perpendicular magnetic and electric field.

5.2.1 Hall regime in non-relativistic electrons

The Hamiltonian for nearly free, non-relativistic electrons in the presence of an external, uniform electromagnetic field is:

$$H - \frac{1}{2m}(\mathbf{p} - q\mathbf{A})^2 + q\phi, \qquad (5.13)$$

where m is the effective mass, $\mathbf{A}$ is the vector potential and ϕ the scalar potential. Without loss of generality, we can choose the y-axis (z-axis) along the direction of

the electric (magnetic) field. Therefore, the scalar potential can be cast as:

$$\phi(y) = -Ey. \tag{5.14}$$

By choosing the gauge $\mathbf{A} = -B(y, 0, 0)$ and considering particles with charge $q = -e$, Equation (5.13) becomes:

$$H = \frac{1}{2m}\left[p_y^2 + \hbar^2 k_z^2\right] + \frac{1}{2}m\tilde{\omega}_c(y - k_x l_B^2)^2 + eEy, \tag{5.15}$$

with $l_B = \sqrt{\hbar/eB}$ the magnetic length and $\tilde{\omega}_c = eB/m$ the cyclotron frequency of the non-relativistic system. Equation (5.15) can be rewritten as:

$$H = \frac{1}{2m}\left[p_y^2 + \hbar^2 k_z^2\right] + \frac{1}{2}m\tilde{\omega}_c(y - \varphi_{k_x})^2 + ek_x l_B^2 E - \frac{m}{2}v_d^2 \tag{5.16}$$

where we have introduced $\varphi_{k_x} = k_x l_B^2 - v_d/\tilde{\omega}_c$ and the drift velocity $v_d = E/B$. The resulting expression is the Hamiltonian of a quantum harmonic oscillator centered around the coordinate φ_{k_x}, where the spectrum has been shifted by the effect of the electric field. The energy levels are given by:

$$\epsilon_n = \hbar\tilde{\omega}_c\left(n + \frac{1}{2}\right) + \frac{\hbar^2 k_z^2}{2m} + e\varphi_{k_x}E + \frac{m}{2}v_d^2 \qquad n = 0, 1, 2, \ldots \tag{5.17}$$

Apart from a rigid shift of the bands, the electric field gives rise to a linear dependent term on k_x, as shown in Figure 5.2. The spectrum is organized in evenly spaced bands that disperse linearly in momentum k_x. The eigenfunctions are still given by the harmonic oscillator solution

$$\psi_n(\mathbf{r}) = \frac{e^{ik_x x}e^{ik_z z}}{\sqrt{L_x L_z}}\frac{1}{\sqrt{2^n n!\pi^{1/2} l_B}}e^{-(y-\varphi_{k_x})^2/l_B^2}H_n\left[\frac{y - \varphi_{k_x}}{l_B}\right], \tag{5.18}$$

but now the equilibrium position is centered at $k_x l_B^2 - v_d/\tilde{\omega}_c$.

5.2.2 Hall regime in Dirac and Weyl semimetals

As mentioned in chapter 1, the Dirac equation splits into two equations (choosing the Weyl representation for the matrices) in the massless case, with the wave-functions representing Weyl fermions of opposite chirality. Around a single Weyl node, the Weyl semimetal is a Lorentz invariant system with the velocity of light being replaced by the Fermi velocity v_F. The minimal low-energy model characterizing a Dirac

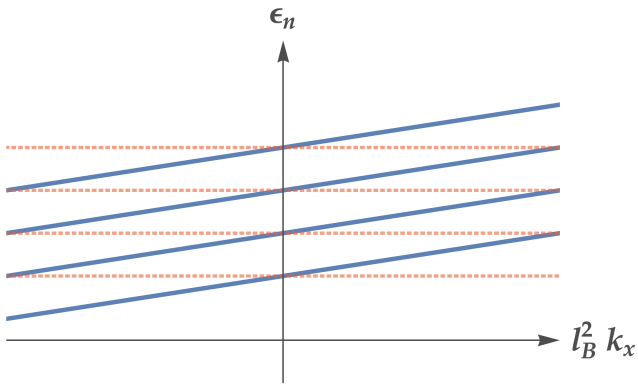

FIGURE 5.2: Schematic representation of the energy dispersion of Landau levels in the presence of an electric field **E** (solid lines) and without the electric field (dotted lines) for $k_z = 0$. The former levels are not flat but disperse linearly as a function of the conserved momentum k_x.

material in the presence of uniform electric and magnetic fields is:

$$\mathcal{L} = i\hbar\bar{\psi}\gamma^\mu \left(\partial_\mu + i\frac{q}{\hbar}A_\mu\right)\psi, \tag{5.19}$$

where $x^0 = t/v_\mathrm{F}$, $x^i = \mathbf{r}$, $A_0 = \phi/v_\mathrm{F}$, $A^i = \mathbf{A}$, $q = -e$ and γ^μ are the Dirac matrices in the Weyl representation. The covariant structure of Equation (5.19) permits to solve the problem exactly; as we see in section 5.1.1, a boost in the direction perpendicular to **E** and **B** with the appropriate velocity leads to a reference frame where the electric field **E**′ vanishes. Therefore, the spectrum of a Weyl semimetal in perpendicular **E** and **B** fields can be obtained by solving the problem in the primed frame (with magnetic field **B**′) and boosting back to the original coordinate system.

We choose the Landau gauge $\mathbf{A} = -B(y, 0, 0)$ and the scalar potential $\phi = -Ey$ to represent a uniform magnetic and electric field pointing in the z- and y-directions, respectively. Since k_z is a good quantum number, the system can be treated as a collection of 2D Dirac layers in perpendicular **E** and **B** fields.

If the system satisfies the condition $v_\mathrm{F}B \geq E$, we can always move to a reference frame where the electric field vanishes. Under a boost in the x-direction with velocity

v, the vector fields **E** and **B** transform as:

$$E'_y = \gamma(E_y - vB_z) \tag{5.20}$$
$$B'_z = \gamma(B_z - v/v_F^2 E_y), \tag{5.21}$$

as it was described in Equations (5.11) and (5.12). When the parameter v coincides with the drift velocity $v_d = E/B$, the second observer experiences only a reduced magnetic field of magnitude $B'_z = [1-\beta^2]^{1/2}B_z$, where $\beta = v_d/v_F$. The energy spectrum of the primed system in the presence of a magnetic field has already been discussed in Equation (2.28) and is given by:

$$\epsilon'_n = \text{sign}(n)\sqrt{\hbar^2\omega_c'^2|n| + v_F^2\hbar^2k_z^2} \qquad n \in \mathbb{Z}, m \neq 0$$
$$\epsilon'_0 = -\text{s}v_F\hbar k_z, \tag{5.22}$$

where $\omega_c = \sqrt{2}v_F eB/\hbar$ is the cyclotron frequency for Dirac systems. To recover the spectrum in the original frame, we have to apply the inverse boost transformation to the energy-momentum quadrivector P^μ, whose zeroth component represents the energy of the system:

$$P^\mu = \begin{pmatrix} E/v_F \\ \mathbf{p} \end{pmatrix}. \tag{5.23}$$

Applying the inverse transformation $P^\mu = (\Lambda^{-1})^\mu{}_\nu P'^\nu$, the spectrum in the original coordinate system reads:

$$\epsilon = \sqrt{1-\beta^2}\epsilon' + v_F\hbar\beta k_x. \tag{5.24}$$

Substituting the primed energies into Equation (5.24), the final expression is:

$$\epsilon_n = \text{sign}(n)\sqrt{\hbar^2\omega_c^2(1-\beta^2)^{3/2}|n| + v_F^2\hbar^2k_z^2(1-\beta^2)} + v_F\hbar\beta k_x$$
$$\epsilon_0 = -\text{s}v_F\hbar k_z\sqrt{1-\beta^2} + v_F\hbar\beta k_x. \tag{5.25}$$

In contrast to non-relativistic electrons, where the only effect of the electric field was a rigid displacement of the dispersing levels, Dirac materials (including graphene [274, 275]) present a non-trivial dependence of the cyclotron frequency with the electric field. The Landau level spacing scales with the electric field as $(1-\beta^2)^{3/2}$, whereas the spectrum is quantized in equally spaced levels in the non-relativistic case. The evolution of the cyclotron frequency with the applied electric field is shown in Figure 5.3. From Equation (5.25) one concludes that when the electric field reaches the critical value $E = v_F B$ (which amounts to $\beta = 1$), all the Landau levels collapse to a single, linearly dependent band:

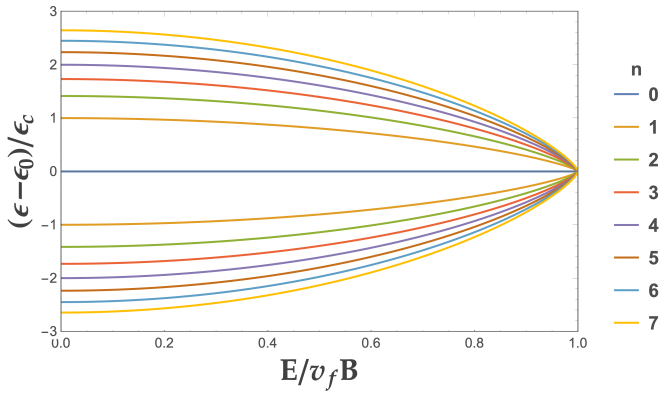

FIGURE 5.3: Evolution of the Landau level spectrum with the applied electric field for $k_z = 0$. As can be see, all Landau levels collapse to a single band $\epsilon_n = \epsilon_0 = v_d \hbar k_x$ for the critical value $E = v_F B$. ϵ_c is the cyclotron frequency $\hbar\omega_c$.

$$\lim_{\beta \to 1} \epsilon_n = v_d \hbar k_x \tag{5.26}$$

The collapse described in this section is different from the overlap of Landau levels occurring in a non-relativistic electron gas [282] due to a broadening of the level spacing on increasing the electric field, filling the gaps between adjacent states. It is a characteristic of the Dirac matter that will take place not only in Weyl but also in Dirac semimetals. Although indications of collapse of Landau levels have been reported experimentally in graphene structures [283, 284], at the time of writing, we do not know of similar attempts in 3D samples.

5.2.3 Magnetic and electric regimes

A comment on the applicability of the boost transformation is in order. The dispersion relation described in Equation (5.25) has been calculated by moving to a frame of reference where the electric field vanishes. One can always perform such transformation provided that $v_F B \geq E$, which amounts to the condition $\beta = v_d/v_F \leq 1$, where the Fermi velocity replaces the speed of light c. The interpretation of this requirement is simple: the relative velocity of an inertial frame cannot exceed the speed of light.

One may naturally wonder what occurs when the magnitude of the electric field is beyond this limit. In this regime we cannot apply the aforementioned transformation (we would get $\beta = v_d/v_F > 1$), but one can find a Lorentz transformation to

a coordinate system where the magnetic field vanishes [278], as illustrated in Equation (5.12). This limit is known as *electric regime*, where the electronic orbits are open trajectories (hyperbola) and the spectrum ceases to be quantized. Below the critical value we are in the *magnetic regime*, characterized by closed orbits where the transformation applied in section 5.2.2 remains valid. As we increase the electric field, the area of these closed trajectories increases, squeezing the level spacing between bands. At the critical value the area becomes infinite, collapsing the Landau levels.

5.3 Collapse of strain-induced Landau levels

In this section, we will review the relation between lattice deformations and electromagnetic fields and explore the collapse of the strain-induced Landau levels in particular strain configurations due to the deformation potentials.

As explained in chapter 4, elastic deformations that change slowly on the lattice scale are parametrized by the tensor $\hat{u}_{ij} = \partial_j u_i$, a function of the displacement vector $\mathbf{u}$. With the help of symmetry arguments, we were able to characterize the smooth variations of the distance between Weyl nodes as gauge fields, $A_i = \hat{u}_{ij} b^j$.

In addition to the vector $\mathbf{A}$, another important electron-phonon coupling in elasticity theory is the deformation potential $\Phi = \mathrm{Tr}[u_{ij}]$. Given an infinitesimal volume element $\mathrm{d}V$, the elements of length $\mathrm{d}x_i$ along the principal axes of the symmetric strain tensor $u_{ij} = \hat{u}_{[i,j]}$ become, after the deformation, $\mathrm{d}x_i' = (1 + u_{ii})\mathrm{d}x_i$ [243]. Ignoring higher-order terms, the resulting volume is proportional to the trace of the strain tensor:

$$\mathrm{d}V' = (1 + u_{11} + u_{22} + u_{33})\mathrm{d}V. \tag{5.27}$$

The deformation potential is a scalar field that couples to the electron density in the effective Hamiltonian. As discussed in chapter 4, it is of the same order as the elastic gauge field in a derivative expansion. Volume changes in the unit-cell volume have significant consequences on the local electronic densities, leading to variations in the chemical potential and shifts in the energy bands [8].

Considering the simplest platform of two Weyl nodes separated in momentum space, the low-energy description around one of the Weyl cones coupled to the lattice deformations is:

$$H_{\mathrm{s}} = \mathrm{s} v_{\mathrm{F}} \sigma^i (p_i + \mathrm{s} c A_i) + g \Phi \mathbb{I}, \tag{5.28}$$

where Φ is the strain-induced scalar potential and g and c are material-dependent coupling constants. The dimensionless Grüneisen parameter c is typically of order 1 in most materials [285, 286]. In what follows, we set $c = 1$ and remove it from the discussion. The deformation potential couples as a scalar field that can generate,

under non-uniform deformations, a strain-induced electric vector $\mathbf{E}_{\text{el}} = -g/e\,\boldsymbol{\nabla}\Phi(\mathbf{r})$. Likewise, elastic gauge fields give rise to pseudo-magnetic fields $\mathbf{B}_{\text{el}} = \hbar/e\,\boldsymbol{\nabla}\times\mathbf{A}(\mathbf{r})$.

As an illustrative example, we assume a Weyl semimetal with two Weyl nodes separated a distance $2b$ in the x-direction. A space dependent uniaxial configuration such that

$$u_{xx} = -\frac{e}{\hbar}\frac{By}{b} \tag{5.29}$$

$$u_{yy} = y_{zz} = 0, \tag{5.30}$$

will give rise to an elastic vector potential $\mathbf{A} = -e/\hbar\, B(y,0,0)$. This term describes a uniform pseudo-magnetic field of magnitude B in the z-direction that quantizes the spectrum into Landau levels. Simultaneously, a scalar potential originates from the strain configuration $\Phi = -\frac{e}{\hbar}\frac{yB}{b}$, inducing an electric field $E = \frac{g}{\hbar}\frac{B}{b}$ along the y-direction. This scenario mimics the situation discussed in section 5.2.2; the electric field introduces a non-trivial dependence on ω_c and the spectrum is given by Equation (5.25). The condition for the collapse $E \geq v_{\text{F}}B$ translates into a constraint on the values of the coupling constant associated with the deformation potential:

$$g \geq \hbar v_{\text{F}}\, b. \tag{5.31}$$

Interestingly, the constraint on the coupling g is independent of the strength of the deformation, being solely a function of the intrinsic parameters of the material. Although there are not yet measurements of the electron-phonon couplings in Weyl semimetals, using reasonable values we see that the condition will be easily attainable in different samples[6]. For instance, the separation between nodes is estimated to be $b \approx 0.08$ Å^{-1} in Weyl semimetal TaAs, with the Fermi velocity $v_{\text{F}} \sim 1.3\times10^5$ m/s [287]. These values give a lower bound for the elastic coupling constant of $g \geq 0.07$ eV, meaning that the samples will be typically affected by the effect described above[7]. The estimated value in graphene structures (taking screening into account) is of the order of 4 eV. Thin films of Weyl semimetals, more suitable for straintronics, are not expected to be as deformable as their 2D counterpart, but the required value is much smaller.

[6]The numerical values used for this calculation have been obtained from Refs. [287, 288]. Applying these parameters, one notices that the resulting condition for the collapse of the Landau levels returns feasible values for the coupling constant.

[7]At the time of writing, Weyl semimetal RhSi displays the largest momentum separation of chiral fermions, $b = 2.33$ Å^{-1} [288]. Assuming a Fermi velocity similar to the one of TaAs, the lower bound for the coupling constant of this material reads $g \geq 2.42$ eV.

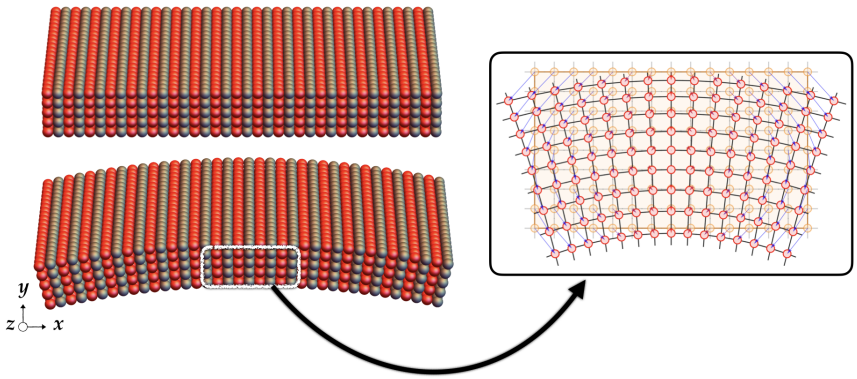

FIGURE 5.4: Schematic representation of the proposed setup. Films of Weyl semimetal organized in a rectangular geometry. The external deformation bends the original system into a circular arc in the $x - y$ plane. This configuration is able to induce both pseudo-magnetic and pseudo-electric fields, the pseudo-Landau level spectrum collapsing when the critical value is reached. Adapted from Ref. [166].

5.3.1 Particular strain proposals. Discussion on possible experimental setups

Other strain configurations will also be affected by this phenomenon, which is particularly relevant for a correct interpretation of the experiments [239]. The best experimentally accessible devices will be obtained by bending thin films of Weyl semimetals, a generalization of the strain configuration first suggested in Ref. [252] for graphene sheets. The physical consequences of pseudo-magnetic fields with realistic strain configurations on Dirac and Weyl semimetals were considered in Refs. [165, 166]. In what follows, we will study the effect of the deformatnion potential on the physics analyzed in these works.

As mentioned in chapter 4, films and wires realizations of Dirac matter are excellent devices to test strain-induced phenomena. We consider a cubic lattice model (the system can be thought as a collection of rectangular staggered layers) where the coordinates are fixed with respect to the parameter $\mathbf{b}$ in such a way that the Weyl nodes are separated a distance $2b$ in the x-direction. Normal forces are applied at the boundaries of the crystal along the x-axis as sketched in Figure 5.4,

leading to a stretching geometry characterized by the deformation:

$$\begin{aligned} u^x &= u_0(2xy + Cx) \\ u^y &= u_0\left[-x^2 - Dy(y + C)\right] \\ u^z &= 0, \end{aligned} \tag{5.32}$$

where u_0 and D are constants that depend on the intrinsic properties of the material; u_0 defines the maximum stress and D is a relation between the Lamé coefficients. C parametrizes a family of deformations giving rise to the same pseudo-magnetic field. The strain configuration described in Equation (5.32) induces a non-uniform elastic gauge field

$$\begin{aligned} A_x &= \hat{u}_{xx} b^x = u_0(2y + C)b \\ A_y &= \hat{u}_{yx} b^x = -2u_0 x b \\ A_z &= 0, \end{aligned} \tag{5.33}$$

that mimics a uniform magnetic field $\mathbf{B} = -\hbar/e\, 4u_o b\, \hat{\mathbf{z}}$ able to create energy gaps in the spectrum. In addition to the pseudo-magnetic field, this bending configuration also contains a dilatation that produces a deformation potential

$$\Phi(\mathbf{r}) = u_0(1 - D)(2y + C) \tag{5.34}$$

equivalent to a constant electric field $\mathbf{E} = -g/e\, 2u_0(1 - D)\, \hat{\mathbf{y}}$ perpendicular to the magnetic field. As in the above example, the collapse of the pseudo-Landau levels is translated into a restriction for the values of the coupling constant g:

$$g \geq 2\hbar \frac{v_F b}{1 - D}. \tag{5.35}$$

For thin films of Cd_3As_2 such as the one suggested in Ref. [165], a coupling constant $g \geq 0.32$ eV would be enough to collapse the predicted oscillations.

5.3.2 Antisymmetric contributions to the deformation potential

Being proportional to the trace of the strain tensor, deformations conserving the volume of the sample will not generate a deformation potential stemming from the strain tensor u_{ij}. This is the case, for example, of the torsional strain discussed in Ref. [165] or the tetra-axial strain in the diamond lattice of Ref. [289]. Nevertheless, these configurations are still able to generate elastic electric fields by virtue of the vorticity vector $\mathbf{\Omega} = \nabla \times \mathbf{u}$. As mentioned in chapter 4, the antisymmetric components of the deformation tensor (related to changes in the relative orientation of the orbitals)

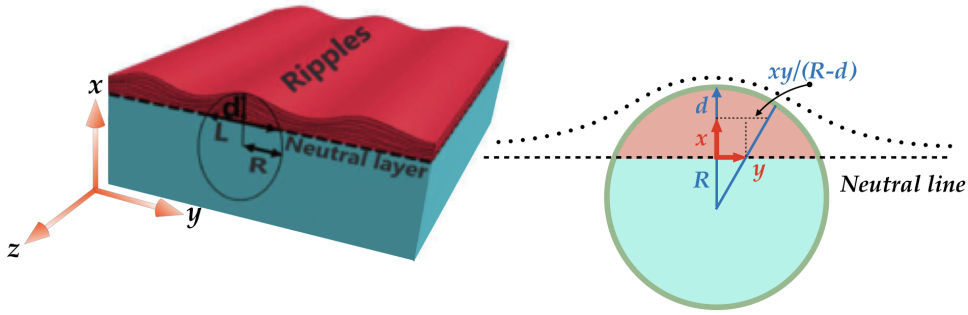

FIGURE 5.5: Schematic description of the geometry used to characterize the ripples. Ripples (black dotted line) with length d protrudes over the neutral surface. The curvature gives rise to a displacement vector $\mathbf{u} = xy/(R-d)$ along the y-direction, where x and y are the displacements in the corresponding axes. Adapted from Ref. [239].

give rise to a scalar term ξ in the Hamiltonian unrelated to volume changes. This term, proportional to the product of the vorticity vector and the intrinsic separation between nodes, $\xi = \mathbf{\Omega} \cdot \mathbf{b}$, provides a rotational contribution to the electric vector $\mathbf{E}_{\text{el}} = -\lambda/e\mathbf{\nabla}\xi(\mathbf{r})$, where λ is the coupling constant parameter associated to the rotational deformation. For the configurations discussed so far in this chapter, either the product $\mathbf{\Omega} \cdot \mathbf{b}$ is zero (such is the case of the bending strain discussed in Ref. [252] and the tetra-axial strain [289]) or the induced fields are parallel (torsional deformation [165]).

In a recent experimental work, the emergence of a pseudo-magnetic field and the quantization of the spectrum into Landau levels on the doped Weyl semimetal $Re - MoTe_2$ was shown [239]. Landau levels were observed in the strained domains where the lattice deformations induce the formation of topographic modulations (ripples) on the surface of the sample (see Figure 5.1).

Following the arguments of section 5.3, it is possible to reproduce the conditions that induce the collapse of the Landau spectra with an electric field generated from the antisymmetric strain. The modulations on the surface introduce a displacement vector $\mathbf{u} = xy/(R-d)\,\hat{\mathbf{y}}$, where d is the length of the ripple from the neutral surface and R is the radius (see the schematic representation of the setup in Figure 5.5). The location of the Weyl points in this system is given by the vector $\mathbf{b} \approx 2\pi/a_x\,(0, 0.18, 0.17)$. Following the low-energy description, this deformation generates the elastic gauge fields

$$
\begin{aligned}
A_x &= 0 \\
A_y &= \hat{u}_{yy} b^y = \left(\frac{x}{R-d}\right) b_y \\
A_z &= 0,
\end{aligned}
\tag{5.36}
$$

that give rise to an effective magnetic field

$$
\mathbf{B} = \frac{\hbar}{e} \frac{b_y}{R-d} \hat{\mathbf{z}}. \tag{5.37}
$$

Additionally, the corrugations induce a perpendicular electric field

$$
\mathbf{E} = -\frac{\lambda}{e} \frac{b_z}{R-d} \hat{\mathbf{y}}, \tag{5.38}
$$

originated from the vorticity vector $\mathbf{\Omega} = y/(R-d)\,\hat{\mathbf{z}}$. The critical value $E = v_F B$ is again translated into a constraint on the elastic coupling constants:

$$
\lambda \geq v_F \hbar \frac{b_y}{b_z}. \tag{5.39}
$$

The condition expressed in Equation (5.39) does not depend on the separation distance of the nodes ($b_y \sim b_z$), but it is given solely by the Fermi velocity. The trace of the strain tensor gives an additional electric field pointing in the x-direction:

$$
\mathbf{E} = -\frac{g}{e} \frac{1}{R-d} \hat{\mathbf{x}}. \tag{5.40}
$$

Applying a similar boost in the y-direction, we arrive to the usual condition

$$
g \geq v_F \hbar\, b_y. \tag{5.41}
$$

5.4 Conclusions and discussions

In this chapter we have analyzed the spectrum of Weyl semimetals in the presence of a perpendicular electric and magnetic field. Motivated by the recognition that, in Dirac materials, the presence of a critical electric field (perpendicular to the magnetic vector) induces a collapse of the Landau levels to a single band, we have extended this analysis to the case of strained Weyl semimetals. Strain geometries leading to uniform pseudo-magnetic fields generate, simultaneously, uniform strain-induced electric fields that fulfill the condition for the Landau levels collapse.

Although there are further proposals leading to uniform magnetic fields, the results shown in this chapter suggest that the condition for the collapse of the

pseudo-Landau levels will be translated into a constraint on the coupling constants determined solely by the intrinsic parameters of the material (the Fermi velocity and the separation between the chiral points), independently of the geometry and strength of the deformation.

The results shown in this chapter will also affect the estimation of the pseudo-magnetic fields induced by strain. The level spacing, which is used to measure the magnitude of the induced magnetic field, changes with the value of the deformation potential, as illustrated in Figure 5.3. This can lead to a spread of values when the magnetic field is evaluated for different points and samples [163, 276]. Thus, this phenomena should be considered for a correct understanding of STM images of strained Dirac materials and similar 3D topological insulators [290].

This work can be extended to situations involving more general materials. In particular, most of the actual Weyl semimetals are inversion broken, meaning that the chiral Weyl points are separated in energy by the zeroth component of the vector b^μ. In a recent publication [162] was shown that this zeroth component will be affected by elastic deformations, developing a time component of the elastic gauge field. This gives rise to a pseudo-electric field that, in contrast to the one associated with the scalar potential discussed in this chapter, will be axial, coupling with opposite sign to the two chiralities. The addition of the two terms can lead to interesting situations where the chiral imbalance is maximized by making the total scalar potential zero in one of the nodes. Dirac semimetals have been a subject of intense experimental research in this topic, magnetoresistance measures being used as experimental evidence of the chiral magnetic effect. Even though these materials have the nodes located at high symmetry points of the lattice, strain will still induce a deformation potential that will affect the spectrum of the system in real (and elastic as suggested in Ref. [171]) magnetic fields.

On the other hand, there are still open questions regarding the tilt parameter and the optical properties of Type-II Weyl semimetals. The former has been shown to play an equivalent role of an electric field in Dirac materials, giving rise to a collapse of the spectrum for Type-II Weyl nodes as a function of the angle between the magnetic field and the tilt parameter, regardless of the strength of the magnetic field [259, 258]. Since the tilt parameter is affected by the lattice distortions, it would be interesting to study the effect of strain on the transitions between the electric and magnetic regimes. From a theoretical point of view, it could be possible to generate this type of phase transitions by tailoring the magnitude of the tilt parameter and its orientation with the magnetic field, making it feasible to induce a collapse of the Landau levels in a Type-I Weyl semimetal [258].

Chapter 6

Conclusions

Dirac matter has become an essential element in modern condensed matter theory. The realization of Dirac particles in solid-state materials has not only brought novel fundamental phenomena, but also has contributed to the exchange of concepts and methods between different fields of physics. The findings in this thesis contribute to the understanding and development of two interesting topics in Dirac matter physics; anomaly-induced transport phenomena and the interplay of lattice deformations and the electronic properties of the system.

In the first part of this thesis we have focused on the unconventional thermal properties of Dirac materials. Both the finite thermoelectric coefficient at zero temperature and the resulting violation of the Mott relation at the conformal limit are anomaly-related transport phenomena characteristic of these physical systems. Violation of the phenomenological relations has been known to occur for a long time in materials where long-range Coulomb interactions are the fastest time scale. However, our results are independent of interaction mechanisms, lying on the low-energy effective structure of Dirac electrons.

The second general topic discussed in this thesis involves the interplay between mechanical and electronic properties in Dirac and Weyl semimetals. The electronic properties of the low-energy excitations are intimately related to the lattice structure of Dirac materials. We have used a symmetry approach to construct the general effective action describing the various electron-phonon couplings. An interesting contribution to this field has been the recognition that deformations affecting the relative orientation between atomic positions lead to effective interactions absent in two-dimensional materials. These new results enrich the possibilities of tailoring the electronic excitations by means of lattice distortions. Remarkably, the vorticity vector induces a deformation potential in volume preserving deformations.

We have also considered the collapse of the Landau level spectrum under the influence of perpendicular electric and magnetic fields (both fictitious and real). We have strained the analogy between real and elastic fields and showed that certain strain geometries generating uniform magnetic fields will induce, simultaneously, an electric field able to destroy the quantized structure of the system due to the same process occurring with real fields. The condition for collapse is translated into a constraint of the coupling parameters, independently of the strength of the deformation.

We conclude this thesis by discussing the promising expectations of current findings in the research field of topological Dirac and Weyl semimetals. Dirac materials not only provide a fruitful basis for the discovery of novel, unconventional physical phenomena, but they also possess non-trivial topological properties that open exciting new pathways to circumvent the current limitations of conventional materials. We firmly believe that topological systems will continue being one of the most inspiring research lines, and will also profoundly influence and complement our future technologies.

We would like to finally make a remark on the relevant role played by these materials in giving new insights into our academic approach. In the current times, where the different physical fields are increasingly specialized, the gap among the different disciplines has become wider, and the subject has begun to loose its unity. Examples as those exposed throughout this thesis have special relevance nowadays. The models presented belong to an unified framework where the Dirac equation lies at the center of the theory, allowing to describe different phenomena with the same language. This establishes robust connections with seemingly unrelated areas of physics, from condensed matter and the study of crystalline structures to the fundamental level of high energy physics and topological spaces. Dirac materials have provided an accessible door to test high energy processes in crystalline structures, proving that the laws of physics are not intrinsically related to the scale of the system, but they should rather be considered in a more universal perspective. It is necessary to reformulate our approach and start a new scientific culture with new and proper questions, encouraging an interdisciplinary research activity to reach a robust development in science.

Chapter 7

Conclusiones

Los materiales de Dirac se han convertido en una pieza fundamental en la teoría moderna de la materia condensada. La realización de partículas de Dirac en sistemas de materia condensada no sólo ha traído nuevos fenómenos fundamentales, sino que también ha contribuido al intercambio de conceptos y métodos entre diferentes campos de la física. Los resultados de esta tesis contribuyen a la comprensión y desarrollo de dos temas interesantes en la física de la materia de Dirac; fenómenos de transporte inducidos por anomalías y la interacción entre las deformaciones de la red y las propiedades electrónicas del sistema.

En la primera parte de esta tesis nos hemos centrado en las propiedades térmicas no convencionales de los materiales de Dirac. Tanto el coeficiente termoeléctrico finito a temperatura cero como la violación de la relación de Mott en el límite conforme son fenómenos de transporte relacionados con las anomalías característicos de estos sistemas. Es ampliamente conocido que las relaciones fenomenológicas no se satisfacen en materiales donde las interacciones de Coulomb de largo alcance son la escala de tiempo más rápida. No obstante, nuestros resultados son independientes de estos mecanismos de interacción, ya que se basan en la estructura de baja energía de los electrones de Dirac.

El segundo problema general del que trata la tesis está relacionado con la interacción entre las propiedades mecánicas y electrónicas de los semimetales de Dirac y Weyl. Las propiedades electrónicas de las excitaciones de baja energía están íntimamente relacionadas con la estructura de la red de los materiales de Dirac. Hemos utilizado un enfoque simétrico para construir una acción efectiva general que describe los diversos acoplos electrón-fonón. Una contribución interesante a este campo ha sido el observar que las deformaciones que afectan la orientación relativa entre las posiciones atómicas dan lugar a interacciones efectivas ausentes en

materiales bidimensionales. Estos nuevos resultados enriquecen las posibilidades de modificar las excitaciones electrónicas a través de las deformaciones de la red. Notablemente, el vector de vorticidad genera un potencial de deformación en aquellas configuraciones que preservan el volumen del sistema.

Finalmente, hemos considerado el colapso de los niveles de Landau bajo la influencia de campos eléctricos y magnéticos perpendiculares (tanto ficticios como reales). Usando la analogía entre los campos reales y elásticos, hemos demostrado que ciertas configuraciones de deformación que dan lugar a campos magnéticos uniformes producen, simultáneamente, campos eléctricos capaces de eliminar la estructura cuantizada del sistema mediante el mismo mecanismo visto en campos reales. La condición del colapso se traduce en una restricción de los parámetros de acoplo, independientemente de la fuerza de la deformación.

Los materiales de Dirac no sólo ofrecen una base fructífera para el descubrimiento de nuevos fenómenos físicos, sino que también poseen propiedades topológicas no triviales que abren nuevas vías para sortear las limitaciones actuales de los materiales convencionales. Creemos firmemente que los sistemas topológicos continuarán siendo una de las líneas de investigación más estimulantes e influirán profundamente en nuestros sistemas tecnológicos futuros.

Finalmente, nos gustaría destacar el papel relevante que juegan estos materiales a la hora de proporcionar nuevos puntos de vista a nuestro enfoque académico. Actualmente, los diferentes campos de la física están cada vez más especializados. La brecha entre las diferentes disciplinas es cada vez mayor, y el área ha comenzado a perder su unidad. Los ejemplos expuestos a lo largo de la tesis resultan actualmente de gran importancia. Todos los modelos presentados pertenecen a un gran marco unificado cuyo nexo es la ecuación de Dirac, lo que permite describir fenómenos totalmente diferentes con el mismo lenguaje. Esta unión establece conexiones robustas entre áreas de la física aparentemente no relacionadas, desde el campo de la materia condensada y el estudio de redes cristalinas, hasta el nivel fundamental de la física de altas energías y espacios topológicos. En este sentido, los materiales de Dirac han proporcionado una vía accesible para experimentar fenómenos de altas energías en estructuras cristalinas, demostrando que las leyes de la física no están intrínsecamente relacionadas con la escala del sistema, sino que deben considerarse desde una perspectiva más universal. Es necesario reformular nuestro enfoque y comenzar una nueva cultura científica con nuevas y apropiadas preguntas, fomentando una carrera investigadora interdisciplinar para alcanzar un robusto desarrollo de la ciencia.

Appendix A

Topological aspects of crystalline lattices. Berry phase

In this appendix we review some basic concepts related to the topological character of solid-state materials. The specific case of a Weyl node will be studied in detail.

A.1 Berry phase on crystalline solids

The topological nature of a crystalline lattice is captured by the Bloch state vectors $|u_n(\mathbf{k})\rangle$, where n labels the index band, and the Berry phase γ_n. In crystalline solids, the Berry phase is computed from the $\mathbf{k}$-dependent Hamiltonian $H(\mathbf{k})$, which is obtained after performing a unitary operation $H(\mathbf{k}) = \exp(-i\mathbf{kr})\, H(\mathbf{p})\, \exp(i\mathbf{kr})$, and their wave-functions $|u_n(\mathbf{k})\rangle$. A quantum state $|u_n(\mathbf{k})\rangle$ is defined up to an arbitrary complex phase, and cannot be distinguished from $\lambda|u_n(\mathbf{k})\rangle$, with $\lambda = e^{i\alpha}$. The latter corresponds to the equivalence class

$$[|u_n(\mathbf{k})\rangle] = \{\lambda|u_n(\mathbf{k})\rangle \mid \lambda \in U(1)\}, \tag{A.1}$$

where the vectors from the ray are normalized. Therefore, at each point of the Brillouin zone there is a complex vector space or fiber $\mathcal{V}_{n,\mathbf{k}}$ whose vectors $|u_n(\mathbf{k})\rangle \in \mathcal{V}_{n,\mathbf{k}}$ satisfy the relation $H(\mathbf{k})|u_n(\mathbf{k})\rangle = E_n(\mathbf{k})|u_n(\mathbf{k})\rangle$. We can study the variation of the fiber $\mathcal{V}_{n,\mathbf{k}}$ in the reciprocal space by selecting an arbitrary element $|u_n(\mathbf{k})\rangle$ at a given point and parallel transport it along a continuous path $\mathbf{k}(s)$, as indicated in

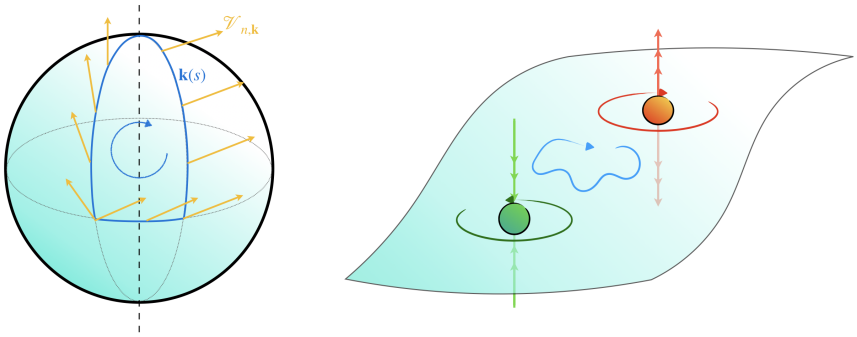

FIGURE A.1: *(Left)*: Schematic representation of the variation of the fiber $\mathcal{V}_{n,\mathbf{k}}$ along the continuous path $\mathbf{k}(s)$ in the reciprocal space. If the topological space has a non-trivial curvature, the state will acquire a phase γ_n proportional to the connection $\mathcal{A}_n(\mathbf{k})$. *(Right)*: Degeneracy points must be excluded when defining the topological space. Closed path surrounding those singularities cannot be continuously deformed.

Figure A.1. The parallel transport condition is formally written as [50]:

$$\left\langle u_n(\mathbf{k}) \middle| \frac{\partial}{\partial \mathbf{k}(s)} u_n(\mathbf{k}) \right\rangle = 0. \tag{A.2}$$

Equation (A.2) defines a *connection* $\mathcal{A}_n(\mathbf{k})$ in the bundle structure [96, 50, 291]. This connection is explicitly given by the vector:

$$\mathcal{A}_n(\mathbf{k}) = -i\langle u_n(\mathbf{k}) | \nabla_{\mathbf{k}} u_n(\mathbf{k}) \rangle. \tag{A.3}$$

If the variation is performed along a closed path C, the vector $|u_n(\mathbf{k})\rangle$ acquires a geometrical phase

$$\gamma_n = \oint_C \mathrm{d}\mathbf{k}\, \mathcal{A}_n(\mathbf{k}). \tag{A.4}$$

Berry introduced his now eponymous Berry phase in 1983 after asking which phase factor would acquire an eigenstate that has been adiabatically transported around a closed path in the parameter space [62]. Later, Simon provided in his work [291] a topological significance to this phase and manifested its relation with the integer values of the quantum Hall effect introduced by Thouless *et al.* [54].

The connection $\mathcal{A}_n(\mathbf{k})$ defined on the complex bundle is similar to an abelian gauge field. The field strength of the Berry connection,

$$\mathcal{F}_n(\mathbf{k}) = -i\nabla_{\mathbf{k}} \times \langle u_n(\mathbf{k})|\nabla_{\mathbf{k}} u_n(\mathbf{k})\rangle, \tag{A.5}$$

known as Berry curvature, is manifestly gauge-invariant under a gauge transformation $\mathcal{A}_n(\mathbf{k}) \to \mathcal{A}_n(\mathbf{k}) + \nabla_{\mathbf{k}}\phi(\mathbf{k})$ (with $\phi(\mathbf{k})$ an arbitrary function) and plays the same role as a magnetic field in the reciprocal space. Stoke's theorem allows us to recast the Berry phase in the form:

$$\gamma_n = \int_{\mathcal{S}} \mathrm{d}\mathbf{S}\, \mathcal{F}_n(\mathbf{k}), \tag{A.6}$$

where $\mathcal{S}$ is any surface enclosed by the curved C. The previous result manifests the analogy with electrodynamics, as γ_n is the phase acquired by the wave-function as it moves along a closed path in a region with a magnetic field $\mathcal{F}_n(\mathbf{k})$, similarly to the Aharanov-Bohm [292]. The Berry phase is independent of the chosen path, it being an intrinsic property of the geometry of the band structure. This fact is illustrated when computing the Berry curvature associated to the eigenstates of a degeneracy point. If the closed loop surrounds a band-crossing point, the Berry connection has a non-vanishing curvature. Degeneracy points have a non-trivial topology, as they represent singular points that must be excluded when defining the topological smooth manifold. A path enclosing one of these singularities cannot be continuously deformed into a different one, as they belong to different equivalence classes of homeomorphisms (see Figure A.1). We will see in what follows that the Berry curvature of a Weyl node is singular at the crossing point and has the form of a magnetic monopole in reciprocal space with a quantized value of the Berry flux.

A.2 Berry phase of band-crossing points. Monopoles of Berry curvature

The Berry curvature of a Weyl node can be derived from the general Hamiltonian:

$$H_\chi = \chi \sigma^j k_j, \tag{A.7}$$

where $v_{\mathrm{F}} = 1$ has been assumed for simplicity, and χ is the chirality of the node. Away from the degeneracy points $\mathbf{k}_*$, the Hamiltonian described in Equation (A.7) has two energy values $E_\pm(\mathbf{k})$ with their corresponding eigenvectors $|u_\pm(\mathbf{k})\rangle$. For the conduction and valence band, the eigenfunctions read:

$$|u_-(\theta,\phi)\rangle_{\chi=+1} = \begin{pmatrix} \sin\frac{\theta}{2} \\ -\cos\frac{\theta}{2} e^{i\phi} \end{pmatrix} \qquad |u_-(\theta,\phi)\rangle_{\chi=-1} = \begin{pmatrix} \cos\frac{\theta}{2} \\ +\sin\frac{\theta}{2} e^{i\phi} \end{pmatrix} \tag{A.8}$$

and

$$|u_+(\theta,\phi)\rangle_{\chi=+1} = \begin{pmatrix} \cos\frac{\theta}{2} \\ +\sin\frac{\theta}{2}e^{i\phi} \end{pmatrix} \qquad |u_+(\theta,\phi)\rangle_{\chi=-1} = \begin{pmatrix} \sin\frac{\theta}{2} \\ -\cos\frac{\theta}{2}e^{i\phi} \end{pmatrix} \tag{A.9}$$

where the components of the momentum vectors are expressed in terms of the angles θ, ϕ of the spherical coordinates. Hence, the Berry curvature is:

$$\mathcal{F}_{n,\chi}(k) = \frac{n\chi}{2k^2}\hat{e_k}. \tag{A.10}$$

The Berry curvature has the form of a magnetic monopole. The sign of the monopole is determined by the chirality of the node. Therefore, Weyl points are sources and sinks of Berry curvature [63]. The monopole charge $\mathcal{N}$ is defined as the Berry flux threading a sphere surrounding the Weyl node:

$$\mathcal{N}_{n,\chi} = \frac{1}{2\pi}\int_{\mathcal{S}} \mathrm{d}\mathbf{S}\,\mathcal{F}_{n,\chi}(\mathbf{k}) = n\chi. \tag{A.11}$$

Equation (A.11) proves the strong connection between the stability of the nodes and their topological character: a Weyl node cannot be eliminated unless it merges with an oppositely chiral charge, situation that is realized in the so called Dirac semimetal.

The Nielsen-Ninomiya theorem states that the sum of winding numbers at the points $\mathbf{k}_\alpha$ where the degeneracies are located is always zero [65, 81]. The monopole charge $\mathcal{N}$ is the *winding number* associated with the continuous mapping $\mathbf{k} \to \mathbf{n}(\mathbf{k})$, where $\mathbf{n}(\mathbf{k}) = \mathbf{k}/k$ is the unit vector, from the Brillouin zone to a unit 2-sphere [50]. The winding number $w(\mathcal{S}_\alpha)$ can be expressed as the Berry flux over the sphere $\mathcal{S}_\alpha$ surrounding the point $\mathbf{k}_\alpha$ where the mapping is ill-defined, definition that results identical to the integral formula of the monopole charge defined earlier in Equation (A.11). In this way, the winding number at each linear band-crossing points is equal to the chirality of the node, $w(\mathcal{S}_\alpha) = \chi$. The Nielsen-Ninomiya theorem implies that the sum over chiral charges must vanish, meaning that the number of positive and negative chiral gapless modes in the parameter space must be equal. Therefore, band-crossing points always come in pairs of opposite chirality.

The topological objects defined over this appendix have been studied for the particular case of crystalline lattices. Nevertheless, their geometrical significance is beyond this particular case, and they can be immediately extended to other topological manifolds by simply replacing the crystal momentum by the corresponding parameter.

Appendix B

Thermoelectric coefficient. Result from a Kubo formula

In this appendix we provide details about the calculation of the different linear response coefficients that appeared throughout chapters 2 and 3. First, we will review the derivation of the *exact eigenstates representation*, commonly referred as *Lehmann representation*, for the case of non-interacting electrons. Secondly, we analyze the particular case of thermoelectric tensor and sketch the key steps in order to obtain Equation (2.45), result that will also prove useful for chapter 3.

B.1 Exact eigenstates representation for non-interacting particles

A deeper insight into the structure of the response function described in Equation (2.2) is obtained by expanding the operators in a complete set of eigenstates of the unperturbed Hamiltonian H_0[1]. In the case of non-interacting electrons, a simpler expression may be achieved if the operators are written in terms of single-particle states. For concreteness, consider two operators in the form:

$$\begin{aligned} A(t) &= \sum_{\alpha\beta} A_{\alpha\beta}\, a^{\dagger}_{\alpha}(t) a_{\beta}(t), \\ B(t) &= \sum_{\alpha\beta} B_{\alpha\beta}\, a^{\dagger}_{\alpha}(t) a_{\beta}(t), \end{aligned} \tag{B.1}$$

[1]The discussion will be partially based on the descriptions found in Refs. [176, 49].

where $a_\alpha^\dagger$ (a_β) is the creation (annihilation) operator of single-particle states that diagonalizes the unperturbed Hamiltonian:

$$H_0 = \sum_\alpha E_\alpha \, a_\alpha^\dagger a_\alpha, \tag{B.2}$$

and $A_{\alpha\beta}$, $B_{\alpha\beta}$ are the matrix elements of the single-particle operators A and B, respectively. Our goal is to calculate the expectation value of A in the presence of an external perturbation $F(t)$ that couples linearly to B, i.e., $H_{\text{pert}}(t) = F(t)B$. In this context, the interaction picture emerges as a natural framework to describe such perturbation. Working with this formalism, the time-dependence of the operators a_α reads [49]:

$$\begin{aligned} a_\alpha(t) &= e^{iH_0 t/\hbar} \, a_\alpha \, e^{-iH_0 t/\hbar} = e^{-iE_\alpha t/\hbar} a_\alpha, \\ a_\alpha^\dagger(t) &= e^{iH_0 t/\hbar} \, a_\alpha^\dagger \, e^{-iH_0 t/\hbar} = e^{+iE_\alpha t/\hbar} a_\alpha. \end{aligned} \tag{B.3}$$

Using the identities discussed above, the response function described in Equation (2.2) takes the form:

$$\chi(t) = -\frac{i}{\hbar} \sum_{\alpha\beta\gamma\delta} \int_{-\infty}^{\infty} \mathrm{d}t' \, \Theta(t-t') \, A_{\alpha\beta} B_{\gamma\delta} \, e^{(E_\alpha - E_\beta)t/\hbar} e^{(E_\gamma - E_\delta)t'/\hbar} \left\langle \left[a_\alpha^\dagger a_\beta, a_\gamma^\dagger a_\delta \right] \right\rangle_0 . \tag{B.4}$$

The commutator appearing in Equation (B.4) is solved by making use of the anti-commutation relation of the single-particle operators a_α:

$$\left[a_\alpha^\dagger a_\beta, a_\gamma^\dagger a_\delta \right] = \delta_{\beta\gamma} a_\alpha^\dagger a_\delta - \delta_{\alpha\delta} a_\gamma^\dagger a_\beta. \tag{B.5}$$

After performing its average in the equilibrium ensemble, Equation (B.5) becomes:

$$\left\langle \left[a_\alpha^\dagger a_\beta, a_\gamma^\dagger a_\delta \right] \right\rangle_0 = \left(n_\alpha - n_\beta \right) \delta_{\alpha\delta} \delta_{\beta\gamma}, \tag{B.6}$$

where $n_\alpha = [\exp[\beta(E_\alpha - \mu)] + 1]^{-1}$ is the Fermi distribution function. Substituting Equation (B.6) into Equation (B.4), the linear response function for non-interacting electrons reads:

$$\chi(t) = -\frac{i}{\hbar} \sum_{\alpha\beta} \int_{-\infty}^{\infty} \mathrm{d}t' \, \Theta(t-t') A_{\alpha\beta} B_{\beta\alpha} e^{(E_\alpha - E_\beta)(t-t')/\hbar} \left[n_\alpha - n_\beta \right]. \tag{B.7}$$

Making use of the time invariance, we take the Fourier transform of the above expression. It should be noted that the function presents an oscillatory behaviour at

infinite times. To guarantee the convergence of the time-integrals, it is customary to add a relaxation mechanism in the form of $e^{-\eta(t-t')}$. This mechanism is analogous to consider that the perturbation was adiabatically switched-on at $t = -\infty$. Finally, the linear response function is given by the following expression:

$$\chi(\omega) = \lim_{\eta \to 0^+} \sum_{\alpha\beta} \frac{A_{\alpha\beta} B_{\beta\alpha}}{E_\alpha - E_\beta + \hbar\omega + i\hbar\eta} \left[n_\alpha - n_\beta \right]. \tag{B.8}$$

It is important to stress that Equation (B.8) contains matrix elements computed between single-particle operators and the difference between single-particle energies [176].

B.2 Thermoelectric coefficient. Current and energy-momentum operators

In this section, we detail the calculation of Equation (B.8) for the particular case of the thermoelectric coefficient. As discussed in the main text, when the system is exposed to a magnetic field perpendicular to an applied temperature gradient, it generates a transverse electric current perpendicular to both fields. Considering the model discussed in section 2.3.1 (the z-axis is chosen along the orientation of the magnetic field while the direction of the thermal gradient is taken as the y-axis), the linear response thermoelectric coefficient χ^{xy} is given by:

$$\chi^{xy}(\mathbf{q}, \omega) = \frac{(2\pi)^3}{\mathcal{V}} \int_{-\infty}^{\infty} \mathrm{d}t e^{i\omega(t-t')} \int_{-\infty}^{t'} \mathrm{d}t'' - i v_{\mathrm{F}} \Theta(t - t') \langle \left[J^x(\mathbf{q}, t), T^{0y}(-\mathbf{q}, t'') \right] \rangle, \tag{B.9}$$

where the current and energy-momentum operators are written as:

$$J^x(\mathbf{r}, t) = e s v_{\mathrm{F}} \Psi^\dagger(\mathbf{r}, t)\, \sigma^x\, \Psi(\mathbf{r}, t), \tag{B.10}$$

$$T^{0y}(\mathbf{r}, t) = \frac{-i\hbar}{2} \left[v_{\mathrm{F}} \Psi^\dagger(\mathbf{r}, t)\, \mathbb{I} \overleftrightarrow{\partial_y}\, \Psi(\mathbf{r}, t) - s \Psi^\dagger(\mathbf{r}, t)\, \sigma^y \overleftrightarrow{\partial_0}\, \Psi(\mathbf{r}, t) \right]. \tag{B.11}$$

As mentioned in the previous section, within the exact eigenstates representation the matrix elements are computed between the single-particle states φ that

diagonalize the unperturbed Hamiltonian[2]:

$$J^x(\mathbf{q},t) = \sum_{\mathbf{k}m,\mathbf{l}n} j^x_{\mathbf{k}m,\mathbf{l}n}(\mathbf{q})\, a^\dagger_{\mathbf{k}m}(t)\, a_{\mathbf{l}n}(t) \tag{B.12}$$

and

$$T^{0y}(-\mathbf{q},t'') = \sum_{\boldsymbol{\kappa}\mu,\boldsymbol{\lambda}\nu} t^{0y}_{\boldsymbol{\kappa}\mu,\boldsymbol{\lambda}\nu}(\mathbf{q})\, a^\dagger_{\boldsymbol{\kappa}\mu}(t'')\, a_{\boldsymbol{\lambda}\nu}(t''). \tag{B.13}$$

The matrix elements read:

$$j^x_{\mathbf{k}m,\mathbf{l}n}(\mathbf{q}) = \frac{1}{(2\pi)^{3/2}} \int \mathrm{d}\mathbf{r}\, e^{-i\mathbf{q}\mathbf{r}}\, s v_{\mathrm{F}} e\, \varphi^\dagger_{\mathbf{k}m}(\mathbf{r})\, \sigma^x \varphi_{\mathbf{l}n}(\mathbf{r}), \tag{B.14}$$

$$\begin{aligned} t^{0y}_{\boldsymbol{\kappa}\mu,\boldsymbol{\lambda}\nu}(\mathbf{q}) = {} & \frac{1}{2}\frac{1}{(2\pi)^{3/2}} \int \mathrm{d}\mathbf{r}\, e^{+i\mathbf{q}\mathbf{r}} \varphi^\dagger_{\boldsymbol{\kappa}\mu}(\mathbf{r}) \left[-i\hbar v_{\mathrm{F}} \mathbb{I} \overleftrightarrow{\partial_y}\right] \varphi_{\boldsymbol{\lambda}\nu}(\mathbf{r}) \\ & + \frac{1}{4}\frac{1}{(2\pi)^{3/2}} \int \mathrm{d}\mathbf{r}\, e^{+i\mathbf{q}\mathbf{r}} \varphi^\dagger_{\boldsymbol{\kappa}\mu}(\mathbf{r}) \left[s\sigma^y \left(E_{\kappa_z\mu} + E_{\lambda_z\nu} - 2\mu\right)\right] \varphi_{\boldsymbol{\lambda}\nu}(\mathbf{r}), \end{aligned} \tag{B.15}$$

with $\varphi_{\mathbf{k}m}$ given by Equation (2.29):

$$\varphi_{\mathbf{k}m}(\mathbf{r}) = \frac{e^{ik_x x} e^{ik_z z}}{\sqrt{L_x L_z}} \frac{e^{-(y-k_x l_B^2)^2/2l_B^2}}{\sqrt{\alpha^2_{k_z ms}+1}} \begin{pmatrix} \frac{\alpha_{k_z ms}}{\sqrt{2^{M-1}(M-1)!\pi^{1/2} l_B}} H_{M-1}\left[\frac{y-k_x l_B^2}{l_B}\right] \\ \frac{1}{\sqrt{2^M M!\pi^{1/2} l_B}} H_M\left[\frac{y-k_x l_B^2}{l_B}\right] \end{pmatrix}. \tag{B.16}$$

By integrating Equations (B.14) and (B.15) over the x-z plane, one obtains a relation between the internal wave-vectors: $\mathbf{l} = \mathbf{k} + \mathbf{q}$ and $\boldsymbol{\lambda} = \boldsymbol{\kappa} - \mathbf{q}$. Introducing this inside the Equations (B.14) and (B.15) and following analogous steps to the ones presented in the previous section, one can recast the response function as:

$$\chi^{xy}(\mathbf{q},\omega) = \lim_{\eta\to 0^+} \sum_{\mathbf{k},mn} \frac{(2\pi)^3}{\mathcal{V}} \frac{i v_{\mathrm{F}} \hbar\, j^x_{\mathbf{k}m,\mathbf{k}+\mathbf{q}n}(\mathbf{q})\, t^{0y}_{\mathbf{k}+\mathbf{q}n,\mathbf{k}m}(\mathbf{q}) \left[n_{\mathbf{k}ms} - n_{\mathbf{k}+\mathbf{q}ns}\right]}{(E_{k_z ms} - E_{k_z+q_z ns} + i\hbar\eta)(E_{k_z ms} - E_{k_z+q_z ns} + \hbar\omega + i\hbar\eta)} \tag{B.17}$$

In the above expression, the denominator is composed by the product of two single-particle energy differences. It stems from the double integration over time that appears in the thermoelectric coefficient:

$$\chi^{\mathbf{q},\omega} \propto \int_{-\infty}^{\infty} \mathrm{d}t\, e^{i\omega(t-t')} \int_{-\infty}^{t'} \mathrm{d}t''\, \Theta(t-t')\, e^{i/\hbar(E_{k_z ms} - E_{k_z+q_z ns})(t-t'')} \tag{B.18}$$

[2]To simplify the notation, we have omitted the chirality dependence on the tensor indices. Current and energy-momentum operators are computed at the same Weyl node.

The ambiguity at infinite times is fixed by adding the relaxation term $e^{-\eta(t-t'')}$ inside the integrand. Solving the time-integrals, one obtains the result depicted in Equation (B.17).

B.3 Matrix elements: product of Hermite polynomials

The matrix elements described in Equations (B.14) and (B.15) are written in terms of Hermite polynomials that satisfy the formula [293]:

$$\int_{-\infty}^{\infty} \mathrm{d}y\, e^{y^2} H_r(y+a) H_s(x+b) = 2^s r! \pi^{1/2} b^{s-r} L_r^{s-r}(-2ab) \quad \text{for } s \geq r, \tag{B.19}$$

where $L_k^{\alpha}(x)$ is the generalized Laguerre polynomial. Depending on the energy levels (m and n) that we are considering, the position of each Hermite polynomial inside the integral should be arranged so that the condition described in Equation (B.19) ($s \geq r$) is satisfied. For the sake of clarity, consider as an example the electric current $j_{\mathbf{k}m,\mathbf{k}+\mathbf{q}n}(\mathbf{q})$. After some algebra, this matrix element reduces to:

$$\begin{aligned} j_{\mathbf{k}m,\mathbf{k}+\mathbf{q}n}(\mathbf{q}) = \frac{s v_{\mathrm{F}} e}{(2\pi)^{3/2}} \int \mathrm{d}\tilde{y}\, & \frac{e^{-q_x^2 l_B^2/4}\, e^{-q_y^2 l_B^2/4}\, e^{-i/2\, q_y(2k_x+q_x) l_B^2}\, e^{-\tilde{y}^2/l_B^2}}{\left[\alpha_{k_z ms}^2 + 1\right]^{1/2} \left[\alpha_{k_z+q_z ns}^2 + 1\right]^{1/2}} \\ \times \Bigg\{ & \frac{\alpha_{k_z ms}}{\sqrt{2^{M-1}(M-1)!\pi^{1/2} l_B}} \frac{1}{\sqrt{2^N N!\pi^{1/2} l_B}} H_{M-1}\left[\frac{\tilde{y}}{l_B} + \frac{q_1}{2}\right] H_N\left[\frac{\tilde{y}}{l_B} - \frac{q_2}{2}\right] \\ & + \frac{1}{\sqrt{2^M M!\pi^{1/2} l_B}} \frac{\alpha_{k_z+q_z ns}}{\sqrt{2^{N-1}(N-1)!\pi^{1/2} l_B}} H_M\left[\frac{\tilde{y}}{l_B} + \frac{q_1}{2}\right] H_{N-1}\left[\frac{\tilde{y}}{l_B} - \frac{q_2}{2}\right] \Bigg\}. \end{aligned} \tag{B.20}$$

where $q_1 = l_B\left(q_x - i q_y\right)$ and $q_2 = l_B\left(q_x + i q_y\right)$. In deriving Equation (B.20), the spatial variable y is rewritten as $y = \tilde{y} + l_B^2(2k_x + q_x)/2 - i l_B^2 q_y/2$. The ordering of the Hermite polynomials during the integration process will depend on the values taken by the indices M and N. Using Equation (B.19), the resulting expression takes the form:

$$j_{\mathbf{k}m,\mathbf{k}+\mathbf{q}n}(\mathbf{q}) = \frac{s v_{\mathrm{F}} e}{(2\pi)^{3/2}} \frac{e^{-(q_x^2+q_y^2) l_B^2/4}}{\left[\alpha_{k_z ms}^2 + 1\right]^{1/2}} \frac{e^{-i q_y l_B^2 (k_x+q_x/2)}}{\left[\alpha_{k_z+q_z ns}^2 + 1\right]^{1/2}} \left\{\Xi(\mathbf{q}, m, n) + \Xi_2(\mathbf{q}, m, n)\right\}, \tag{B.21}$$

where the functions Ξ are defined as:

$$\Xi_1(\mathbf{q},m,n) = \alpha_{k_z ms}\sqrt{\frac{2^N(M-1)!}{2^{M-1}N!}}\left(\frac{-q_2}{2}\right)^{N-M+1} L_{M-1}^{N-M+1}\left(\frac{\mathbf{q}^2 l_B^2}{2}\right) \quad (N \geq M-1), \tag{B.22}$$

$$\Xi_1(\mathbf{q},m,n) = \alpha_{k_z ms}\sqrt{\frac{2^{M-1}N!}{2^N(M-1)!}}\left(\frac{+q_1}{2}\right)^{M-N-1} L_{N}^{M-N-1}\left(\frac{\mathbf{q}^2 l_B^2}{2}\right) \quad (M \geq N+1), \tag{B.23}$$

and

$$\Xi_2(\mathbf{q},m,n) = \alpha_{k_z+q_z ns}\sqrt{\frac{2^{N-1}M!}{2^M(N-1)!}}\left(\frac{-q_2}{2}\right)^{N-M-1} L_{M}^{N-M-1}\left(\frac{\mathbf{q}^2 l_B^2}{2}\right) \quad (N \geq M+1), \tag{B.24}$$

$$\Xi_2(\mathbf{q},m,n) = \alpha_{k_z+q_z ns}\sqrt{\frac{2^M(N-1)!}{2^{N-1}M!}}\left(\frac{+q_1}{2}\right)^{M-N+1} L_{N-1}^{M-N+1}\left(\frac{\mathbf{q}^2 l_B^2}{2}\right) \quad (M \geq N-1), \tag{B.25}$$

with $\mathbf{q}^2 = q_x^2 + q_y^2$. The different terms in Ξ are chosen depending on the regime that we are studying. This scenario is considerably simplified when the local limit $\mathbf{q} \to 0$ is taken. In order to get non-vanishing results, the indices must satisfy the relation $N = M \pm 1$ to nullify the exponent, which restricts the possible transitions between Landau levels (selection rules). The combination of this relation and the local limit makes the generalized Laguerre polynomials equal to 1.

Energy-momentum tensor

The energy-momentum tensor deserves a more detailed analysis. It should be stressed that only the second line in Equation (B.15) is proportional to the chirality s of the node. The spatial derivative, when acting on the eigenfunctions of the unperturbed Hamiltonian, gives rise to two results. The first contribution stems from the exponential factors $\exp[-(y-\kappa_x l_B^2)^2/l_B^2]$. Being the resulting expression proportional to $\mathbf{q}$, this term vanishes in the local limit. The other contribution originates from the derivative acting on the Hermite polynomials, that satisfy the identity:

$$H_n'(x) = 2n\, H_{n-1}(x). \tag{B.26}$$

Once all the different elements are obtained, the calculation of the energy-momentum tensor $t^{0y}_{\mathbf{k}+\mathbf{q}n,\mathbf{k}m}$ follows analogously to the current case.

B.4 Thermoelectric response function

Finally, one gets the thermoelectric response coefficient after computing the product between the current and energy-momentum tensor at the different regimes. In the local limit, this coefficient is given by the expression:

$$\chi^{xy}(0,\omega) = \lim_{\eta\to 0^+} \frac{1}{4(2\pi)^2} \sum_{m,n}{}' \frac{s v_F e^2 B}{\hbar} \int \mathrm{d}\kappa_z \xi(m,n,\omega) \alpha^2_{\kappa_z ms} \times \left[s\left(E_{\kappa_z ms} + E_{\kappa_z ns} - 2\mu\right) - \alpha_{\kappa_z ns}\sqrt{M-1} - \sqrt{M}/\alpha_{\kappa_z ms} \right], \quad \text{(B.27)}$$

where the summation is restricted to the condition $N = M-1$ and the dimensionless function $\xi(m,n,\omega)$ is defined as:

$$\xi(m,n,\omega) = \frac{2\left[n_{\kappa_z ms} - n_{\kappa_z ns}\right]\left[\alpha^2_{\kappa_z ms}+1\right]^{-1}\left[\alpha^2_{\kappa_z ns}+1\right]^{-1}}{\left(E_{\kappa_z ms} - E_{\kappa_z ns} + i\eta\right)\left(E_{\kappa_z ms} - E_{\kappa_z ns} + \omega/\omega_c + i\eta\right)} \quad \text{(B.28)}$$

($\omega_c = v_F\sqrt{2eB/\hbar}$ is the cyclotron frequency). Some comments are in order at this point. In deriving Equation (B.27), the summation over the allowed values of $\mathbf{k}$ is written as an integral following the general expression:

$$\sum_{k_x,k_z} = \int \mathrm{d}k_x \mathrm{d}k_z \frac{L_x L_z}{4\pi^2}. \quad \text{(B.29)}$$

The integration over k_x is easily computed. Being the integrand independent of k_x, it accounts for the degeneracy factor $eBL_y/\hbar$ of each Landau level. The coefficient is further simplified by defining the dimensionless variable $\kappa_z = \hbar k_z/\sqrt{2eB\hbar}$. The eigenvalues are rewritten in the form $E_{k_z ms} = \hbar\omega_c E_{\kappa_z ms}$, with $E_{\kappa_z ms}$ a dimensionless Landau level. Gathering these considerations, the summation over the allowed values of $\mathbf{k}$ reads:

$$\sum_{\mathbf{k}} = \frac{\mathcal{V}\, eB\omega_c}{(2\pi)^2 v_F \hbar} \int \mathrm{d}\kappa_z. \quad \text{(B.30)}$$

The coefficient in front of the dimensionless integral is multiplied by the corresponding coefficients of the matrix elements, leading to the result shown in Equation (B.27).

Appendix C

Antisymmetric deformation tensor: two-dimensional versus three-dimensional Dirac crystals

In this appendix we give some details on the coupling of the antisymmetric part of the deformation tensor to the electronic excitations in Dirac matter. As discussed in chapter 4, the underlying symmetries of the crystalline structure constrain the possible interacting terms arising in the low-energy Hamiltonian. The different effective couplings are constructed using a symmetry approach and organized following a systematic expansion in derivatives of the strain tensor and the electron field. To maintain the continuum low-energy description of the electronic excitations as massless Dirac fermions, the expansion is restricted to be linear in the crystal momentum $\mathbf{k}$. It is known that the antisymmetric derivative of the displacement vector $\mathbf{u}$ can be eliminated from the effective Hamiltonian of 2D Dirac materials by a local rotation of the wave-function [294, 242]. The discussion becomes richer in three-dimensional Dirac systems, where the antisymmetric tensor is related to the vorticity vector. We will examine the term $\psi^\dagger \omega_{ij} \sigma_i k_j \psi$ describing the coupling of the antisymmetric part of the gradient deformation tensor $\omega_{ij} = 1/2\,(\partial_j u_i - \partial_i u_j)$ to the low-energy excitations in 2D and 3D Dirac materials.

Two-dimensional Dirac crystals

To first order in the derivative expansion, the effective 2D Hamiltonian induced by elastic deformations includes the term [294, 242]:

$$H = -i\hbar v_{\mathrm{F}} \psi^{\dagger} \sigma_j \overleftrightarrow{\partial_j} \psi - i\hbar v_{\mathrm{F}} \psi^{\dagger} \left(u_{jk} + \omega_{jk}\right) \sigma_j \overleftrightarrow{\partial_k} \psi \tag{C.1}$$

where we use the symmetric convention for the derivatives acting on the electron fields and u_{jk} is the strain tensor. In two-dimensional systems, any antisymmetric tensor is equivalent to a pseudo-scalar field $\omega_{jk} = \epsilon_{jk}\omega$, where ϵ_{jk} is the Levi-Civita symbol. The dependence on ω_{jk} in Equation (C.1) is canceled by performing a local rotation of the spinor [294]:

$$\psi \rightarrow \tilde{\psi} = e^{(i/2)\omega\sigma_3}\psi, \tag{C.2}$$

where we have used the relation:

$$i\sigma_j\sigma_3 = \epsilon_{jk}\sigma_k. \tag{C.3}$$

Indeed, introducing Equations (C.2) and (C.3) in Equation (C.1) and expanding to linear order in the antisymmetric tensor ω_{jk}, we get:

$$\begin{aligned} H &= -i\hbar v_{\mathrm{F}}\, \psi^{\dagger} \sigma_j \overleftrightarrow{\partial_j} \psi - i\hbar v_{\mathrm{F}}\, \psi^{\dagger} \left(u_{jk} + \omega_{jk}\right) \sigma_j \overleftrightarrow{\partial_k} \psi \\ &+ \frac{\hbar v_{\mathrm{F}}}{4} \psi^{\dagger} \left\{\sigma_j, \sigma_3\right\} \left(\partial_j \omega\right) \psi + i\hbar v_{\mathrm{F}}\, \psi^{\dagger} \left(\epsilon_{jk}\omega\right) \sigma_j \overleftrightarrow{\partial_k} \psi \\ &= -i\hbar v_{\mathrm{F}}\, \psi^{\dagger} \sigma_j \overleftrightarrow{\partial_j} \psi - i\hbar v_{\mathrm{F}}\, \psi^{\dagger} \left(u_{jk}\right) \sigma_j \overleftrightarrow{\partial_k} \psi \end{aligned} \tag{C.4}$$

(the contribution from $\partial_j\omega$ vanishes as well after using the anticommutation relation of the Pauli matrices). Thus, the effective Hamiltonian of 2D Dirac systems does not depend on ω_{jk}.

Three-dimensional Dirac crystals

Similarly to the previous case, it is possible to cancel the contribution proportional to ω_{jk} by a rotation of the spinors. However, this transformation leaves a term proportional to the divergence of the rotated vector not present in the two-dimensional system. Consider as before the general Hamiltonian

$$H = -i\hbar v_{\mathrm{F}}\, \psi^{\dagger} \sigma_j \overleftrightarrow{\partial_j} \psi - i\hbar v_{\mathrm{F}}\, \psi^{\dagger} \mathcal{V}_{jk} \sigma_j \overleftrightarrow{\partial_k} \psi, \tag{C.5}$$

where $\mathcal{V}_{jk} = \epsilon_{jkl} V_l$ is an antisymmetric tensor (for the particular case of elastic deformations, $\mathcal{V}_{jk} = \omega_{jk} = \epsilon_{jkl}\Omega_l$, with Ω_l being the rotational vector). As before, a local rotation

$$\psi \rightarrow \tilde{\psi} = e^{(i/2)V_l \sigma_l} \psi \tag{C.6}$$

eliminates the contribution proportional to the antisymmetric tensor $\mathcal{V}_{jk}$. Unlike the previous case, where the axis perpendicular to the plane was a privileged direction, we must consider an arbitrary rotation (without any particular orientation) in three-dimensional systems. The resulting expression after applying the transformation described in Equation (C.6) and expanding to linear order in $\mathcal{V}_{jk}$ reads:

$$\begin{aligned} H &= -i\hbar v_{\mathrm{F}}\, \psi^{\dagger}\sigma_j \overleftrightarrow{\partial_j}\psi - i\hbar v_{\mathrm{F}}\, \psi^{\dagger}\mathcal{V}_{jk}\sigma_j \overleftrightarrow{\partial_k}\psi \\ &\quad + \frac{\hbar v_{\mathrm{F}}}{4}\psi^{\dagger}\left\{\sigma_j, \sigma_k\right\}\left(\partial_j V_k\right)\psi + i\hbar v_{\mathrm{F}}\, \psi^{\dagger}\left(\epsilon_{jkl} V_l\right)\sigma_j \overleftrightarrow{\partial_k}\psi \\ &= -i\hbar v_{\mathrm{F}}\, \psi^{\dagger}\sigma_j \overleftrightarrow{\partial_j}\psi + \frac{\hbar v_{\mathrm{F}}}{4}\psi^{\dagger}\left\{\sigma_j, \sigma_k\right\}\left(\partial_j V_k\right)\psi, \end{aligned} \tag{C.7}$$

where we used the relation between the Pauli matrices:

$$\{\sigma_a, \sigma_b\} = 2\delta_{ab} \tag{C.8}$$

$$\sigma_a \sigma_b = 2i\epsilon_{abc}\sigma_c + 2\delta_{ab} \tag{C.9}$$

The coupling of $\mathcal{V}_{jk}$ to the electronic degrees of freedom is removed by the local rotation, but a contribution proportional to the divergence of the vector $\mathbf{V}$ emerges. The antisymmetric tensor is dual to a pseudo-vector in 3D systems that gives rise to new terms in the effective model.

Bibliography

1. Dirac, P. A. M. & Fowler, R. H. The quantum theory of the electron. *Proceedings of the Royal Society of London. Series A, Containing Papers of a Mathematical and Physical Character* **117,** 610–624 (1928) (cited on page 1).
2. Shankar, R. Renormalization-group approach to interacting fermions. *Rev. Mod. Phys.* **66,** 129–192 (1 1994) (cited on pages 1, 4, 38).
3. Wilson, K. G. The renormalization group: Critical phenomena and the Kondo problem. *Rev. Mod. Phys.* **47,** 773–840 (4 1975) (cited on page 1).
4. Herring, C. Accidental Degeneracy in the Energy Bands of Crystals. *Phys. Rev.* **52,** 365–373 (4 1937) (cited on pages 2, 4).
5. A. Abrikosov, A. & D. Beneslavskii, S. Possible Existence of Substances Intermediate Between Metals and Dielectrics. *Journal of Experimental and Theoretical Physics* **32** (1971) (cited on pages 2, 5).
6. Novoselov, K. S. *et al.* Two-dimensional gas of massless Dirac fermions in graphene. *Nature* **438,** 197 (2005) (cited on pages 2, 67).
7. Zhang, Y., Tan, Y.-W., Stormer, H. L. & Kim, P. Experimental observation of the quantum Hall effect and Berry's phase in graphene. *Nature* **438,** 201 (2005) (cited on pages 2, 67).
8. Castro Neto, A. H., Guinea, F., Peres, N. M. R., Novoselov, K. S. & Geim, A. K. The electronic properties of graphene. *Rev. Mod. Phys.* **81,** 109–162 (1 2009) (cited on pages 2, 54, 56, 77).
9. Fu, L., Kane, C. L. & Mele, E. J. Topological Insulators in Three Dimensions. *Phys. Rev. Lett.* **98,** 106803 (10 2007) (cited on page 2).
10. Hasan, M. Z. & Kane, C. L. Colloquium: Topological insulators. *Rev. Mod. Phys.* **82,** 3045–3067 (4 2010) (cited on pages 2, 7).

11. Qi, X.-L. & Zhang, S.-C. Topological insulators and superconductors. *Rev. Mod. Phys.* **83,** 1057–1110 (4 2011) (cited on pages 2, 7).

12. Bernevig, B. & Hughes, T. *Topological Insulators and Topological Superconductors* (Princeton University Press, 2013) (cited on pages 2, 7).

13. Liu, Z. K. *et al.* Discovery of a Three-Dimensional Topological Dirac Semimetal, Na3Bi. *Science* **343,** 864–867 (2014) (cited on pages 2, 13).

14. Neupane, M. *et al.* Observation of a three-dimensional topological Dirac semimetal phase in high-mobility Cd3As2. *Nature Communications* **5,** 3786 (2014) (cited on pages 2, 13).

15. Lv, B. Q. *et al.* Experimental Discovery of Weyl Semimetal TaAs. *Phys. Rev. X* **5,** 031013 (3 2015) (cited on pages 2, 15).

16. Xu, S.-Y. *et al.* Discovery of a Weyl fermion semimetal and topological Fermi arcs. *Science* **349,** 613–617 (2015) (cited on pages 2, 15).

17. Burkov, A. A. & Balents, L. Weyl Semimetal in a Topological Insulator Multilayer. *Phys. Rev. Lett.* **107,** 127205 (12 2011) (cited on pages 2, 13–15).

18. Wan, X., Turner, A. M., Vishwanath, A. & Savrasov, S. Y. Topological semimetal and Fermi-arc surface states in the electronic structure of pyrochlore iridates. *Phys. Rev. B* **83,** 205101 (20 2011) (cited on pages 2, 5, 9, 14, 15).

19. Armitage, N. P., Mele, E. J. & Vishwanath, A. Weyl and Dirac semimetals in three-dimensional solids. *Rev. Mod. Phys.* **90,** 015001 (1 2018) (cited on pages 2, 9).

20. Burkov, A. A. Topological semimetals. *Nature Materials* **15,** 1145 (2016) (cited on pages 2, 5).

21. Burkov, A. Weyl Metals. *Annual Review of Condensed Matter Physics* **9,** 359–378 (2018) (cited on pages 2, 11, 15).

22. Landsteiner, K. Notes on Anomaly Induced Transport. *Acta Physica Polonica B* **47,** 2617 (2016) (cited on pages 2, 10, 20, 64).

23. Turner, A. M. & Vishwanath, A. Beyond band insulators: topology of semimetals and interacting phases. *Topological Insulators* **6,** 293–324 (2013) (cited on pages 2, 9).

24. Lu, H.-Z. & Shen, S.-Q. Quantum transport in topological semimetals under magnetic fields. *Frontiers of Physics* **12,** 127201 (2017) (cited on page 2).

25. Ilan, R., Grushin, A. G. & Pikulin, D. I. Pseudo-electromagnetic fields in topological semimetals. *arXiv preprint arXiv:1903.11088* (2019) (cited on pages 2, 54, 57, 58, 67).

26. Weyl, H. Gravitation and the Electron. *Proceedings of the National Academy of Sciences of the United States of America* **15,** 323–334 (1929) (cited on page 2).

27. Peskin, M. E. & Schroeder, D. V. *An introduction to quantum field theory* Includes exercises (Westview, Boulder, CO, 1995) (cited on pages 3, 9, 22, 30, 31, 71).

28. Kajita, T. Nobel Lecture: Discovery of atmospheric neutrino oscillations. *Rev. Mod. Phys.* **88,** 030501 (3 2016) (cited on page 3).

29. McDonald, A. B. Nobel Lecture: The Sudbury Neutrino Observatory: Observation of flavor change for solar neutrinos. *Rev. Mod. Phys.* **88,** 030502 (3 2016) (cited on page 3).

30. Satz, H. The Quark-Gluon Plasma – A Short Introduction. *Nuclear Physics A* **862-863.** The Sixth International Conference on Physics and Astrophysics of Quark Gluon Plasma (ICPAQGP-2010), 4–12 (2011) (cited on page 3).

31. Kharzeev, D., Liao, J., Voloshin, S. & Wang, G. Chiral magnetic and vortical effects in high-energy nuclear collisions—A status report. *Progress in Particle and Nuclear Physics* **88,** 1–28 (2016) (cited on page 3).

32. Ashcroft, N. & Mermin, N. *Solid State Physics* (Holt, Rinehart and Winston, 1976) (cited on pages 3, 21, 38, 40).

33. Simon, S. H. *The Oxford solid state basics* (Oxford Univ. Press, Oxford, UK, 2013) (cited on page 3).

34. Marder, M. *Condensed Matter Physics* (Wiley, 2010) (cited on pages 4, 21, 33, 37, 38, 40).

35. Landau, L. D. The Theory of a Fermi Liquid. *J. Exptl. Theoret. Phys.* **3,** 1058–1064 (6 1957) (cited on page 4).

36. Polchinski, J. Effective field theory and the Fermi surface. *arXiv preprint hep-th/9210046* (1992) (cited on pages 4, 38).

37. Jain, J. K. Composite-fermion approach for the fractional quantum Hall effect. *Phys. Rev. Lett.* **63,** 199–202 (2 1989) (cited on page 4).

38. Jain, J. K. Composite Fermion Theory of Exotic Fractional Quantum Hall Effect. *Annual Review of Condensed Matter Physics* **6,** 39–62 (2015) (cited on page 4).

39. Halperin, B. I., Lee, P. A. & Read, N. Theory of the half-filled Landau level. *Phys. Rev. B* **47,** 7312–7343 (12 1993) (cited on page 4).

40. Ronen, Y. *et al.* Charge of a quasiparticle in a superconductor. *Proceedings of the National Academy of Sciences* **113,** 1743–1748 (2016) (cited on page 4).

41. Kivelson, S. A. & Rokhsar, D. S. Bogoliubov quasiparticles, spinons, and spin-charge decoupling in superconductors. *Phys. Rev. B* **41,** 11693–11696 (16 1990) (cited on page 4).

42. Skyrme, T. A unified field theory of mesons and baryons. *Nuclear Physics* **31,** 556–569 (1962) (cited on page 4).

43. Romming, N. *et al.* Writing and Deleting Single Magnetic Skyrmions. *Science* **341,** 636–639 (2013) (cited on page 4).

44. Von Neumann, J. & Wigner, E. Uber merkwürdige diskrete Eigenwerte. Uber das Verhalten von Eigenwerten bei adiabatischen Prozessen. *Z Phys* **30,** 467–470 (1929) (cited on page 4).

45. Adler, S. L. Axial-Vector Vertex in Spinor Electrodynamics. *Phys. Rev.* **177,** 2426–2438 (5 1969) (cited on pages 5, 10).

46. Bell, J. S. & Jackiw, R. A PCAC puzzle: $\pi^0 \to \gamma\ \gamma$ in the σ-model. *Il Nuovo Cimento A* **51,** 47–61 (1969) (cited on pages 5, 10).

47. Grabecki, G. *et al.* Interface transmission of (Nb, Pb, In)/NbP – superconductor/Weyl semimetal junctions (2019) (cited on page 6).

48. Ginzburg, V. L. & Landau, L. D. On the Theory of superconductivity. *J. Exp. Theor. Phys. USSR* **20,** 1064 (1950) (cited on pages 6, 7).

49. Bruus, H. & Flensberg, K. *Many-body quantum theory in condensed matter physics: an introduction* (Oxford Graduate Texts, 2004) (cited on pages 7, 21, 23, 44, 93, 94).

50. Nakahara, M. *Geometry, topology and physics* (Hilger, Bristol, 1990) (cited on pages 7, 31, 90, 92).

51. Anderson, M. H., Ensher, J. R., Matthews, M. R., Wieman, C. E. & Cornell, E. A. Observation of Bose-Einstein Condensation in a Dilute Atomic Vapor. *Science* **269,** 198–201 (1995) (cited on page 7).

52. Davis, K. B. *et al.* Bose-Einstein Condensation in a Gas of Sodium Atoms. *Phys. Rev. Lett.* **75,** 3969–3973 (22 1995) (cited on page 7).

53. Bradley, C. C., Sackett, C. A., Tollett, J. J. & Hulet, R. G. Evidence of Bose-Einstein Condensation in an Atomic Gas with Attractive Interactions. *Phys. Rev. Lett.* **75,** 1687–1690 (9 1995) (cited on page 7).

54. Thouless, D. J., Kohmoto, M., Nightingale, M. P. & den Nijs, M. Quantized Hall Conductance in a Two-Dimensional Periodic Potential. *Phys. Rev. Lett.* **49,** 405–408 (6 1982) (cited on pages 7, 90).

55. Shen, S. *Topological Insulators: Dirac Equation in Condensed Matter* (Springer Singapore, 2017) (cited on page 7).

56. Karplus, R. & Luttinger, J. M. Hall Effect in Ferromagnetics. *Phys. Rev.* **95,** 1154–1160 (5 1954) (cited on pages 7, 38).

57. Kane, C. L. & Mele, E. J. Z_2 Topological Order and the Quantum Spin Hall Effect. *Phys. Rev. Lett.* **95,** 146802 (14 2005) (cited on pages 7, 8).

58. Schnyder, A. P., Ryu, S., Furusaki, A. & Ludwig, A. W. W. Classification of topological insulators and superconductors in three spatial dimensions. *Phys. Rev. B* **78,** 195125 (19 2008) (cited on page 7).

59. Chiu, C.-K., Teo, J. C. Y., Schnyder, A. P. & Ryu, S. Classification of topological quantum matter with symmetries. *Rev. Mod. Phys.* **88,** 035005 (3 2016) (cited on page 7).

60. Altland, A. & Zirnbauer, M. R. Nonstandard symmetry classes in mesoscopic normal-superconducting hybrid structures. *Phys. Rev. B* **55,** 1142–1161 (2 1997) (cited on page 7).

61. Ryu, S., Schnyder, A. P., Furusaki, A. & Ludwig, A. W. W. Topological insulators and superconductors: tenfold way and dimensional hierarchy. *New Journal of Physics* **12,** 065010 (2010) (cited on page 7).

62. Berry, M. V. Quantal phase factors accompanying adiabatic changes. *Proceedings of the Royal Society of London. A. Mathematical and Physical Sciences* **392,** 45–57 (1984) (cited on pages 7, 90).

63. Berry, M. V. in *Chaotic Behavior in Quantum Systems: Theory and Applications* (ed Casati, G.) 123–140 (Springer US, Boston, MA, 1985) (cited on pages 7, 92).

64. Volovik, G. & Press, O. U. *The Universe in a Helium Droplet* (Clarendon Press, 2003) (cited on pages 7, 13).

65. Nielsen, H. & Ninomiya, M. A no-go theorem for regularizing chiral fermions. *Physics Letters B* **105,** 219–223 (1981) (cited on pages 8, 92).

66. Ludwig, A. W. W., Fisher, M. P. A., Shankar, R. & Grinstein, G. Integer quantum Hall transition: An alternative approach and exact results. *Phys. Rev. B* **50,** 7526–7552 (11 1994) (cited on page 8).

67. Balents, L. Weyl electrons kiss. *Physics* **4,** 36 (2011) (cited on page 9).

68. Xu, S.-Y. *et al.* Experimental discovery of a topological Weyl semimetal state in TaP. *Science Advances* **1** (2015) (cited on page 9).

69. Liu, Z. K. *et al.* Evolution of the Fermi surface of Weyl semimetals in the transition metal pnictide family. *Nature Materials* **15,** 27 (2015) (cited on pages 9, 15).

70. Hosur, P. Friedel oscillations due to Fermi arcs in Weyl semimetals. *Phys. Rev. B* **86,** 195102 (19 2012) (cited on page 9).

71. Ojanen, T. Helical Fermi arcs and surface states in time-reversal invariant Weyl semimetals. *Phys. Rev. B* **87,** 245112 (24 2013) (cited on page 9).

72. Potter, A. C., Kimchi, I. & Vishwanath, A. Quantum oscillations from surface Fermi arcs in Weyl and Dirac semimetals. *Nature Communications* **5,** 5161 (2014) (cited on page 9).

73. Noether, E. Invariant variation problems. *Transport Theory and Statistical Physics* **1,** 186–207 (1971) (cited on pages 9, 22, 31).

74. Bertlmann, R. A. *Anomalies in quantum field theory* (Clarendon Press, 1996) (cited on pages 10, 22).

75. Holstein, B. R. Anomalies for pedestrians. *American Journal of Physics* **61,** 142–147 (1993) (cited on page 10).

76. Kim, H.-J. *et al.* Dirac versus Weyl Fermions in Topological Insulators: Adler-Bell-Jackiw Anomaly in Transport Phenomena. *Phys. Rev. Lett.* **111,** 246603 (24 2013) (cited on pages 10, 22).

77. Son, D. T. & Spivak, B. Z. Chiral anomaly and classical negative magnetoresistance of Weyl metals. *Phys. Rev. B* **88,** 104412 (10 2013) (cited on page 10).

78. Xiong, J. *et al.* Evidence for the chiral anomaly in the Dirac semimetal Na3Bi. *Science* **350,** 413–416 (2015) (cited on pages 10, 11, 22, 68).

79. Li, C. Z. *et al.* Giant negative magnetoresistance induced by the chiral anomaly in individual Cd3As2 nanowires. *Nature Communications* **6,** 1–7 (2015) (cited on pages 10, 11, 22, 68).

80. Zhang, C.-L. *et al.* Signatures of the Adler–Bell–Jackiw chiral anomaly in a Weyl fermion semimetal. *Nature communications* **7,** 10735 (2016) (cited on pages 10, 11, 68).

81. Nielsen, H. & Ninomiya, M. Absence of neutrinos on a lattice: (I). Proof by homotopy theory. *Nuclear Physics B* **185,** 20–40 (1981) (cited on pages 10, 92).

82. Nielsen, H. & Ninomiya, M. Absence of neutrinos on a lattice: (II). Intuitive topological proof. *Nuclear Physics B* **193,** 173–194 (1981) (cited on page 10).

83. Li, H. *et al.* Negative magnetoresistance in Dirac semimetal Cd3As2. *Nature Communications* **7,** 10301 (2016) (cited on page 11).

84. Shekhar, C. *et al.* Extremely large magnetoresistance and ultrahigh mobility in the topological Weyl semimetal candidate NbP. *Nature Physics* **11,** 645 (2015) (cited on page 11).

85. Kharzeev, D. E., McLerran, L. D. & Warringa, H. J. The effects of topological charge change in heavy ion collisions: "Event by event P and CP violation". *Nuclear Physics A* **803,** 227–253 (2008) (cited on page 11).

86. Kharzeev, D. E. The Chiral Magnetic Effect and anomaly-induced transport. *Progress in Particle and Nuclear Physics* **75,** 133–151 (2014) (cited on pages 11, 22).

87. Başar, G., Kharzeev, D. E. & Yee, H.-U. Triangle anomaly in Weyl semimetals. *Phys. Rev. B* **89,** 035142 (3 2014) (cited on page 11).

88. Li, Q. *et al.* Chiral magnetic effect in ZrTe5. *Nature Physics* **12,** 550 (2016) (cited on page 11).

89. Gooth, J. *et al.* Experimental signatures of the mixed axial–gravitational anomaly in the Weyl semimetal NbP. *Nature* **547,** 324 (2017) (cited on pages 11, 22).

90. Schindler, C. *et al.* Observation of an anomalous heat current in a Weyl fermion semimetal. *arXiv preprint arXiv:1810.02300* (2018) (cited on pages 11, 22).

91. Chernodub, M. N. Anomalous Transport Due to the Conformal Anomaly. *Phys. Rev. Lett.* **117,** 141601 (14 2016) (cited on pages 11, 22, 35).

92. Chernodub, M. N. & Zubkov, M. A. Scale magnetic effect in quantum electrodynamics and the Wigner-Weyl formalism. *Phys. Rev. D* **96,** 056006 (5 2017) (cited on page 11).

93. Chernodub, M. N., Cortijo, A. & Vozmediano, M. A. H. Generation of a Nernst Current from the Conformal Anomaly in Dirac and Weyl Semimetals. *Phys. Rev. Lett.* **120,** 206601 (20 2018) (cited on pages 11, 22, 23, 28, 35).

94. Sakurai, J. J. & Napolitano, J. *Modern quantum mechanics* (Pearson Harlow, 1994) (cited on pages 12, 25).

95. Xiao, D., Chang, M.-C. & Niu, Q. Berry phase effects on electronic properties. *Rev. Mod. Phys.* **82,** 1959–2007 (3 2010) (cited on pages 12, 18, 38).

96. Witten, E. Three lectures on topological phases of matter. *Rivista del Nuovo Cimento* (2016) (cited on pages 12, 90).

97. Young, S. M. *et al.* Dirac Semimetal in Three Dimensions. *Phys. Rev. Lett.* **108,** 140405 (14 2012) (cited on page 13).

98. Murakami, S. Phase transition between the quantum spin Hall and insulator phases in 3D: Emergence of a topological gapless phase. *New Journal of Physics* (2007) (cited on page 13).

99. Smith, J. C., Banerjee, S., Pardo, V. & Pickett, W. E. Dirac Point Degenerate with Massive Bands at a Topological Quantum Critical Point. *Phys. Rev. Lett.* **106,** 056401 (5 2011) (cited on page 13).

100. Wang, W. *et al.* Evidence for Layered Quantized Transport in Dirac Semimetal ZrTe5. *Scientific Reports* **8,** 5125 (2018) (cited on page 13).

101. Wang, Z. *et al.* Dirac semimetal and topological phase transitions in A_3Bi (A = Na, K, Rb). *Phys. Rev. B* **85,** 195320 (19 2012) (cited on page 13).

102. Wang, Z., Weng, H., Wu, Q., Dai, X. & Fang, Z. Three-dimensional Dirac semimetal and quantum transport in Cd_3As_2. *Phys. Rev. B* **88,** 125427 (12 2013) (cited on pages 13, 62).

103. Borisenko, S. *et al.* Experimental Realization of a Three-Dimensional Dirac Semimetal. *Phys. Rev. Lett.* **113,** 027603 (2 2014) (cited on page 13).

104. Liu, Z. K. *et al.* A stable three-dimensional topological Dirac semimetal Cd3As2. *Nature Materials* **13,** 677 (2014) (cited on page 13).

105. Zyuzin, A. A., Wu, S. & Burkov, A. A. Weyl semimetal with broken time reversal and inversion symmetries. *Phys. Rev. B* **85,** 165110 (16 2012) (cited on page 13).

106. Grushin, A. G. Consequences of a condensed matter realization of Lorentz-violating QED in Weyl semi-metals. *Phys. Rev. D* **86,** 045001 (4 2012) (cited on page 13).

107. Halász, G. B. & Balents, L. Time-reversal invariant realization of the Weyl semimetal phase. *Phys. Rev. B* **85,** 035103 (3 2012) (cited on page 14).

108. Huang, S.-M. *et al.* A Weyl Fermion semimetal with surface Fermi arcs in the transition metal monopnictide TaAs class. *Nature Communications* **6,** 7373 (2015) (cited on page 15).

109. Weng, H., Fang, C., Fang, Z., Bernevig, B. A. & Dai, X. Weyl Semimetal Phase in Noncentrosymmetric Transition-Metal Monophosphides. *Phys. Rev. X* **5,** 011029 (1 2015) (cited on page 15).

110. Yang, L. X. *et al.* Weyl semimetal phase in the non-centrosymmetric compound TaAs. *Nature Physics* **11,** 728 (2015) (cited on page 15).

111. Lv, B. Q. *et al.* Observation of Weyl nodes in TaAs. *Nature Physics* **11,** 724 (2015) (cited on page 15).

112. Xu, S. Y. *et al.* Discovery of a Weyl fermion state with Fermi arcs in niobium arsenide. *Nature Phys.* **11,** 748 (2015) (cited on page 15).

113. Xu, N. *et al.* Observation of Weyl nodes and Fermi arcs in tantalum phosphide. *Nature Communications* **7,** 11006 (2016) (cited on page 15).

114. Borisenko, S. *et al.* Time-reversal symmetry breaking type-II Weyl state in YbMnBi2. *Nature Communications* **10,** 3424 (2019) (cited on page 15).

115. Kuroda, K. *et al.* Evidence for magnetic Weyl fermions in a correlated metal. *Nature Materials* **16,** 1090 (2017) (cited on page 15).

116. Li, X. *et al.* Anomalous Nernst and Righi-Leduc Effects in Mn_3Sn: Berry Curvature and Entropy Flow. *Phys. Rev. Lett.* **119,** 056601 (5 2017) (cited on page 15).

117. Reichlova, H. *et al.* Imaging and writing magnetic domains in the non-collinear antiferromagnet Mn_3Sn (2019) (cited on page 15).

118. Taylor, J. M. *et al.* Magnetic and electrical transport signatures of uncompensated moments in epitaxial thin films of the noncollinear antiferromagnet Mn3Ir. *Applied Physics Letters* **115,** 062403 (2019) (cited on page 15).

119. Wuttke, C. *et al.* Berry curvature unravelled by the anomalous Nernst effect in Mn_3Ge. *Phys. Rev. B* **100,** 085111 (8 2019) (cited on page 15).

120. Wurmehl, S. *et al.* Geometric, electronic, and magnetic structure of Co_2FeSi: Curie temperature and magnetic moment measurements and calculations. *Phys. Rev. B* **72,** 184434 (18 2005) (cited on page 15).

121. Kübler, J. & Felser, C. Weyl points in the ferromagnetic Heusler compound Co2MnAl. *EPL (Europhysics Letters)* **114,** 47005 (2016) (cited on page 15).

122. Wang, Z. *et al.* Time-Reversal-Breaking Weyl Fermions in Magnetic Heusler Alloys. *Phys. Rev. Lett.* **117,** 236401 (23 2016) (cited on page 15).

123. Watzman, S. J. *et al.* Dirac dispersion generates unusually large Nernst effect in Weyl semimetals. *Phys. Rev. B* **97,** 161404 (16 2018) (cited on pages 15, 17, 18, 22, 39, 43).

124. Manna, K. *et al.* From Colossal to Zero: Controlling the Anomalous Hall Effect in Magnetic Heusler Compounds via Berry Curvature Design. *Phys. Rev. X* **8,** 041045 (4 2018) (cited on pages 15, 18, 22).

125. Li, X.-Z., Zhang, W.-Y., Valloppilly, S. & Sellmyer, D. J. New Heusler compounds in Ni-Mn-In and Ni-Mn-Sn alloys. *Scientific Reports* **9,** 7762 (2019) (cited on page 15).

126. Markou, A. *et al.* Thickness dependence of the anomalous Hall effect in thin films of the topological semimetal Co_2MnGa. *Phys. Rev. B* **100,** 054422 (5 2019) (cited on page 15).

127. Li, G. *et al.* Surface states in bulk single crystal of topological semimetal Co3Sn2S2 toward water oxidation. *Science Advances* **5** (2019) (cited on page 15).

128. Liu, D. F. *et al.* Magnetic Weyl semimetal phase in a Kagomé crystal. *Science* **365,** 1282–1285 (2019) (cited on page 15).

129. Soluyanov, A. A. *et al.* Type-II Weyl semimetals. *Nature* **527,** 495 (2015) (cited on pages 15, 16, 58).

130. Grushin, A. G. in *Topological Matter* 149–175 (Springer, 2018) (cited on page 16).

131. Bradlyn, B. *et al.* Beyond Dirac and Weyl fermions: Unconventional quasiparticles in conventional crystals. *Science* **353** (2016) (cited on page 16).

132. Beenakker, C. Bringing order to the expanding fermion zoo. *Science* **353,** 539–540 (2016) (cited on page 16).

133. Ali, M. N. *et al.* Large, non-saturating magnetoresistance in WTe2. *Nature* **514,** 205–208 (2014) (cited on pages 16, 58).

134. Huang, L. *et al.* Spectroscopic evidence for a type II Weyl semimetallic state in MoTe2. *Nature Materials* **15,** 1155 (2016) (cited on pages 16, 58).

135. Snyder, G. J. & Toberer, E. S. Complex thermoelectric materials. *Nature Materials* **7,** 105–114 (2008) (cited on page 17).

136. Fu, C. *et al.* Large Nernst power factor over a broad temperature range in polycrystalline Weyl semimetal NbP. *Energy Environ. Sci.* **11,** 2813–2820 (10 2018) (cited on page 17).

137. He, J. & Tritt, T. M. Advances in thermoelectric materials research: Looking back and moving forward. *Science* **357** (2017) (cited on page 17).

138. Ziman, J. *Electrons and Phonons: The Theory of Transport Phenomena in Solids* (OUP Oxford, 2001) (cited on pages 17, 21, 35, 38–41).

139. Rowe, D. *CRC Handbook of Thermoelectrics* (CRC Press, 1995) (cited on page 17).

140. Behnia, K., Méasson, M.-A. & Kopelevich, Y. Nernst Effect in Semimetals: The Effective Mass and the Figure of Merit. *Phys. Rev. Lett.* **98,** 076603 (7 2007) (cited on page 17).

141. Behnia, K. & Aubin, H. Nernst effect in metals and superconductors: a review of concepts and experiments. *Reports on Progress in Physics* **79,** 046502 (2016) (cited on page 17).

142. Lundgren, R., Laurell, P. & Fiete, G. A. Thermoelectric properties of Weyl and Dirac semimetals. *Phys. Rev. B* **90,** 165115 (16 2014) (cited on pages 17, 22).

143. Sharma, G., Goswami, P. & Tewari, S. Nernst and magnetothermal conductivity in a lattice model of Weyl fermions. *Phys. Rev. B* **93,** 035116 (3 2016) (cited on pages 17, 22, 50).

144. Sharma, G., Moore, C., Saha, S. & Tewari, S. Nernst effect in Dirac and inversion-asymmetric Weyl semimetals. *Phys. Rev. B* **96,** 195119 (19 2017) (cited on pages 17, 42, 50).

145. Nagaosa, N., Sinova, J., Onoda, S., MacDonald, A. H. & Ong, N. P. Anomalous Hall effect. *Rev. Mod. Phys.* **82,** 1539–1592 (2 2010) (cited on page 18).

146. Pu, Y., Chiba, D., Matsukura, F., Ohno, H. & Shi, J. Mott Relation for Anomalous Hall and Nernst Effects in $Ga_{1-x}Mn_xAs$ Ferromagnetic Semiconductors. *Phys. Rev. Lett.* **101,** 117208 (11 2008) (cited on pages 18, 39).

147. Burkov, A. A. Anomalous Hall Effect in Weyl Metals. *Phys. Rev. Lett.* **113,** 187202 (18 2014) (cited on pages 18, 19, 45).

148. Liang, T. *et al.* Anomalous Nernst Effect in the Dirac Semimetal Cd_3As_2. *Phys. Rev. Lett.* **118,** 136601 (13 2017) (cited on pages 18, 22, 39, 43, 50).

149. Jia, Z. *et al.* Thermoelectric signature of the chiral anomaly in Cd3As2. *Nature Communications* **7,** 13013 (2016) (cited on page 18).

150. Sakai, A. *et al.* Giant anomalous Nernst effect and quantum-critical scaling in a ferromagnetic semimetal. *Nature Physics* **14,** 1119 (2018) (cited on pages 18, 22, 39, 42, 50).

151. Yang, H. *et al.* Giant anomalous Nernst effect in the magnetic Weyl semimetal Co3Sn2S2. *arXiv preprint arXiv:1811.03485* (2018) (cited on pages 18, 22).

152. Guin, S. N. *et al.* Anomalous Nernst effect beyond the magnetization scaling relation in the ferromagnetic Heusler compound Co2MnGa. *NPG Asia Materials* (2019) (cited on pages 18, 43).

153. Skinner, B. & Fu, L. Large, nonsaturating thermopower in a quantizing magnetic field. *Science Advances* **4** (2018) (cited on pages 18, 39, 50).

154. Kozii, V., Skinner, B. & Fu, L. Thermoelectric Hall conductivity and figure of merit in Dirac/Weyl materials. *Phys. Rev. B* **99,** 155123 (15 2019) (cited on pages 18, 35).

155. Han, F. *et al.* Discovery of giant, non-saturating thermopower in topological semimetal at quantum limit. *arXiv preprint arXiv:1904.03179* (2019) (cited on pages 18, 22, 42).

156. Zhang, W. *et al.* Quantized plateau in the thermoelectric Hall conductivity for Dirac electrons in the extreme quantum limit. *arXiv preprint arXiv:1904.02157* (2019) (cited on pages 18, 22, 42).

157. Bardeen, J., Cooper, L. N. & Schrieffer, J. R. Theory of Superconductivity. *Phys. Rev.* **108,** 1175–1204 (5 1957) (cited on page 18).

158. Suzuura, H. & Ando, T. Phonons and electron-phonon scattering in carbon nanotubes. *Phys. Rev. B* **65,** 235412 (23 2002) (cited on pages 19, 51, 54, 56, 67).

159. Guinea, F., Katsnelson, M. I. & Geim, A. K. Energy gaps and a zero-field quantum Hall effect in graphene by strain engineering. *Nature Physics* **6,** 30–33 (2010) (cited on pages 19, 54, 67).

160. Vozmediano, M., Katsnelson, M. & Guinea, F. Gauge fields in graphene. *Physics Reports* **496,** 109–148 (2010) (cited on pages 19, 54, 67).

161. Cortijo, A., Ferreirós, Y., Landsteiner, K. & Vozmediano, M. A. H. Elastic Gauge Fields in Weyl Semimetals. *Phys. Rev. Lett.* **115,** 177202 (17 2015) (cited on pages 19, 54, 55, 57, 59, 67).

162. Cortijo, A., Kharzeev, D., Landsteiner, K. & Vozmediano, M. A. H. Strain-induced chiral magnetic effect in Weyl semimetals. *Phys. Rev. B* **94,** 241405 (24 2016) (cited on pages 19, 20, 57, 62, 83).

163. Levy, N. *et al.* Strain-Induced Pseudo–Magnetic Fields Greater Than 300 Tesla in Graphene Nanobubbles. *Science* **329,** 544–547 (2010) (cited on pages 19, 52, 54, 67, 83).

164. Shapourian, H., Hughes, T. L. & Ryu, S. Viscoelastic response of topological tight-binding models in two and three dimensions. *Phys. Rev. B* **92,** 165131 (16 2015) (cited on pages 19, 55, 59).

165. Pikulin, D. I., Chen, A. & Franz, M. Chiral Anomaly from Strain-Induced Gauge Fields in Dirac and Weyl Semimetals. *Phys. Rev. X* **6,** 041021 (4 2016) (cited on pages 19, 20, 54, 55, 57, 60, 62–67, 79–81).

166. Liu, T., Pikulin, D. I. & Franz, M. Quantum oscillations without magnetic field. *Phys. Rev. B* **95,** 041201 (4 2017) (cited on pages 19, 54, 57, 67, 79).

167. Cortijo, A. & Zubkov, M. Emergent gravity in the cubic tight-binding model of Weyl semimetal in the presence of elastic deformations. *Annals of Physics* **366,** 45–56 (2016) (cited on pages 19, 54, 57).

168. Gorbar, E. V., Miransky, V. A., Shovkovy, I. A. & Sukhachov, P. O. Pseudomagnetic lens as a valley and chirality splitter in Dirac and Weyl materials. *Phys. Rev. B* **95,** 241114 (24 2017) (cited on pages 19, 57).

169. Gorbar, E. V., Miransky, V. A., Shovkovy, I. A. & Sukhachov, P. O. Pseudomagnetic helicons. *Phys. Rev. B* **95,** 115422 (11 2017) (cited on pages 19, 57, 67).

170. Gorbar, E. V., Miransky, V. A., Shovkovy, I. A. & Sukhachov, P. O. Chiral response in lattice models of Weyl materials. *Phys. Rev. B* **96,** 125123 (12 2017) (cited on pages 19, 57).

171. Zabolotskiy, A. & Lozovik, Y. Strain-induced pseudomagnetic and scalar fields in symmetry-enforced Dirac nodes. *Journal of Magnetism and Magnetic Materials* **459,** 43–45 (2018) (cited on pages 19, 57, 83).

172. Huang, Z.-M., Zhou, J. & Shen, S.-Q. Topological responses from chiral anomaly in multi-Weyl semimetals. *Phys. Rev. B* **96,** 085201 (8 2017) (cited on pages 19, 57, 67).

173. Liu, C.-X., Ye, P. & Qi, X.-L. Chiral gauge field and axial anomaly in a Weyl semimetal. *Phys. Rev. B* **87,** 235306 (23 2013) (cited on pages 20, 64).

174. Huang, Z.-M., Zhou, J. & Shen, S.-Q. Topological responses from chiral anomaly in multi-Weyl semimetals. *Phys. Rev. B* **96,** 085201 (8 2017) (cited on page 20).

175. Grushin, A. G., Venderbos, J. W. F., Vishwanath, A. & Ilan, R. Inhomogeneous Weyl and Dirac Semimetals: Transport in Axial Magnetic Fields and Fermi Arc Surface States from Pseudo-Landau Levels. *Phys. Rev. X* **6,** 041046 (4 2016) (cited on pages 20, 54, 57, 67).

176. Giuliani, G. & Vignale, G. *Quantum Theory of the Electron Liquid* (Cambridge University Press, 2005) (cited on pages 21, 23, 45, 93, 95).

177. Coleman, P. *Introduction to Many-Body Physics* (Cambridge University Press, 2015) (cited on page 21).

178. Ming-Che, C. & Qian, N. Berry curvature, orbital moment, and effective quantum theory of electrons in electromagnetic fields. *Journal of Physics: Condensed Matter* (2008) (cited on page 21).

179. Landsteiner, K. Anomalous transport of Weyl fermions in Weyl semimetals. *Phys. Rev. B* **89,** 075124 (7 2014) (cited on pages 22, 64).

180. Behnia, K. & Aubin, H. *Nernst effect in metals and superconductors: a review of concepts and experiments* 2016 (cited on pages 22, 37).

181. Ferreiros, Y., Zyuzin, A. A. & Bardarson, J. H. Anomalous Nernst and thermal Hall effects in tilted Weyl semimetals. *Phys. Rev. B* **96,** 115202 (11 2017) (cited on page 22).

182. Gorbar, E. V., Miransky, V. A., Shovkovy, I. A. & Sukhachov, P. O. Anomalous thermoelectric phenomena in lattice models of multi-Weyl semimetals. *Phys. Rev. B* **96,** 155138 (15 2017) (cited on pages 22, 38, 42, 43).

183. Tolman, R. C. & Ehrenfest, P. Temperature Equilibrium in a Static Gravitational Field. *Phys. Rev.* **36,** 1791–1798 (12 1930) (cited on pages 22, 24).

184. Luttinger, J. M. Theory of Thermal Transport Coefficients. *Phys. Rev.* **135,** A1505–A1514 (6A 1964) (cited on pages 22, 24, 25, 38).

185. Cooper, N. R., Halperin, B. I. & Ruzin, I. M. Thermoelectric response of an interacting two-dimensional electron gas in a quantizing magnetic field. *Phys. Rev. B* **55,** 2344–2359 (4 1997) (cited on pages 24, 38).

186. Kondepudi, D. & Prigogine, I. *Modern Thermodynamics: From Heat Engines to Dissipative Structures* (Wiley, 2014) (cited on page 25).

187. Belinfante, F. J. On the current and the density of the electric charge, the energy, the linear momentum and the angular momentum of arbitrary fields. *Physica* **7,** 449–474 (1940) (cited on page 31).

188. Chester, G. V. & Thellung, A. The Law of Wiedemann and Franz. *Proceedings of the Physical Society* (1961) (cited on page 38).

189. Jonson, M. & Mahan, G. D. Mott's formula for the thermopower and the Wiedemann-Franz law. *Phys. Rev. B* **21,** 4223–4229 (10 1980) (cited on page 38).

190. Jonson, M. & Girvin, S. M. Thermoelectric effect in a weakly disordered inversion layer subject to a quantizing magnetic field. *Phys. Rev. B* **29,** 1939–1946 (4 1984) (cited on page 38).

191. Oji, H. & Streda, P. Theory of electronic thermal transport: Magnetoquantum corrections to the thermal transport coefficients. *Phys. Rev. B* **31,** 7291–7295 (11 1985) (cited on page 38).

192. Smrcka, L. & Středa, P. Transport coefficients in strong magnetic fields. *Journal of Physics C: Solid State Physics* **10,** 2153–2161 (1977) (cited on page 38).

193. Abrikosov, A., Gorkov, L., Dzyaloshinski, I. & Silverman, R. *Methods of Quantum Field Theory in Statistical Physics* (Dover Publications, 2012) (cited on page 38).

194. Kadanoff, L. P. & Martin, P. C. Hydrodynamic equations and correlation functions. *Annals of Physics* **24,** 419–469 (1963) (cited on page 38).

195. Andreev, A. V., Kivelson, S. A. & Spivak, B. Hydrodynamic Description of Transport in Strongly Correlated Electron Systems. *Phys. Rev. Lett.* **106,** 256804 (25 2011) (cited on pages 38, 42).

196. Moll, P. J. W., Kushwaha, P., Nandi, N., Schmidt, B. & Mackenzie, A. P. Evidence for hydrodynamic electron flow in PdCoO2. *Science* **351,** 1061–1064 (2016) (cited on page 38).

197. Crossno, J. *et al.* Observation of the Dirac fluid and the breakdown of the Wiedemann-Franz law in graphene. *Science* **351,** 1058–1061 (2016) (cited on pages 38, 42, 50).

198. Jaoui, A. *et al.* Departure from the Wiedemann–Franz law in WP2 driven by mismatch in T-square resistivity prefactors. *npj Quantum Materials* (2018) (cited on page 38).

199. Luttinger, J. M. Theory of the Hall Effect in Ferromagnetic Substances. *Phys. Rev.* **112,** 739–751 (3 1958) (cited on page 38).

200. Crépieux, A. & Bruno, P. Theory of the anomalous Hall effect from the Kubo formula and the Dirac equation. *Phys. Rev. B* **64,** 014416 (1 2001) (cited on page 38).

201. Jungwirth, T., Niu, Q. & MacDonald, A. H. Anomalous Hall Effect in Ferromagnetic Semiconductors. *Phys. Rev. Lett.* **88,** 207208 (20 2002) (cited on page 38).

202. Nagaosa, N. Anomalous Hall Effect –A New Perspective–. *Journal of the Physical Society of Japan* **75,** 042001 (2006) (cited on page 38).

203. Xiao, D., Yao, Y., Fang, Z. & Niu, Q. Berry-Phase Effect in Anomalous Thermoelectric Transport. *Phys. Rev. Lett.* **97,** 026603 (2 2006) (cited on page 39).

204. Lee, W.-L., Watauchi, S., Miller, V. L., Cava, R. J. & Ong, N. P. Anomalous Hall Heat Current and Nernst Effect in the $CuCr_2Se_{4-x}Br_x$ Ferromagnet. *Phys. Rev. Lett.* **93,** 226601 (22 2004) (cited on page 39).

205. Onose, Y., Shiomi, Y. & Tokura, Y. Lorenz Number Determination of the Dissipationless Nature of the Anomalous Hall Effect in Itinerant Ferromagnets. *Phys. Rev. Lett.* **100,** 016601 (1 2008) (cited on page 39).

206. Kim, K.-S. Role of axion electrodynamics in a Weyl metal: Violation of Wiedemann-Franz law. *Phys. Rev. B* **90,** 121108 (12 2014) (cited on pages 39, 42, 50).

207. Gooth, J. *et al.* Thermal and electrical signatures of a hydrodynamic electron fluid in tungsten diphosphide. *Nature Communications* **9,** 4093 (2018) (cited on pages 39, 42, 43, 50).

208. Liang, T. *et al.* Ultrahigh mobility and giant magnetoresistance in the Dirac semimetal Cd3As2. *Nature Materials* **14,** 280 (2014) (cited on page 39).

209. Xu, L. *et al.* Finite-temperature violation of the anomalous transverse Wiedemann-Franz law in absence of inelastic scattering. *arXiv preprint arXiv:1812.04339* (2018) (cited on pages 39, 42, 50).

210. Lewis, H. W. Wave Packets and Transport of Electrons in Metals. *Solid State Physics - Advances in Research and Applications* (1958) (cited on page 39).

211. Behnia, K. The Nernst effect and the boundaries of the Fermi liquid picture. *Journal of Physics Condensed Matter* (2009) (cited on page 42).

212. Das, K. & Agarwal, A. Berry curvature induced thermopower in type-I and type-II Weyl Semimetals. *arXiv preprint arXiv:1903.01205* (2019) (cited on pages 42, 43).

213. Scaffidi, T., Nandi, N., Schmidt, B., Mackenzie, A. P. & Moore, J. E. Hydrodynamic Electron Flow and Hall Viscosity. *Phys. Rev. Lett.* **118,** 226601 (22 2017) (cited on page 42).

214. Alekseev, P. S. Negative Magnetoresistance in Viscous Flow of Two-Dimensional Electrons. *Phys. Rev. Lett.* **117,** 166601 (16 2016) (cited on page 42).

215. De Jong, M. J. M. & Molenkamp, L. W. Hydrodynamic electron flow in high-mobility wires. *Phys. Rev. B* **51,** 13389–13402 (19 1995) (cited on page 42).

216. Cao, C. *et al.* Universal Quantum Viscosity in a Unitary Fermi Gas. *Science* **331,** 58–61 (2011) (cited on page 42).

217. Hartnoll, S. A. Theory of universal incoherent metallic transport. *Nature Physics* **11,** 54 (2014) (cited on page 42).

218. Levitov, L. & Falkovich, G. Electron viscosity, current vortices and negative nonlocal resistance in graphene. *Nature Physics* **12,** 672 (2016) (cited on page 42).

219. Mahajan, R., Barkeshli, M. & Hartnoll, S. A. Non-Fermi liquids and the Wiedemann-Franz law. *Phys. Rev. B* **88,** 125107 (12 2013) (cited on page 42).

220. Principi, A. & Vignale, G. Violation of the Wiedemann-Franz Law in Hydrodynamic Electron Liquids. *Phys. Rev. Lett.* **115,** 056603 (5 2015) (cited on page 42).

221. Hill, R. W., Proust, C., Taillefer, L., Fournier, P. & Greene, R. L. Breakdown of Fermi-liquid theory in a copper-oxide superconductor. *Nature* **414,** 711–715 (2001) (cited on page 42).

222. Tanatar, M. A., Paglione, J., Petrovic, C. & Taillefer, L. Anisotropic Violation of the Wiedemann-Franz Law at a Quantum Critical Point. *Science* **316,** 1320–1322 (2007) (cited on page 42).

223. Wakeham, N. *et al.* Gross violation of the Wiedemann–Franz law in a quasi-one-dimensional conductor. *Nature Communications* **2,** 396 (2011) (cited on page 42).

224. Siegel, D. A., Regan, W., Fedorov, A. V., Zettl, A. & Lanzara, A. Charge-Carrier Screening in Single-Layer Graphene. *Phys. Rev. Lett.* **110,** 146802 (14 2013) (cited on page 42).

225. Principi, A. & Vignale, G. Intrinsic charge and spin conductivities of doped graphene in the Fermi-liquid regime. *Phys. Rev. B* **91,** 205423 (20 2015) (cited on page 42).

226. Bandurin, D. A. *et al.* Negative local resistance caused by viscous electron backflow in graphene. *Science* **351,** 1055–1058 (2016) (cited on page 42).

227. Krishna Kumar, R. *et al.* Superballistic flow of viscous electron fluid through graphene constrictions. *Nature Physics* **13,** 1182 (2017) (cited on page 42).

228. Berdyugin, A. I. *et al.* Measuring Hall viscosity of graphene's electron fluid. *Science* **364,** 162–165 (2019) (cited on page 42).

229. Lucas, A., Davison, R. A. & Sachdev, S. Hydrodynamic theory of thermoelectric transport and negative magnetoresistance in Weyl semimetals. *Proceedings of the National Academy of Sciences* **113,** 9463–9468 (2016) (cited on page 43).

230. Gorbar, E. V., Miransky, V. A., Shovkovy, I. A. & Sukhachov, P. O. Consistent hydrodynamic theory of chiral electrons in Weyl semimetals. *Phys. Rev. B* **97,** 121105 (12 2018) (cited on page 43).

231. Gorbar, E. V., Miransky, V. A., Shovkovy, I. A. & Sukhachov, P. O. Nonlocal transport in Weyl semimetals in the hydrodynamic regime. *Phys. Rev. B* **98,** 035121 (3 2018) (cited on page 43).

232. Noky, J., Gooth, J., Felser, C. & Sun, Y. Characterization of topological band structures away from the Fermi level by the anomalous Nernst effect. *Phys. Rev. B* **98,** 241106 (24 2018) (cited on page 43).

233. Altland, A., Altland, P. & Simons, B. *Condensed Matter Field Theory* (Cambridge University Press, 2006) (cited on page 44).

234. Miransky, V. A. & Shovkovy, I. A. Quantum field theory in a magnetic field: From quantum chromodynamics to graphene and Dirac semimetals. *Physics*

Reports **576.** Quantum field theory in a magnetic field: From quantum chromodynamics to graphene and Dirac semimetals, 1–209 (2015) (cited on pages 45, 46, 50).

235. Nguyen, D. X. & Gromov, A. Exact electromagnetic response of Landau level electrons. *Phys. Rev. B* **95,** 085151 (8 2017) (cited on page 46).

236. Wei, P., Bao, W., Pu, Y., Lau, C. N. & Shi, J. Anomalous Thermoelectric Transport of Dirac Particles in Graphene. *Phys. Rev. Lett.* **102,** 166808 (16 2009) (cited on page 50).

237. Tabert, C. J., Carbotte, J. P. & Nicol, E. J. Optical and transport properties in three-dimensional Dirac and Weyl semimetals. *Phys. Rev. B* **93,** 085426 (8 2016) (cited on page 50).

238. Castellanos-Gomez, A. *et al.* Local Strain Engineering in Atomically Thin MoS2. *Nano Letters* **13,** 5361–5366 (2013) (cited on page 52).

239. Kamboj, S. *et al.* Generation of strain-induced pseudo-magnetic field in a doped type-II Weyl semimetal. *Phys. Rev. B* **100,** 115105 (11 2019) (cited on pages 52, 54, 67, 68, 79, 81).

240. Sasaki, K.-i., Kawazoe, Y. & Saito, R. Local Energy Gap in Deformed Carbon Nanotubes. *Progress of Theoretical Physics* (2005) (cited on pages 51, 54).

241. Guinea, F., Horovitz, B. & Le Doussal, P. Gauge field induced by ripples in graphene. *Phys. Rev. B* **77,** 205421 (20 2008) (cited on pages 51, 54).

242. Mañes, J. L., de Juan, F., Sturla, M. & Vozmediano, M. A. H. Generalized effective Hamiltonian for graphene under nonuniform strain. *Phys. Rev. B* **88,** 155405 (15 2013) (cited on pages 52, 56, 61, 66, 101, 102).

243. Landau, L. *et al. Theory of Elasticity* (Elsevier Science, 1986) (cited on pages 53, 77).

244. Kleinert, H. *Gauge Fields in Condensed Matter* (Worls Scientific, Singapore, 1989) (cited on page 53).

245. Landau, L. & Lifshitz, E. *Fluid Mechanics* **v. 6** (Elsevier Science, 2013) (cited on page 54).

246. Guinea, F. Strain engineering in graphene. *Solid State Communications* **152.** Exploring Graphene, Recent Research Advances, 1437–1441 (2012) (cited on page 54).

247. Amorim, B. *et al. Novel effects of strains in graphene and other two dimensional materials* Novel effects of strains in graphene and other two dimensional materials. 2016 (cited on pages 54, 55).

248. Morpurgo, A. F. & Guinea, F. Intervalley Scattering, Long-Range Disorder, and Effective Time-Reversal Symmetry Breaking in Graphene. *Phys. Rev. Lett.* **97,** 196804 (19 2006) (cited on page 54).

249. Morozov, S. V. *et al.* Strong Suppression of Weak Localization in Graphene. *Phys. Rev. Lett.* **97,** 016801 (1 2006) (cited on page 54).

250. Katsnelson, M. I. & Novoselov, K. S. Graphene: New bridge between condensed matter physics and quantum electrodynamics. *Solid State Communications* (2007) (cited on page 54).

251. Pereira, V. M. & Castro Neto, A. H. Strain Engineering of Graphene's Electronic Structure. *Phys. Rev. Lett.* **103,** 046801 (4 2009) (cited on pages 54, 67).

252. Guinea, F., Geim, A. K., Katsnelson, M. I. & Novoselov, K. S. Generating quantizing pseudomagnetic fields by bending graphene ribbons. *Phys. Rev. B* **81,** 035408 (3 2010) (cited on pages 54, 79, 81).

253. Gorbar, E. V., Miransky, V. A., Shovkovy, I. A. & Sukhachov, P. O. Consistent Chiral Kinetic Theory in Weyl Materials: Chiral Magnetic Plasmons. *Phys. Rev. Lett.* **118,** 127601 (12 2017) (cited on page 57).

254. Goerbig, M. O., Fuchs, J.-N., Montambaux, G. & Piéchon, F. Tilted anisotropic Dirac cones in quinoid-type graphene and α – $(BEDT\ TTF)_2I_3$. *Phys. Rev. B* **78,** 045415 (4 2008) (cited on pages 58, 68).

255. Goerbig, M. O., Fuchs, J.-N., Montambaux, G. & Piéchon, F. Electric-field–induced lifting of the valley degeneracy in α – $(BEDT\ TTF)_2I_3$ Dirac-like Landau levels. *EPL (Europhysics Letters)* **85,** 57005 (2009) (cited on pages 58, 68).

256. Jafari, S. A. Electric field assisted amplification of magnetic fields in tilted Dirac cone systems. *Phys. Rev. B* **100,** 045144 (4 2019) (cited on page 58).

257. Sári, J., Goerbig, M. O. & Tőke, C. Magneto-optics of quasirelativistic electrons in graphene with an inplane electric field and in tilted Dirac cones in α – $(BEDT\ TTF)_2I_3$. *Phys. Rev. B* **92,** 035306 (3 2015) (cited on pages 58, 68).

258. Tchoumakov, S., Civelli, M. & Goerbig, M. O. Magnetic-Field-Induced Relativistic Properties in Type-I and Type-II Weyl Semimetals. *Phys. Rev. Lett.* **117,** 086402 (8 2016) (cited on pages 58, 68, 72, 83).

259. Yu, Z.-M., Yao, Y. & Yang, S. A. Predicted Unusual Magnetoresponse in Type-II Weyl Semimetals. *Phys. Rev. Lett.* **117,** 077202 (7 2016) (cited on pages 58, 68, 72, 83).

260. Volovik, G. E. Black hole and hawking radiation by type-II Weyl fermions. *JETP Letters* **104,** 645–648 (2016) (cited on page 58).

261. Zhang, K. & Volovik, G. E. Lifshitz transitions via the type-II dirac and type-II Weyl points. *JETP Letters* **105,** 519–525 (2017) (cited on page 58).

262. Chang, G. *et al.* A strongly robust type II Weyl fermion semimetal state in Ta3S2. *Science Advances* **2** (2016) (cited on pages 58, 61).

263. Kim, S. J., Nanjundaswamy, K. S. & Hughbanks, T. Single-crystal structure of tantalum sulfide (Ta3S2). Structure and bonding in the Ta6Sn (n = 1,3,4,5?) pentagonal-antiprismatic chain compounds. *Inorganic Chemistry* **30,** 159–164 (1991) (cited on page 58).

264. Nozaki, H., Wada, H. & Takekawa, S. Galvanomagnetic Properties of Ta3S2, Ta2S and Ta6S. *Journal of the Physical Society of Japan* **60,** 3510–3515 (1991) (cited on page 58).

265. Chernodub, M. N., Cortijo, A., Grushin, A. G., Landsteiner, K. & Vozmediano, M. A. H. Condensed matter realization of the axial magnetic effect. *Phys. Rev. B* **89,** 081407 (8 2014) (cited on pages 58, 64).

266. Slater, J. C. & Koster, G. F. Simplified LCAO Method for the Periodic Potential Problem. *Phys. Rev.* **94,** 1498–1524 (6 1954) (cited on page 59).

267. Gorbar, E. V., Miransky, V. A. & Shovkovy, I. A. Engineering Weyl nodes in Dirac semimetals by a magnetic field. *Phys. Rev. B* **88,** 165105 (16 2013) (cited on page 60).

268. Vaezi, A., Abedpour, N., Asgari, R., Cortijo, A. & Vozmediano, M. A. H. Topological electric current from time-dependent elastic deformations in graphene. *Phys. Rev. B* **88,** 125406 (12 2013) (cited on page 66).

269. Muñoz, E. & Soto-Garrido, R. Thermoelectric transport in torsional strained Weyl semimetals. *Journal of Applied Physics* (2019) (cited on page 66).

270. Nielsen, H. B. & Ninomiya, M. The Adler-Bell-Jackiw anomaly and Weyl fermions in a crystal. *Physics Letters B* (1983) (cited on page 68).

271. Burkov, A. A. Chiral anomaly and transport in Weyl metals. *Journal of Physics Condensed Matter* (2015) (cited on page 68).

272. Jia, S., Xu, S.-Y. & Hasan, M. Z. Weyl semimetals, Fermi arcs and chiral anomalies. *Nature Materials* **15,** 1140 (2016) (cited on page 68).

273. MacDonald, A. H. Quantized Hall conductance in a relativistic two-dimensional electron gas. *Phys. Rev. B* **28,** 2235–2236 (4 1983) (cited on page 68).

274. Lukose, V., Shankar, R. & Baskaran, G. Novel Electric Field Effects on Landau Levels in Graphene. *Phys. Rev. Lett.* **98,** 116802 (11 2007) (cited on pages 68, 75).

275. Peres, N. M. & Castro, E. V. Algebraic solution of a graphene layer in transverse electric and perpendicular magnetic fields. *Journal of Physics Condensed Matter* (2007) (cited on pages 68, 75).

276. Castro, E. V., Cazalilla, M. A. & Vozmediano, M. A. H. Raise and collapse of pseudo Landau levels in graphene. *Phys. Rev. B* **96,** 241405 (24 2017) (cited on pages 69, 83).

277. Lorentz, H., Einstein, A., Minkowski, H., Weyl, H. & Sommerfeld, A. *The Principle of Relativity: A Collection of Original Memoirs on the Special and General Theory of Relativity* (Dover, 1952) (cited on page 69).

278. Landau, L., Lifshitz, E. & Hamermesh, M. *The Classical Theory of Fields* (Elsevier Science, 1975) (cited on pages 69, 77).

279. Einstein, A., Beck, A. & Havas, P. *The Collected Papers of Albert Einstein, Volume 2: The Swiss Years* (Princeton University Press, 1989) (cited on page 69).

280. Møller, C. *The theory of relativity* (Clarendon Press, 1972) (cited on page 69).

281. Lorentz, H. A. Simplified theory of electrical and optical phenomena in moving systems. *Koninklijke Nederlandse Akademie van Wetenschappen Proceedings Series B Physical Sciences* **1,** 427–442 (1898) (cited on page 69).

282. Kramer, T., Bracher, C. & Kleber, M. Electron propagation in crossed magnetic and electric fields. *Journal of Optics B: Quantum and Semiclassical Optics* (2004) (cited on page 76).

283. Singh, V. & Deshmukh, M. M. Nonequilibrium breakdown of quantum Hall state in graphene. *Phys. Rev. B* **80,** 081404 (8 2009) (cited on page 76).

284. Gu, N., Rudner, M., Young, A., Kim, P. & Levitov, L. Collapse of Landau Levels in Gated Graphene Structures. *Phys. Rev. Lett.* **106,** 066601 (6 2011) (cited on page 76).

285. Hofmeister, A. M. & Mao, H.-k. Redefinition of the mode Gruneisen parameter for polyatomic substances and thermodynamic implications. *Proceedings of the National Academy of Sciences* (2002) (cited on page 77).

286. Ibach, H. & Lüth, H. *Solid-State Physics: An Introduction to Principles of Materials Science* (Springer Berlin Heidelberg, 2009) (cited on page 77).

287. Hasan, M. Z., Xu, S.-Y., Belopolski, I. & Huang, S.-M. Discovery of Weyl Fermion Semimetals and Topological Fermi Arc States. *Annual Review of Condensed Matter Physics* **8,** 289–309 (2017) (cited on page 78).

288. Chang, G. *et al.* Unconventional Chiral Fermions and Large Topological Fermi Arcs in RhSi. *Phys. Rev. Lett.* **119,** 206401 (20 2017) (cited on page 78).

289. Rachel, S., Göthel, I., Arovas, D. P. & Vojta, M. Strain-Induced Landau Levels in Arbitrary Dimensions with an Exact Spectrum. *Phys. Rev. Lett.* **117,** 266801 (26 2016) (cited on pages 80, 81).

290. Storz, O. *et al.* Mapping the effect of defect-induced strain disorder on the Dirac states of topological insulators. *Phys. Rev. B* **94,** 121301 (12 2016) (cited on page 83).

291. Simon, B. Holonomy, the Quantum Adiabatic Theorem, and Berry's Phase. *Phys. Rev. Lett.* **51,** 2167–2170 (24 1983) (cited on page 90).

292. Aharonov, Y. & Bohm, D. Significance of Electromagnetic Potentials in the Quantum Theory. *Phys. Rev.* **115,** 485–491 (3 1959) (cited on page 91).

293. Gradshteyn, I. S. & Ryzhik, I. M. *Table of Integrals, Series, and Products, 7th Edition* (Elsevier Academic Press, 2007) (cited on page 97).

294. De Juan, F., Mañes, J. L. & Vozmediano, M. A. H. Gauge fields from strain in graphene. *Phys. Rev. B* **87,** 165131 (16 2013) (cited on pages 101, 102).